Check for updates

Received: 18 October 2021 | Revised: 7 February 2022 | Accepted: 10 March 2022

DOI: 10.1002/fld.5085

RESEARCH ARTICLE

WILEY

Periodic hill flow simulations with a parameterized cumulant lattice Boltzmann method

Martin Gehrke | **Thomas Rung**

Hamburg University of Technology, TUHH, Institute for Fluid Dynamics and Ship Theory, Hamburg, Germany

Correspondence
Martin Gehrke, Hamburg University of Technology, TUHH, Institute for Fluid Dynamics and Ship Theory, Am Schwarzenberg-Campus 4, 21073 Hamburg, Germany.
Email: martin.gehrke@tuhh.de

Funding information
TUHH

Abstract

The article is concerned with the assessment of a cumulant lattice Boltzmann method in wall-bounded, separated turbulent shear flows. The approach is of interest for its resolution-spanning success in turbulent channel flows without using a specific turbulence treatment. The assessment focuses upon the flow over a periodic hill, which offers a rich basis of numerical and experimental data, for Reynolds numbers within $700 \leq \mathrm{Re} \leq 37{,}000$. The analysis involves the mean flow field, second moments and their invariants, as well as spectral data obtained for a wide range of resolutions with $2 \lesssim \Delta x_i^+ \lesssim 100$. With the emphasis on a recently published parameterized cumulant collision operator, the universality of the value assigned to a stability preserving regularization parameter is assessed. Reported results guide resolution-dependent optimized values and indicate a required minimum resolution of $\Delta x_i^+ \approx 30$. Analog to the findings for attached turbulent shear flows, the approach appears to adequately resolve complex turbulent flows without the need for ad hoc modeling for a range of scale resolving resolutions.

KEYWORDS

cumulant lattice Boltzmann method, GPU computing, lattice Boltzmann, separated shear flows, turbulent boundary layer, turbulent flow

1 | INTRODUCTION

Many recent fluid engineering applications are concerned with inherently unsteady problems where turbulent and transient motion are hardly separable, and turbulence modeling becomes difficult. On the contrary, comprehensive time-dependent studies or efforts to resolve turbulent scales often remain challenging if not unfeasible for industrial computational fluid dynamics (CFD), particularly for large Reynolds number applications. An example refers to flow control efforts increasingly introduced to the fluid dynamic design of cars, aircraft, or ships. The lattice Boltzmann method (LBM) has recently gained enhanced attention for transient simulations of scale resolving industrial flows.[1-3] The method offers favorable efficiency features also adopted by a few other recent CFD strategies, that is, weak compressibility, explicit advancing in time, and a structured grid discretization. A crucial algorithmic benefit of LBM is the strict locality of nonlinear expressions. However, the turbulence simulation capabilities remain uncertain, limiting its use in practical applications.

This is an open access article under the terms of the Creative Commons Attribution License, which permits use, distribution and reproduction in any medium, provided the original work is properly cited.
© 2022 The Authors. *International Journal for Numerical Methods in Fluids* published by John Wiley & Sons, Ltd.

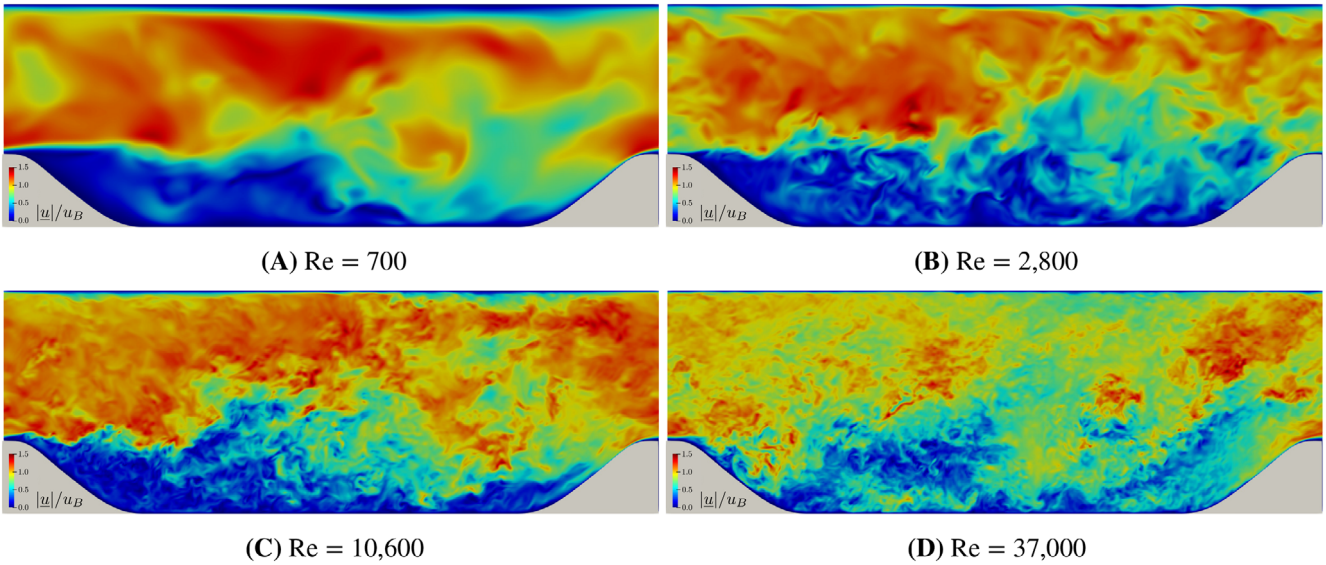

FIGURE 1 Instantaneous normalized velocity magnitude in the *x*-*y* center plane for the four investigated Reynolds numbers [Colour figure can be viewed at wileyonlinelibrary.com]

The performance of LBM in turbulent flows is notably intertwined with the employed collision operator. Therefore, the formulation of adequate collision models is a focal area of LBM research. Various improvements of the initial single-time BGK[4] collision operator were suggested to increase the stability and accuracy in high Reynolds number (turbulent) flows. A detailed review of collision operators and their rationale is beyond the scope of this article, and we refer, for instance, to a recent comprehensive paper of Coreixas et al.[5] Published suggestions for improved collision operators adopt two and more relaxation times, for example, TRT[6,7] and MRT[8,9] approaches, introduce an improved Galilean invariance of the collision operator as suggested by the cascaded approach,[10] promote stability in addition to accuracy enhancements by a regularization[11] as well as by a local adaptation of relaxation times using discrete entropy minimizing methods,[12-14] or relax the distribution functions in cumulant space.[15,16] The latter is the focal point of our effort.

As regards scale-resolving simulations of turbulent engineering shear flows, the predictive accuracy of different LBM concepts has been investigated in, for example, Pasquali,[17] Gehrke et al.,[18,19] Nathen et al.,[20] and Geier et al.[21] to assess the influence of the collision operator and the employed LBM discretization strategy. Still, virtually all these studies focus on the predictive performance in fairly generic flows, for example, a turbulence-driven decay of large vortices in a periodic box, the so-called Taylor–Green vortex (TGV) test case, or a wall-bounded unidirectional mean shear in a plane channel flow. On the contrary, few systematic efforts into separated engineering shear flows were published. The present article aims to assess the performance of a more recent well-conditioned parameterized (WP) cumulant collision operator[16] in a particular separated shear flow that has previously been examined in greater detail. To this end, the flow over a periodic hill arrangement that is, mounted to the bottom wall of a straight channel[22] is computed. Figure 1 outlines snapshots of the instantaneous velocity magnitude for different Reynolds numbers in a centered *x*-*y*-plane of the numerical domain, which is perpendicular to the homogeneous direction of the geometry. As indicated by the figure, an increase in the Reynolds number is associated with a decrease in flow structure sizes and a more intensified turbulent motion. Due to the simple setup of the geometry and the boundary conditions, the test case refers to a frequently computed benchmark studied to assess the turbulence modeling capabilities of various CFD approaches.

The present study utilizes results obtained from a 27-point three-dimensional spatial LBM discretization (*D*3*Q*27) on isotropic homogeneous Cartesian grids to analyze the predictive capabilities of the WP cumulant LBM for the periodic hill test case. The WP cumulant operator was chosen because it offers improved stability properties controlled by a single user-defined parameter. Attention is restricted to four different Reynolds numbers, Re = {700; 2800; 10,600; 37,000}, where results are compared with solutions of Navier–Stokes-based direct (DNS) and large eddy (LES) simulations for all investigated Reynolds numbers as well as experimental data for Re = {10,600; 37,000}. The utilized D3Q27 discretization supports Galilean invariance and offers benefits when pronounced nonlinearities occur. For this reason, we exclude related stencil influences from the present study and refer to previously reported investigations of the cumulant LBM.[19,23] All simulations were subject to the waiver of a turbulence closure or wall function, which is a crucial aspect of the study,

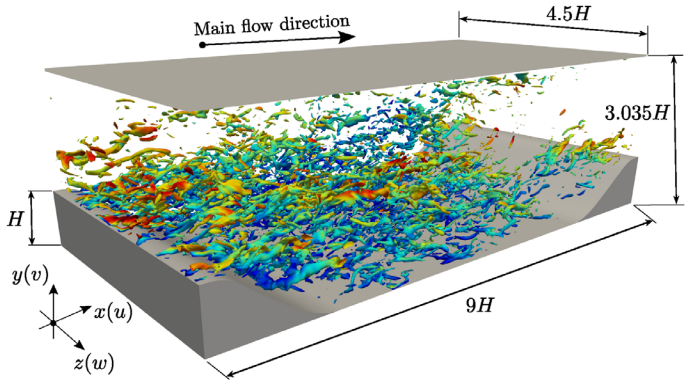

FIGURE 2 Illustration of the physical domain supplemented by isosurfaces of the longitudinal vorticity component $\omega_x = \partial u_z/\partial y - \partial u_y/\partial z$ (20% of the maximum value) colored by the velocity magnitude [Colour figure can be viewed at wileyonlinelibrary.com]

and different spatial and temporal resolutions were assessed. Emphasis is given to the influence of the value assigned to the stability-enhancing regularization parameter and its relation to the required resolution. The discussion involves mean flow data as well as Reynolds stresses and is supplemented by one-dimensional power spectra obtained from locally recorded time series of the velocity vector. Results of the present study reveal an interplay between the value assigned to the regularization parameter and the (near-wall) resolution of the grid.

The remainder of the article is structured as follows. The subsequent parts of the introduction outline the test case details and briefly describe the status of cumulant LBM applied to turbulent flows. Section 2 provides details of the numerical method and Section 3 is concerned with case specific computational aspects. Section 4 is devoted to the comprehensive presentation of results. Final conclusions are drawn in Section 5. A description of the geometry and the explicit implementation of the cumulant collision operator are given in the Appendix.

1.1 | Periodic hill test case description

The periodic hill test case (PHTC) was initially the subject of experimental investigations for a periodic arrangement of analytically described hills in a straight channel, compare Figure 2. The geometry is homogeneous in the lateral (z) direction, and the flow is deemed periodic in the longitudinal (x) and lateral direction. The case features separation from a curved surface and accelerated and decelerated mean shear. Due to the more complex physics, the test case represents a natural candidate to scrutinize simulation capabilities subsequent to assessing simple flows, for example, unidirectional channel flows.[19] The PHTC is part of prominent benchmark databases, for example, ERCOFTAC,[24] featuring reference data from various simulations[25,26] and experiments.[27]

To reduce the influence of lateral walls and improve the periodicity in the lateral direction, the initial geometry,[28] firstly numerically analyzed by Bonnin et al.,[29] was revised by Mellen et al.[22] The revised setup also served as a basis for extensive experimental studies, for example, Rapp et al.[27,30] In comparison to the initial geometry, the revised geometry increases the ratio of the horizontal to vertical dimension L_x/L_y to π, which avoids a longitudinal correlation.[31] Experimental data for the revised geometry were reported for four Reynolds numbers, $\mathrm{Re} = \{5600; 10,600; 19,000; 37,000\}$ by Rapp et al.[27] and two further Reynolds numbers, $\mathrm{Re} = \{8000; 33,000\}$ by Kähler et al.,[32] whereas numerical studies[31,33-38] refer to an wider range of Reynolds numbers between $\mathrm{Re} = 10^2$ and $\mathrm{Re} = 10^5$ forlaminar as well as highly turbulent conditions. Similar to the majority of investigations, the present study employs the revised geometry in a domain that spans $L_x \times L_y \times L_z = 9H \times 3.035H \times 4.5H$. Here H refers to the height of the hill, L_x denotes the horizontal distance between the hill crests, and L_y denotes the maximum vertical distance between the plane bottom wall and the straight top wall, compare Figure 2. Numerical simulations are performed with periodic boundary conditions along the longitudinal (x) and lateral (z) end planes. The definition of the Reynolds number employs H and the bulk velocity u_B at the entrance plane ($x = 0$), which is spatially averaged in lateral (z) and vertical (y) direction,

$$\mathrm{Re} = \frac{u_B\, H}{\nu} \qquad \text{with} \quad u_B = \frac{1}{2.035H \cdot L_z} \int_{L_z} \int_{H}^{3.035H} u\,(x = 0, y, z)\, \mathrm{d}y\, \mathrm{d}z. \tag{1}$$

1.2 | Development of cumulant collision operators

The use of cumulants in conjunction with LBM simulations was initially suggested by Seeger et al.[39] in the year 2000 and has received increased attention following the publication of Geier et al.[15] in 2015. While the initial publication[39] refers to the equations of motion in cumulant space, the subsequent studies[15,16] restrict the use of cumulants to the collision step for a D3Q27 discretization. The suggested collision operator[15] employs ten different relaxation rates ω_i ($i \in [1, \dots, 10]$) to relax the cumulants toward their specific equilibria. Generally, the choice of the relaxation rates strongly influences the stability and the predictive accuracy of the LBM and therefore motivates research into collision operators.

Only a single relaxation rate (ω_1) is usually linked to a physically observable quantity and is defined from the shear viscosity of the underlying fluid. The remaining nine relaxation rates are user-specified and bounded to $\omega_i \in [0, 2]$ and often assigned to unity, $\omega_2 = \omega_3 = \cdots = \omega_{10} = 1$, which refers to the *all one* (AO) approach. The AO approach greatly supports the method's stability due to neglecting the nonequilibrium parts of the third to sixth-order cumulants in the collision step, whereby the concerning postcollision states are set to zero. The AO cumulant approach was tested for a few benchmark cases,[15,40] among them Taylor–Green vortex for moderate Reynolds numbers and the flow around a sphere for Reynolds numbers in the range of $\mathcal{O}(10^2)$ to $\mathcal{O}(10^5)$. Asmuth et al.[41] have successfully applied the AO approach to study more complex wind turbine flows at higher Reynolds numbers $\mathrm{Re} \approx \mathcal{O}(10^7)$ on relatively coarse grids. A first modification of the cumulant collision operator was suggested by Geier et al.,[15] see Appendix J therein. The modification aims at a reduction of round-off errors due to a particular calculation sequence when reconstructing the flow field from the particle distribution functions of the lattice Boltzmann equation and is labeled *well-conditioned* (W) cumulant.

Turbulence model-free applications of the W and AO cumulant models were assessed in greater detail for lower Reynolds number turbulent flows, for example, transitional ZPG flat plate,[42] Taylor–Green vortex, and channel flows.[18,19] Increasing the Reynolds number, the viscosity-related relaxation rate approaches $\omega_1 \to 2$, whereby the nonequilibrium parts of the second-order cumulant expressions are almost fully conserved during the collision step, whereby instabilities could emerge. These hamper the robustness of the approach and trigger further modifications. A derivative of the well-conditioned (W) cumulant was suggested and applied by Geier et al.,[16,43] labeled the *well-conditioned parameterized* (WP) cumulant. The WP approach includes stability enhancing regularization, which also helps to improve the accuracy. It combines the well-conditioned approach with a parameterization of three relaxation rates ($\omega_3, \omega_4, \omega_5$) and two parameters ($A, B$) as a function of the shear and the bulk viscosity, and thereby ω_1 and ω_2, compare Section 2.2. The parameterization involves a single unified regularization parameter λ to limit the third-order nonequilibrium contributions during the collision. In general, numerical damping is introduced through the regularization parameter. A default value is assigned to $\lambda_{\mathrm{def}} = 10^{-2}$, and smaller values around $\lambda \leq 10^{-6}$ restore unit relaxation rates ($\to$ AO) by disabling the parameterization. The regularization interacts with the turbulence treatment by suppressing the small-scale motion of the upper-frequency end, compare Section 4, also observed by Asmuth et al.[44] for wind turbine simulations. The latter study compares results of an LES-WP ($\lambda = 10^{-6}$) that incorporates an algebraic subgrid-scale (SGS) closure model, with results obtained by increasing the regularization parameter from the default value to $\lambda = 10^{-1}$ and $\lambda = 10^{0}$ without the use of an SGS turbulence model. The study indicates significant flow changes in the turbulent wake downstream of the wind turbine, whereby results obtained from $\lambda = 10^{-2}$ to some extent resembled SGS results, but no detailed grid influences were assessed. Moreover, Pasquali[17] also vaguely researched the influence of increased or specifically tuned λ values for turbulent channel flow simulations at $\mathrm{Re}_\tau = \{950; 2000; 16,000\}$.

2 | NUMERICAL METHOD

This section briefly introduces the underlying LBM, the utilized specific collision operator, and its relaxation rates and summarizes the details of the applied solid wall boundary condition.

2.1 | Lattice Boltzmann procedure

The current study is based on a GPU-based (graphics processing unit) lattice Boltzmann implementation[45] for the simulation of incompressible fluid flow.[46,47] The Boltzmann equation governs the particle distribution functions $f(\boldsymbol{x}, t, \boldsymbol{\xi})$ and reads

$$\frac{\partial f(\boldsymbol{x},t,\boldsymbol{\xi})}{\partial t}+\boldsymbol{\xi}\cdot\frac{\partial f(\boldsymbol{x},t,\boldsymbol{\xi})}{\partial \boldsymbol{x}}+F\,\frac{\partial f(\boldsymbol{x},t,\boldsymbol{\xi})}{\partial \boldsymbol{\xi}}=\Omega. \tag{2}$$

The particle distribution function (PDF) describes the probability of encountering a particle located at position $\boldsymbol{x}$ with the velocity $\boldsymbol{\xi}$ at the time t. While the left-hand side of the Boltzmann equation (2) is of advection type, the right-hand side contains the so-called collision operator Ω, which covers the interaction of particles. The third term of the left-hand side incorporates surface or body forces. For the sake of simplicity, the term is neglected below. The consideration of body forces is outlined in Appendix B.1.

In the framework of a numerical approximation, the Boltzmann equation is solved for a set of discrete particle distribution functions described by a lattice of grid points. The present study employs a regular D3Q27 lattice. Accordingly, a set of 27 discrete velocities $\boldsymbol{e}_{ijk}$ is introduced, oriented in 27 characteristic directions of the underlying grid, compare Figure 3. Deploying these assumptions, Equation (2) transforms into a set of discrete equations

$$\frac{\partial f_{ijk}(\boldsymbol{x},t)}{\partial t}+\boldsymbol{e}_{ijk}\cdot\frac{\partial f_{ijk}(\boldsymbol{x},t)}{\partial \boldsymbol{x}}=\Omega_{ijk}, \tag{3}$$

where $\boldsymbol{e}_{ijk}=c\times(i,j,k)$ refers to a directional speed matrix, with $i,j,k\in(\bar{1},0,1)$ based on the Miller notation ($-1\equiv\bar{1}$, $0\equiv 0$, $1\equiv 1$),

$$\boldsymbol{e}_{ijk}=c\begin{pmatrix}0&1&\bar{1}&0&0&0&0&1&\bar{1}&1&\bar{1}&1&\bar{1}&1&\bar{1}&0&0&0&0&1&1&1&1&\bar{1}&\bar{1}&\bar{1}&\bar{1}\\0&0&0&1&\bar{1}&0&0&1&\bar{1}&\bar{1}&1&0&0&0&0&1&\bar{1}&1&\bar{1}&1&\bar{1}&1&\bar{1}&1&\bar{1}&1&\bar{1}\\0&0&0&0&0&1&\bar{1}&0&0&0&0&1&\bar{1}&\bar{1}&1&1&\bar{1}&\bar{1}&1&1&1&\bar{1}&\bar{1}&1&1&\bar{1}&\bar{1}\end{pmatrix}. \tag{4}$$

The lattice speed is defined as $c=\Delta x/\Delta t$, where Δx represents the regular lattice spacing, and Δt is the time step. Usually, spatial and temporal unit spacings are assumed, that is, $\Delta x=1$ and $\Delta t=1$. Thus c is also assigned to unity implying the particles are restricted to stay or move only to one of their next neighbor nodes within a discrete time step. The numerical solution of the discrete Boltzmann equation (3) is obtained from a finite difference approximation in space and time over a grid cell

$$f_{ijk}(\boldsymbol{x}+\boldsymbol{e}_{ijk}\Delta t,t+\Delta t)=f_{ijk}(\boldsymbol{x},t)+\Delta t\;\Omega_{ijk}. \tag{5}$$

As indicated by the Chapman–Enskog theory,[48] the LBE (5) converges to that of the incompressible Navier–Stokes equation for sufficiently small spatial and temporal step sizes, as well as adequately small Mach (Ma) and Knudsen numbers. The macroscopic flow quantities of pressure and velocity are extracted from the PDF space via

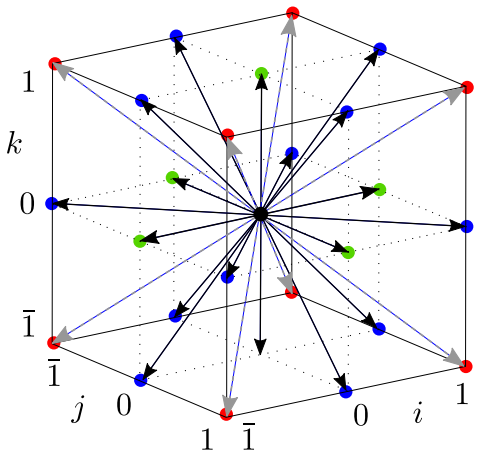

FIGURE 3 D3Q27 lattice model used in the present LBM, where the arrows indicate the 27 possible velocity vectors. The so-called collocation points are marked in color [Colour figure can be viewed at wileyonlinelibrary.com]

$$p = c_s^2\ \rho \sum_{i=\bar{1}}^{1}\sum_{j=\bar{1}}^{1}\sum_{k=\bar{1}}^{1} f_{ijk} \quad \text{and} \quad u_i = (u,v,w)^{\intercal} = \frac{1}{\rho}\sum_{i=\bar{1}}^{1}\sum_{j=\bar{1}}^{1}\sum_{k=\bar{1}}^{1} f_{ijk}\ \boldsymbol{e}_{ijk}, \tag{6}$$

where $c_s = c/\sqrt{3}$ matches the speed of sound in the lattice. The solution procedure is usually divided into two parts involving

$$f^*_{ijk}(\boldsymbol{x},t) = f_{ijk}(\boldsymbol{x},t) + \Omega_{ijk} \qquad \text{the collision step,} \tag{7}$$

$$f_{ijk}(\boldsymbol{x} + \boldsymbol{e}_{ijk}\Delta t, t + \Delta t) = f^*_{ijk}(\boldsymbol{x},t) \qquad \text{and the propagation step.} \tag{8}$$

The first part (7) contains the collision step, where the initial particle distribution function $f_{ijk}(\boldsymbol{x},t)$ deviates from equilibrium state due to the collision of particles. The asterisk notation f^*_{ijk} represents the postcollision particle distribution function. The second part (8) shifts the evolved particle distribution functions to their respective neighboring nodes and is termed the propagation step. The prevalent strict locality of the collision step allows exploiting the advantage of GPUs for high-performance computing.[49]

2.2 | Cumulant collision operator

Previously reported studies[15,16,18,19,41,42,44,50] demonstrated that the cumulant collision operator is suitable for simulating transitional and turbulent flows. To save space, we only provide a brief description of the approach and its implementation, and the reader is referred to the initial work of Geier et al.[15] for a more in-depth explanation of the cumulant LBM. The method involves transforming the PDFs from phase space (ξ,ψ,ζ) to frequency space $(\vec{\Xi}) = (\Xi,\Psi,Z)$ by a two-sided Laplace transform

$$\mathscr{L}\{f(\xi,\psi,\zeta)\} = F(\vec{\Xi}) = \int_{-\infty}^{+\infty} e^{-\vec{\xi}\cdot\vec{\Xi}} f(\vec{\xi})\ \mathrm{d}x. \tag{9}$$

The eponymous cumulants of the method are defined as

$$c_{\alpha\beta\gamma} = (-c)^{-\alpha-\beta-\gamma}\frac{\partial^\alpha\partial^\beta\partial^\gamma}{\partial\xi^\alpha\partial\Psi^\beta Z\partial^\gamma}\ln(F(\Xi,\Psi,Z))|_{\Xi=\Psi=Z=0}. \tag{10}$$

Herein $(\alpha\beta\gamma) \in (0,1,2)$ each, whereby a total of 27 cumulant moments are generated with the highest order of 6. Due to the complexity, the computation of cumulants based on (10) is costly. A simpler alternative refers to the reconstruction of cumulants through central moments $\kappa_{\alpha\beta\gamma}$, which involves the velocity vector u_i, the lattice speed c, and the PDFs f_{ijk}

$$\kappa_{\alpha\beta\gamma} = \sum_{i,j,k}(i-u/c)^\alpha\ (j-v/c)^\beta\ (k-w/c)^\gamma\ f_{ijk}. \tag{11}$$

Details of the related reconstruction from central moments employed in the present work are outlined by Geier et al.[16] Once the cumulants are computed, the collision is executed in cumulant space. The postcollision cumulants read

$$C^*_{\alpha\beta\gamma} = C^{\mathrm{eq}}_{\alpha\beta\gamma} + (1-\omega_{\alpha\beta\gamma})\ C_{\alpha\beta\gamma}, \tag{12}$$

where the asterisk expresses the post collision states, $\omega_{\alpha\beta\gamma}$ represents the order-dependent relaxation rates and $C_{\alpha\beta\gamma} = c_{\alpha\beta\gamma}\ \rho$. While $C_{\alpha\beta\gamma}$ represents precollision cumulant states, $C^{\mathrm{eq}}_{\alpha\beta\gamma}$ denotes their equilibria. It is to be noted that only three second-order equilibria (C^{eq}_{200}, C^{eq}_{020}, and C^{eq}_{002}) and all fourth-order cumulant equilibria differ from zero for the utilized WP cumulant collision operator.

Relaxation rates

Equation (12) features a total of 27 relaxation rates $\omega_{\alpha\beta\gamma}$ of which 10 are independent of each other, $\omega_1 \cdots \omega_{10}$. For the WP cumulant collision, the most influential rate ω_1 addresses both second- and fourth-order collision. The relaxation rate ω_2 occurs in the nonzero second-order equilibria. While ω_3, ω_4, and ω_5 are related to third-order collision, the rates ω_6, ω_7, and ω_8 address fourth-order collision. Fifth- and sixth-order relaxation of the cumulant nonequilibrium parts are controlled by ω_9 and ω_{10}, respectively. The properties of the underlying fluid determine only the relaxation rate ω_1, which is its (shear) viscosity via

$$\omega_1 = \frac{1}{\nu/c_s^2 + \Delta t/2}. \tag{13}$$

The remaining nine relaxation rates ω_2 to ω_{10} can be chosen within the interval $[0, 2]$. The choice affects both the accuracy and numerical stability. Assigning all nine rates to unity is accompanied by beneficial stability for high Reynolds number flows due to the associated introduction of numerical damping. However, this choice is detrimental to the attainable accuracy beyond a sufficiently fine spatial/temporal resolution. Geier et al.[16] report an improvement of the method's diffusive order up to an order of four, derived from an optimization of the leading error of the collision operator. The optimization provides parameterized formulations for the three relaxation rates ω_3 to ω_5, which are responsible for the third-order collision, and two additional coefficients A and B are of influence for the fourth-order cumulant equilibria, compare Appendix B.2 for details. All five expressions are determined from ω_1 and ω_2,

$$\omega_3 = \frac{8\,(\omega_1 - 2)\,(\omega_2\,(3\,\omega_1 - 1) - 5\,\omega_1)}{8\,(5 - 2\,\omega_1)\,\omega_1 + \omega_2\,(8 + \omega_1\,(9\,\omega_1 - 26))}, \tag{14}$$

$$\omega_4 = \frac{8\,(\omega_1 - 2)\,(\omega_1 + \omega_2\,(3\,\omega_1 - 7))}{\omega_2\,(56 - 42\,\omega_1 + 9\,\omega_1^2) - 8\,\omega_1}, \tag{15}$$

$$\omega_5 = \frac{24\,(\omega_1 - 2)\,(4\,\omega_1^2 + \omega_1\,\omega_2\,(18 - 13\,\omega_1) + \omega_2^2\,(2 + \omega_1\,(6\,\omega_1 - 11)))}{16\,\omega_1^2\,(\omega_1 - 6) - 2\,\omega_1\,\omega_2\,(216 + 5\,\omega_1\,(9\,\omega_1 - 46)) + \omega_2^2\,(\omega_1\,(3\omega_1 - 10)\,(15\,\omega_1 - 28) - 48)}, \tag{16}$$

$$A = \frac{4\,\omega_1^2 + 2\,\omega_1\,\omega_2\,(\omega_1 - 6) + \omega_2^2\,(\omega_1\,(10 - 3\,\omega_1) - 4)}{(\omega_1 - \omega_2)\,(\omega_2\,(2 + 3\,\omega_1) - 8\,\omega_1)}, \tag{17}$$

$$B = \frac{4\,\omega_1\,\omega_2\,(9\,\omega_1 - 16) - 4\,\omega_1^2 - 2\,\omega_2^2\,(2 + 9\,\omega_1\,(\omega_1 - 2))}{3\,(\omega_1 - \omega_2)\,(\omega_2\,(2 + 3\,\omega_1) - 8\,\omega_1)}. \tag{18}$$

Mind that the relaxation rate ω_2, theoretically linked to the bulk viscosity, is assigned to unity within our study, such as ω_6 to ω_{10}. In the low viscosity (high Reynolds number) limit one obtains $\omega_1 \to 2$ from (13), which in turn yields

$$\lim_{\nu \to 0} \omega_\varepsilon(\omega_1, \omega_2)\Big|_{\varepsilon=\{3,4,5\}} = 0 \tag{19}$$

from (14)–(16), and has a detrimental effect on the numerical stability. To regularize the expressions (14)–(16) at low viscosities, Geier et al.[16] suggested a limiter for the third-order relaxation rates. In conclusion, seven limited relaxation rates occur, defined as

$$\omega_{3,1}^{\lambda} = \omega_3 + \frac{(1 - \omega_3)\,|C_{120} + C_{102}|}{\rho\,\lambda + |C_{120} + C_{102}|}, \tag{20}$$

$$\omega_{4,1}^{\lambda} = \omega_4 + \frac{(1 - \omega_4)\,|C_{120} - C_{102}|}{\rho\,\lambda + |C_{120} - C_{102}|}, \tag{21}$$

$$\omega_{3,2}^{\lambda} = \omega_3 + \frac{(1 - \omega_3)\,|C_{210} + C_{012}|}{\rho\,\lambda + |C_{210} + C_{012}|}, \tag{22}$$

$$\omega_{4,2}^{\lambda} = \omega_4 + \frac{(1 - \omega_4)\,|C_{210} - C_{012}|}{\rho\,\lambda + |C_{210} - C_{012}|}, \tag{23}$$

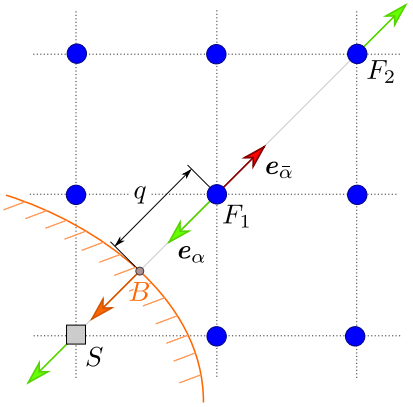

FIGURE 4 Illustration of the no-slip wall boundary condition [Colour figure can be viewed at wileyonlinelibrary.com]

$$\omega_{3,3}^{\lambda} = \omega_3 + \frac{(1-\omega_3)\ |C_{201}+C_{021}|}{\rho\ \lambda + |C_{201}+C_{021}|}, \tag{24}$$

$$\omega_{4,3}^{\lambda} = \omega_4 + \frac{(1-\omega_4)\ |C_{201}-C_{021}|}{\rho\ \lambda + |C_{201}-C_{021}|}, \tag{25}$$

$$\omega_{5}^{\lambda} = \omega_5 + \frac{(1-\omega_5)\ |C_{111}|}{\rho\ \lambda + |C_{111}|}, \tag{26}$$

where λ refers to an adjustable free parameter. As already mentioned, the default value is assigned to $\lambda_{\text{def}} = 10^{-2}$. For small products $\rho\ \lambda$, the optimized relaxation rate converges to 1 and therefore to the AO variant. For large values the limiter has virtually no effect, $\omega_{\varepsilon,k}^{\lambda} = \omega_{\varepsilon}$.

Owing to $\lambda_{\text{def}} = 10^{-2}$, one would intuitively expect the cumulant magnitude expressions in (20)–(26) to reach up to values around 10^{-2} or higher. However, the present results reveal peak values around 10^{-3} for coarser resolutions, which indicates that subtle changes of ω_i in the order of 1% in the direction of AO are of distinct significance. The latter is understood by the generally low values of the higher-order relaxation rates, which are around $\omega_{\varepsilon} \approx \mathcal{O}(10^{-3}) - \mathcal{O}(10^{-2})$. Essentially, one can observe a strong link between the resolution and the cumulant magnitude expressions. Likewise, a very weak link between these expressions and changes of the Reynolds number is seen. A weak proportionality is observed when attention is directed to the nonlinear interaction between the cumulant magnitude expressions observed for a variation of the limiter value λ.

2.3 | Wall boundary condition

Figure 4 depicts a cutout of the Cartesian grid where the continuous boundary (B) separates the solid nodes S of the discretized geometry from the fluid nodes F. The illustrated vectors correspond to the particle distributions (PDF) of the discrete velocity space $\boldsymbol{e}$, compare (4). Omitting the three directional indices, α denotes the opposite of wall-normal direction $\overline{\alpha}$. The PDF moving outwards of the solid wall into the direction of the first fluid node (F_1) is unknown, that is, $f_{\overline{\alpha}}(F_1)$. The corresponding direction is illustrated in red and the subgrid distance[51], defining the distance in $\boldsymbol{e}_{\alpha}$ direction between the continuous solid boundary (wall) and the first fluid node, is depicted by the scalar value $q \in [0, 1)$. The PDF directions marked in green are known properties since they constitute valid poststreaming states received from their next neighbor nodes. It is noted that all PDFs are accessed at the same discrete time step, which is why its explicit indication is omitted.

The employed boundary condition (BC) complies with the second-order accurate unified boundary treatment proposed by Yu et al.[52] as a modification of a BC introduced by Bouzidi et al.[53] which has also been applied in an amended version by Geier et al.[15] solely based on using postcollision PDFs of the local node bypassing the need to access neighboring node information.

The sequence of the applied BC starts from a linear interpolation of the PDF located at the wall in α-direction (orange vector) via

$$f_\alpha(B) = f_\alpha(F_1) + q\left[f_\alpha(S) - f_\alpha(F_1)\right]. \tag{27}$$

using the information of the first fluid node (F_1) and the corresponding solid node (S). In order to satisfy the momentum balance in the direction of α and to fulfill the no-slip boundary condition on the surface of the geometry, requiring zero velocity on the wall, the inverse ($\overline{\alpha}$) value is set to $f_{\overline{\alpha}}(B) = f_\alpha(B)$ and the unknown value follows from

$$f_{\overline{\alpha}}(F_1) = \frac{1}{1+q} f_{\overline{\alpha}}(B) + \frac{q}{1+q} f_{\overline{\alpha}}(F_2). \tag{28}$$

3 | COMPUTATIONAL STRATEGY AND DATA PROCESSING

This section covers (i) details of the scaling between physical and LB units, (ii) describes the adjustment of the body force used to match the targeted Reynolds number, and (iii) briefly outlines data processing aspects as well as (iv) the underlying grid layout.

3.1 | Scaling and Reynolds number adjustment

The Reynolds numbers (1) defined by physical (SI) and LB units agree, from which

$$\nu_{\mathrm{LB}} = \frac{u_{B,\mathrm{LB}}\, N_H}{\mathrm{Re}} \quad [-] \tag{29}$$

applies. Here N_H corresponds to the discrete number of lattice nodes distributed over the hill height H, and the associated physical spacing corresponds to $\Delta x_{\mathrm{SI}} = H/N_H$ [m], with $H = 0.05$ [m]. In the remainder of the article, the spatial discretization is referred to by specifying the discretization of the hill height N_H. The parameter $u_{B,\mathrm{LB}}$ of (29) relates to the nondimensional bulk velocity of the LB context and is linked to the Mach number (Ma) by $u_{B,\mathrm{LB}} = \mathrm{Ma}/\sqrt{3}$ [-]. As a result, the physical time increment is recovered by $\Delta t_{\mathrm{SI}} = \Delta x_{\mathrm{SI}}/\Lambda_u$ [s] with the velocity scaling factor $\Lambda_u = u_{B,\mathrm{SI}}/u_{B,\mathrm{LB}}$ [m/s] and $u_{B,\mathrm{SI}}$ following from Equation (1) with $\nu_{\mathrm{SI}} = 1.01 \times 10^{-6}$ [m^2/s]. Thus, the three parameters specifying the simulation are Re, N_H, and Ma. The required simulation time is quantified by the so-called (nondimensional) flow-through time

$$\mathrm{FT} = \frac{9\, N_H}{u_{B,\mathrm{LB}}\, \Delta t_{\mathrm{LB}}} \quad [-], \tag{30}$$

which comprises the number of discrete time steps needed to advect a particle with the bulk velocity through the domain. Appropriate multiples of FT are used to ensure the statistical convergence of the processed results, compare Section 3.2. FT is independent of the Reynolds number and only depends on the particular spatial (N_H) and temporal (Ma) discretization.

The investigated flow is driven by a pressure gradient $\partial p/\partial x$ acting in the longitudinal direction. The pressure gradient is imposed as a homogeneous body force $F_{x,\mathrm{LB}}$, which is adjusted during runtime. To this end, an initial value is iteratively found during the preceding transient phase of the simulation. Subsequently, a reconciliation between the current Re and the targeted Re$_t$ is carried out ten times per FT. The latter employs the computation of an averaged inlet-plane velocity as described in (1). If the magnitude of the deviation between both Reynolds numbers exceeds 1.5%, the body force is scaled by $F_{x,\mathrm{LB}} = F_{x,\mathrm{LB}}(1 - 0.1\mathrm{Re}_{\%})$. This approach was found to be both robust and accurate enough to limit the Reynolds number deviations to the order of $\mathcal{O}(‰)$.

3.2 | Data recording

The simulation process includes an initial transient period of 50 flow-through times. The initial period is followed by another 50 FT to converge the temporally averaged velocity vector $\overline{u}_i = (\overline{u}, \overline{v}, \overline{w})^{\intercal}$ as indicated by the bar. Subsequently,

the computation of the Reynolds stresses ($\overline{u_i' u_i'}$) is performed for approximately 100 FT. Thus, each simulation covers around 200 FT. In accordance with reference data sets sourced from Reference 24, mean velocity and Reynolds stress profiles are evaluated at ten different axial locations, see Figure 5. Profiles are obtained from the temporally averaged flow field, which is also spatially averaged in the homogeneous lateral (z) direction. Results are compared with experiments and data reported from two different Navier–Stokes procedures, namely, *LESOCC*[25] based on curvilinear grids and *MGLET*[26] developed for nonequidistant Cartesian grids, compare Table 1. LES reference solutions employ the well-known (dynamic) Smagorinsky model with van Driest damping near solid walls. Additionally, instantaneous velocity data is recorded at four different characteristic points of the flow field over 150 FT to compute the energy spectra, compare Table 2 and Figure 5.

3.3 | Spatial and temporal resolution

All utilized grids refer to homogeneous isotropic Cartesian grids. The baseline (medium) grid discretizes the height of the hill with $N_H = 28$ nodes. With this choice, the distance between the bottom and top wall H_{BT} also corresponds to

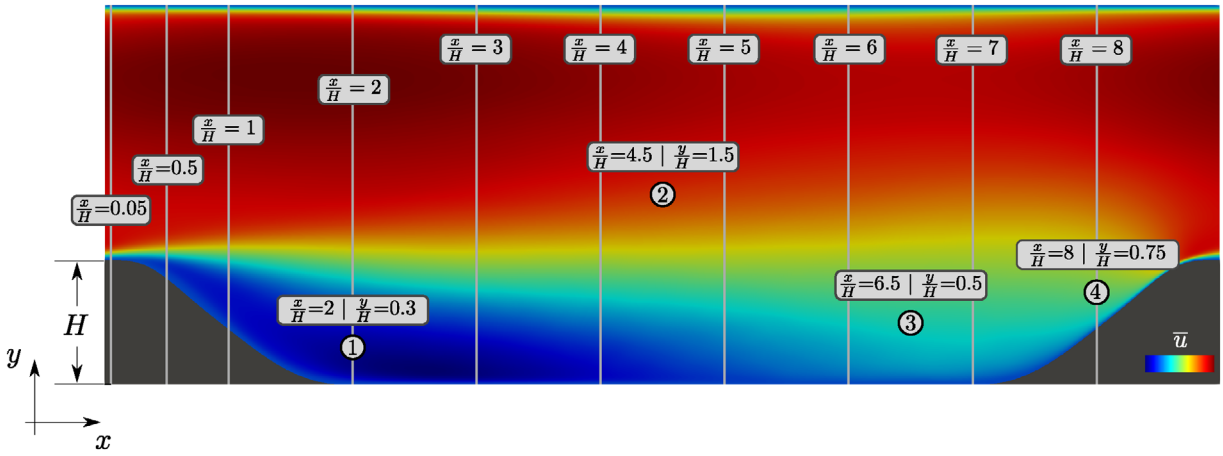

FIGURE 5 Locations of averaged profiles (lines) and instantaneous quantities (points) in the central x-y plane of the domain [Colour figure can be viewed at wileyonlinelibrary.com]

TABLE 1 Utilized reference data sets with a classification of turbulence treatment and grid size

Re	Solver	Classification	$\sum N_i$ [×10⁶]
700	LESOCC	DNS	13.1
2800	LESOCC & MGLET	DNS	13.1 & 48.0
10,600	MGLET	LES	4.1
37,000	MGLET	LES	4.1

TABLE 2 Point probe positions for the instantaneous velocity recordings in the central x-y plane

Identifier	Position - $(x,y)/H$	Flow characteristics
P-1	(2 , 0.3)	Recirculation regime
P-2	(4.5 , 1.5)	Core flow
P-3	(6.5 , 0.5)	Reattached flow
P-4	(8 , 0.75)	Accelerated flow

even multiples of the step size $\Delta x_{28} = 1.786 \times 10^{-3}$ [m] with $N_{BT} = 85$. In this grid, the subgrid distance mentioned in Section 2.3 matches $q_{H\,|\,T\,|\,B} = 0.5$ at the crest of the hill ($x = 0$), the top wall, and the plane lower part of the bottom wall ($1.93 \leq x/H \leq 7.07$). The grid arrangement aims to suppress influences from $q \neq 0.5$, which can thus only occur at the curved hill boundary sections. Doubling the number of lattice nodes to $N_H = 56$ results in a refined grid that satisfies the stated $q = 0.5$ condition.

Coarsening the $N_H = 28$ grid, no configuration can be found for which integer multiples between both H and H_{BT} exist. Applying a consistent refinement level of two leads to $N_H = 14$, whereby the H_{BT} discretization corresponds to $N_{BT} = 42.5$ which results in $q_T = 0$ for $q_{H\,|\,B} = 0.5$. Therefore, the top wall is virtually shifted by $\Delta x_{14}/2$ to maintain $q_T = 0.5$, increasing the domain height by 1.15% and $N_{BT} = 43$. Details of the investigated grids, including the number of lattice nodes and the number of discrete time steps per flow-through time (FT), for a baseline temporal resolution of Ma = 1/30, are given in Table 3. Note that $N_y = N_{BT} + 2$ applies due to the consideration of the additional solid boundary nodes, whereas N_x and N_z match $9H$ resp. $4.5H$ owing to periodicity. In addition to investigations of the diffusive scaling, that is, an N_H variation, we also report an analysis concerning acoustic scaling through a Ma variation. The baseline temporal resolution refers to the Mach number of Ma = 1/30. Scaling by a factor of three results in a finer (Ma = 1/90) and a respectively coarser (Ma = 1/10) temporal resolution. While linear relations, $\nu_{\mathrm{LB}} \propto (\Delta N_H)$ and $\overline{F}_{x,\mathrm{LB}} \propto (\Delta N_H)$, apply for diffusive scaling, the acoustic scaling deviates by featuring a quadratic dependence on $\overline{F}_{x,\mathrm{LB}} \propto \left(\Delta \mathrm{Ma}^2\right)$, whereas $\nu_{\mathrm{LB}} \propto (\Delta \mathrm{Ma})$ holds.

Table 4 offers an overview of the main parameters for the investigation of the baseline Reynolds number Re = 2800 in conjunction with diffusive (column-wise) and acoustic (row-wise) scaling using $\lambda_{\mathrm{def}} = 10^{-2}$. Mind that the experienced deviations from the target Reynolds numbers are fairly small.

3.4 | Turbulent flow analysis

The evaluation of turbulent structures is based on the analyzes of the power spectral density (*PSD*) data at distinct point locations and the anisotropy of the Reynolds stress tensor for exemplary one-dimensional profiles.

TABLE 3 Investigated grids and related time steps per flow-through time (FT) at Ma = 1/30

N_H	$N_x \times N_y \times N_z$	$\sum N_i$	FT
14	$126 \times 45 \times 63$	357,210	6,547
28	$252 \times 87 \times 126$	2,762,424	13,094
56	$504 \times 172 \times 252$	21,845,376	26,188

TABLE 4 Simulation parameters for the baseline Reynolds number Re = 2800 using the default limiter value $\lambda_{\mathrm{def}} = 10^{-2}$ under acoustic and diffusive scaling

		$N_H = 14$	$N_H = 28$	$N_H = 56$
Ma = 1/10	ν_{LB}	2.89×10^{-4}	5.77×10^{-4}	1.15×10^{-3}
	$\overline{F_{x\mathrm{LB}}}$	3.10×10^{-6}	1.49×10^{-6}	7.07×10^{-7}
	$\overline{\mathrm{Re}}$	2799.4 (−0.02%)	2802.2 (+0.08%)	2798.0 (−0.07%)
Ma = 1/30	ν_{LB}	9.62×10^{-5}	1.92×10^{-4}	3.85×10^{-4}
	$\overline{F_{x\mathrm{LB}}}$	3.56×10^{-7}	1.63×10^{-7}	7.85×10^{-8}
	$\overline{\mathrm{Re}}$	2801.5 (+0.05%)	2799.5 (−0.02%)	2796.4 (−0.13%)
Ma = 1/90	ν_{LB}	3.21×10^{-5}	6.41×10^{-5}	1.28×10^{-4}
	$\overline{F_{x\mathrm{LB}}}$	3.94×10^{-8}	1.89×10^{-8}	9.00×10^{-9}
	$\overline{\mathrm{Re}}$	2801.1 (+0.04%)	2806.8 (+0.24%)	2802.4 (+0.09%)

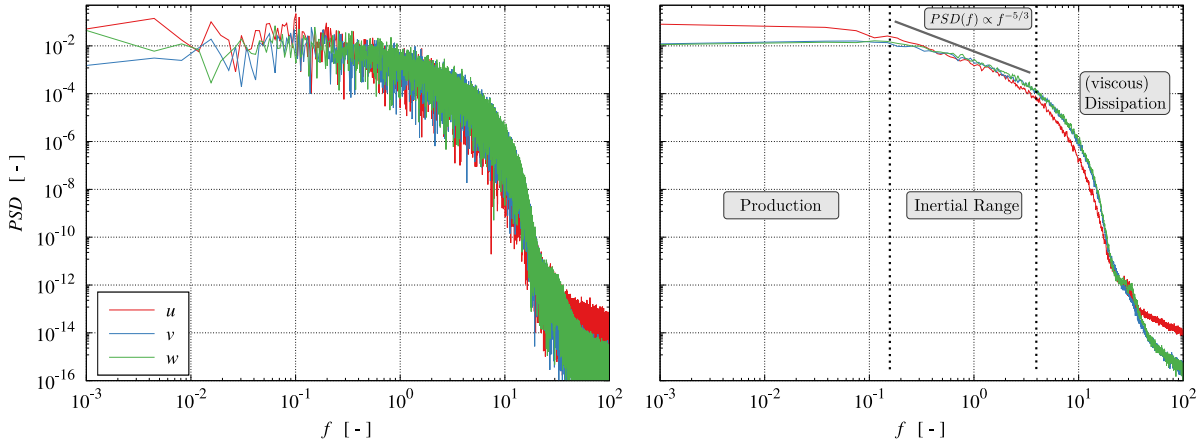

(A) Raw data plots featuring all DFT data points

(B) Moving average filtered data set (filter width: 100 discrete frequency contributions)

FIGURE 6 Power spectral density $PSD(f)$ of the three velocity components (u (red), v (blue) and w (green)) at P-2 (core flow) for the configuration Re = 2800, $N_H = 28$, Ma = 1/30, and $\lambda_{\text{def}} = 10^{-2}$ [Colour figure can be viewed at wileyonlinelibrary.com]

Energy spectra and filtering

The PSD follows from a discrete Fourier transform (DFT) of the instantaneous time series of the velocity components recorded at four different locations in the numerical domain, compare Table 2. The graphs provide information regarding the energy distribution of different scales. No comparison is performed with other research efforts as the related data is nonavailable. The data is processed to discuss the response of the cumulant LBM to the interplay between the resolution and the regularization parameter. In order to enable the comparison of different configurations, the displayed data is nondimensionalized with H and u_B, PSD [m^2/s] $/(u_B\, H)$ resp. f [1/s] $\cdot H/u_B$.

Figure 6A depicts the exemplary raw data $PSD(f)$ for all three velocity components extracted at location P-2 (core flow) for Re = 2800, $N_H = 28$, Ma = 1/30, and $\lambda_{\text{def}} = 10^{-2}$. Due to distinct oscillations, the comparison between the graphs is hampered, and a moving average filter is applied to the underlying DFT raw data. The filter width spans 100 discrete frequency contributions and the filtered $PSD(f)$ graphs are depicted in Figure 6B.

Reynolds stress invariant maps

A widespread approach to analyze turbulent structures is the visual evaluation using the Q-criterion introduced by Dubief et al.[54] Due to its qualitative nature, not all details can be revealed, and the present study opts to observe the tensor of (resolved) Reynolds stresses using anisotropy invariant maps (AIM). The starting point is the nondimensional anisotropy tensor[55,56]

$$a_{ij} = \frac{\overline{u_i'\, u_j'}}{2k} - \frac{\delta_{ij}}{3} \tag{31}$$

with $k = \overline{u_i'\, u_i'}/2$ representing the turbulent kinetic energy and δ_{ij} being the Kronecker delta. The graphical evaluation of the flow anisotropy introduced by Banerjee et al.[57] refers to plotting the invariants of a_{ij} in a two-dimensional space,

$$x_B = \Lambda_1 - \Lambda_2 + \frac{3}{2}\Lambda_3 + \frac{1}{2}, \tag{32}$$

$$y_B = \frac{\sqrt{27}}{2}\Lambda_3 + \frac{\sqrt{3}}{2}. \tag{33}$$

Herein x_B and y_B denote barycentric (B) coordinates and Λ_i are the eigenvalues of a_{ij}, sorted in descending order $\Lambda_1 \geq \Lambda_2 \geq \Lambda_3$. All possible points are bounded by an isosceles triangle whose vertices state one-component turbulence ($1c$ at [1,0]), isotropic two-component turbulence ($2c$ at [0,0]) and isotropic 3D turbulence ($3c$ at $[1/2,\sqrt{3}/2]$). The triangle edges indicate two-component turbulence ($\overline{2c-1c}$) and axisymmetric contraction ($\overline{3c-2c}$) or axisymmetric expansion ($\overline{1c-2c}$). The advantage of the barycentric map rests upon equal weighting of the vertex points, $1c$, $2c$, and $3c$ turbulence, whereby important details are crucially magnified. Further details will be given in Section 4.1.

3.5 | Error quantification

To allow for a code-to-code-verification of the predicted velocity and Reynolds stress profiles and assess the global flow field, a relative L_2 error norm of a specific flow quantity (ϑ) is introduced by

$$L^{\text{ref}}_{2,rel}(\vartheta)\Big|_{x/H} = \frac{\sum_{n=1}^{N_y}\left(\vartheta_{x/H}(n) - \vartheta^{\text{ref}}_{x/H}(n)\right)^2}{\sum_{n=1}^{N_y}\left(\vartheta^{\text{ref}}_{x/H}(n)\right)^2}. \tag{34}$$

To this end, a cubic spline interpolation of the available reference (ref) data sets[24] is taken as the ground truth, which is evaluated at each (n) discrete lattice node. As a result, each one-dimensional profile featuring N_y nodes is reduced to a single scalar. Graphs displayed in Section 4 include these ten (verification) "error" measures, one for each assessed x/H location, as well as their respective (unweighted) mean value to characterize the overall accuracy of the flow field prediction.

3.6 | Nondimensional wall distance

The classification of the grid resolution rests upon the nondimensional wall distance y^+. Its computation is based on the velocity gradient obtained at the first wall-adjacent fluid nodes using the averaged velocity vector components $\overline{u}$ and $\overline{v}$ in the centered x-y plane. The tangential part $\overline{u}_{\parallel}$ is obtained by subtracting the projection of the 2D components in the direction of the wall normal. The velocity gradient follows from $u_{\parallel}/q$ with q being the subgrid distance, see Figure 4. The corresponding wall shear stress, the friction velocity, and the nondimensional wall distance are defined from linear relations and get inaccurate beyond $y^+ \geq 12$. Their definitions read

$$\tau_w = \nu\,\frac{\overline{u}_{\parallel}}{q}, \quad u_\tau = \sqrt{\frac{|\tau_w|}{\rho}} \quad \text{and} \quad y^+ = \frac{u_\tau\, q}{\nu}. \tag{35}$$

Visualized data is smoothed by a centered unweighted moving average with five points to account for the Cartesian discretization of the hill geometry. Mind that the y^+-distribution is generally smooth along the top wall and the plain center section of the bottom wall, due to the imposed $q = 0.5$ criterion, compare Section 2.3. A rougher distribution is experienced alongside the curved segments of the lower wall, $x/H \leq 1.93$ and $x/H \geq 7.07$, where q varies. For $q = 0.5$, the evaluated y^+-distribution quantifies the resolution of the isotropic, homogeneous Cartesian grid by means of $\Delta x_i^+ \sim 2y^+$.

4 | RESULTS

The validation displayed in Section 4.1 refers to the results obtained for the chosen baseline Reynolds number of $\text{Re} = 2800$ combined with the fine grid ($N_H = 56$), the medium Mach number ($\text{Ma} = 1/30$), and the default regularization parameter value ($\lambda_{\text{def}} = 10^{-2}$). Subsequently, resolution studies for both acoustic (4.2) and diffusive scaling (4.3) are performed for $\text{Re} = 2800$, $\lambda_{\text{def}} = 10^{-2}$. Section 4.4 is devoted to assessing the influence of the regularization parameter for $\text{Re} = 2800$. Build upon the findings from Sections 4.1–4.4, results for the other Reynolds numbers are presented in Section 4.5.

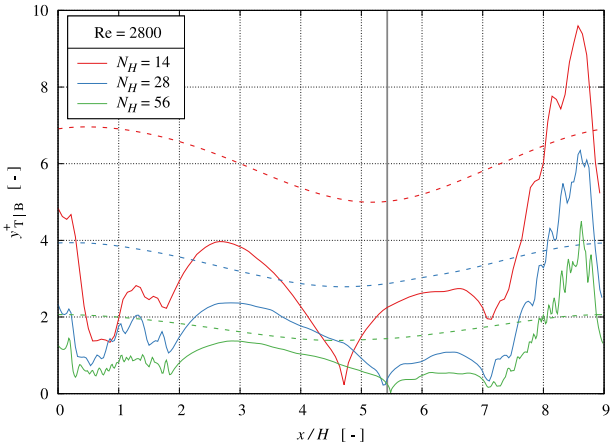

FIGURE 7 Nondimensional wall distance $y^+_{T|B}$ under diffusive scaling with $N_H = \{14; 28; 56\}$ at the bottom (solid) and top (dashed) wall for the parameter set Re = 2800, Ma = 1/30, and $\lambda_{def} = 10^{-2}$ [Colour figure can be viewed at wileyonlinelibrary.com]

4.1 | Baseline study for Re = 2800

Figure 7 displays the nondimensional wall distance $y^+_{T|B}$ of the wall-adjacent fluid lattice along the top (T - dashed lines) and bottom (B - solid lines) boundaries of the domain, obtained for Re = 2800, Ma = 1/30, and $\lambda_{def} = 10^{-2}$. The vertical gray line at $x/H = 5.43$ indicates the reattachment point (RP) position taken from Breuer et al.[33] and serves as the first indicator for the resolution quality. It is evident that the coarse grid RP prediction significantly deviates from the prediction of the other two grids, which both agree much better with the reference data.

The maximum $y^+_{T,max}$ values at the top wall occur above the crest, where the flow is accelerated, and refer to 7 (N_H=14), 4 (N_H=28) and 2 (N_H=56) wall units for the three grids. Due to the smaller velocities in the recirculation and reattachment region, the nondimensional resolution of the bottom wall is mostly better. However, it deteriorates when the flow accelerates ($x/H \gtrsim 7$), and the wall distances deviate from $q = 0.5$. The respective maxima refer to 10 (N_H=14), 6 (N_H=28), and 4 (N_H=56) wall units and occur shortly upstream of the crest. In conclusion, all three resolutions correspond to LES grids, and the fine grid, where the field lattice spacing is around $\Delta x_i^+ \approx 3$, is deemed close to a DNS resolution.

Averaged data

Figure 8 displays averaged profiles of the longitudinal velocity component (A) and the Reynolds shear stress (B) for Re = 2800. The presented mean flow quantities refer to the fine grid ($N_H = 56$), the medium temporal resolution (Ma = 1/30), and $\lambda_{def} = 10^{-2}$. They are in fair predictive agreement with the DNS reference data sets from *LESOCC* (red) and *MGLET* (blue). The depicted Reynolds shear stress components reveal minor deviations around the extreme values of the profiles located at $2 \leq x/H \leq 6$. Overall, the WP LBM provides a remarkable predictive agreement with DNS data when using the fine grid.

Turbulence quantities

Figure 9 shows the turbulent energy spectra $PSD(f)$ of the longitudinal, vertical, and lateral direction. Each figure includes four spectra corresponding to the four reference points of the flow field, compare Table 2. In large parts, the spectra for the acceleration (P-4) and the reattachment (P-3) location overlap. As expected from the relatively low Reynolds number of Re = 2800, the inertial subrange, featuring the classical $PSD(f) \propto f^{-5/3}$ proportionality, is restricted to a narrow frequency regime of $\Delta f_{inertial} \approx \mathcal{O}(10^1)$. The confinement is most pronounced in the recirculation regime (red), where the spectra' energy-containing and energy dissipating parts tend to overlap and are less severe for the core flow position (blue). The sloping toward the dissipation range is almost identical for the three velocity components. Some deviations of the energy levels are observed in the production range, where the lateral component displays the

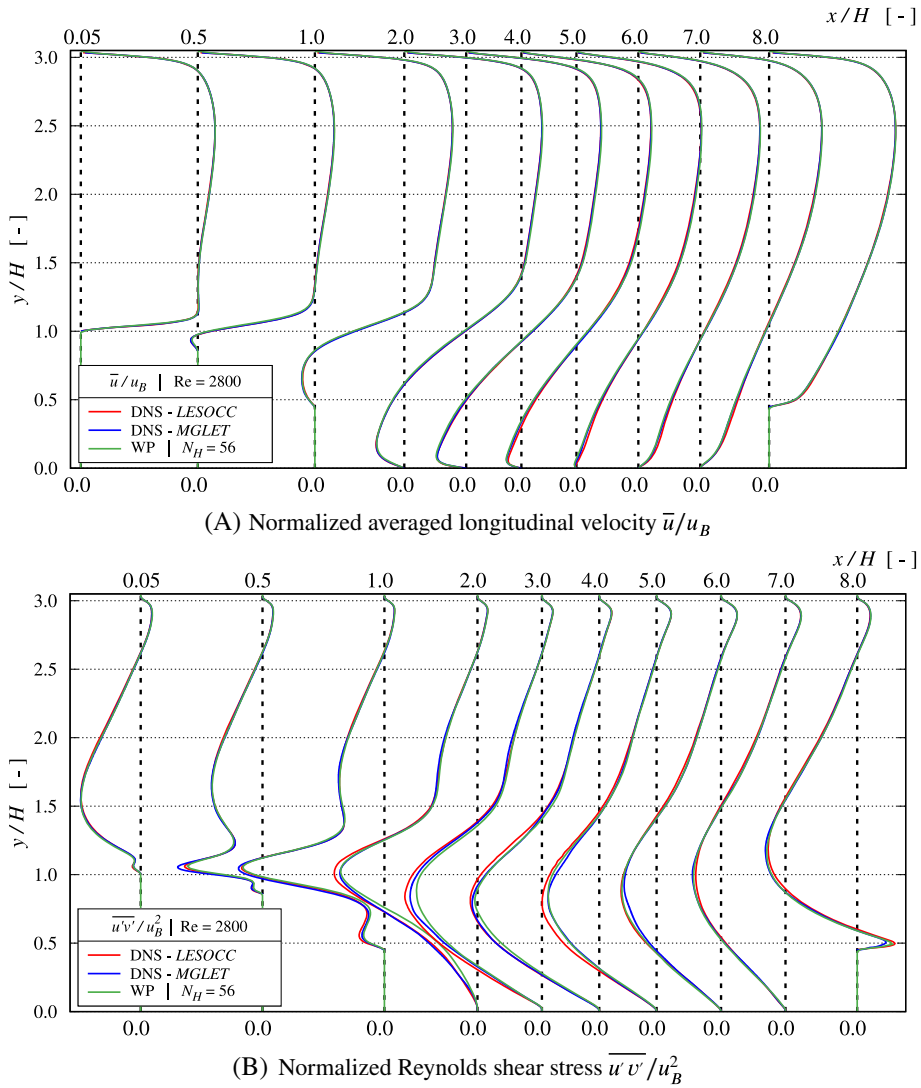

FIGURE 8 Comparison of averaged longitudinal velocities (top) and Reynolds shear stresses (bottom) predicted by the WP LBM ($N_H = 56$, Ma $= 1/30$, $\lambda_{\text{def}} = 10^{-2}$) and the reference DNS[24] data for Re $= 2800$ [Colour figure can be viewed at wileyonlinelibrary.com]

most distinct location-dependent variations, and the levels are generally augmented for the reattachment location (P-3), compare Figure 9C.

Figure 10 depicts anisotropy invariant maps (AIM) for four profiles located at $x/H = \{0.05; 0.5; 3; 6\}$. The representation of the discrete points distributed in y-direction employs a diverging color bar ranging from blue (bottom wall) to red (top wall). A commonality of all displayed maps includes the alignment of both wall near-wall regions with the two-component turbulence abscissa. As wall influences decrease, a trend toward isotropic 3c turbulence is formed and reaches a global y_B maximum in the upper region of the domain at approximately $y/H = 2/3$ (orange).

For the sake of clarity the detailed discussion of the AIM begins at $x/H = 6$ and is supported by characteristic markers added to Figure 10D. Close to the top wall, the trajectory [1] falls almost centered on the x-axis at $x_B = 0.45$. In this regime, the vertical fluctuation vanishes, and the longitudinal contribution exceeds the lateral one. Away from the wall, the boundary layer gradient $\mathrm{d}\overline{u}/\mathrm{d}y$ contributes to an increase of $\overline{u'^2}$ which shifts the trajectory in the 1c direction and yields the global x_B maximum [2]. Subsequently, the wall damping attenuates, and the vertical component $\overline{v'^2}$ develops [3]. The 3c trend ends at $y_B \approx 0.55$, where the AIM turns toward the right axisymmetric expansion edge of the triangle [4]. This is attributed to the longitudinal acceleration of the flow, whereby the lateral (w) dynamics gradually decrease concurrent to the decreasing influence of the top wall while the $\overline{u'^2}$ and $\overline{v'^2}$ are of a similar order of magnitude. In the center of the channel (green), the longitudinal component represents the major contribution [5]. As the lower wall is progressively

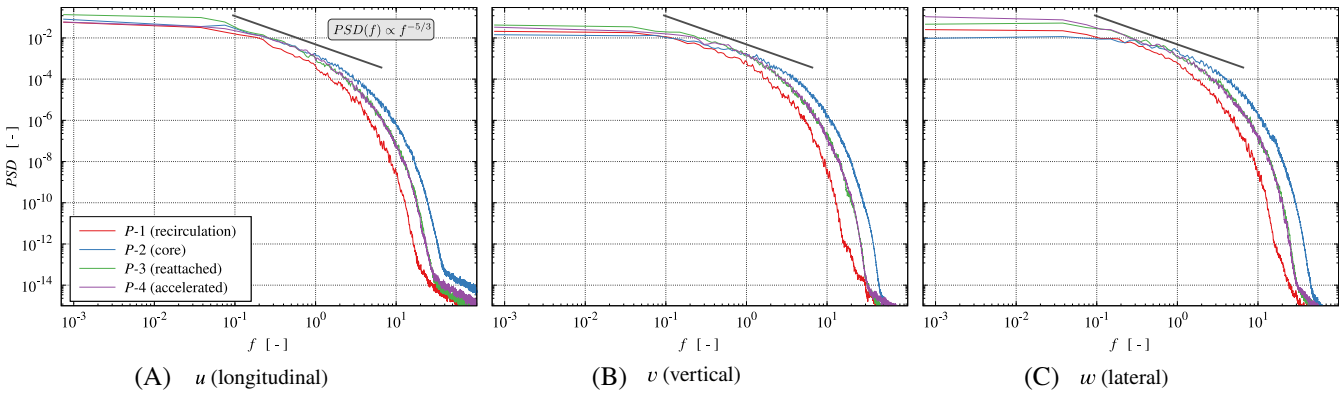

FIGURE 9 Computed turbulent energy spectra $PSD(f)$ of the three Cartesian velocity components evaluated at the four points outlined in Figure 5 for the parameter set Re = 2800, $N_H = 56$, Ma = 1/30, and $\lambda_{\text{def}} = 10^{-2}$ [Colour figure can be viewed at wileyonlinelibrary.com]

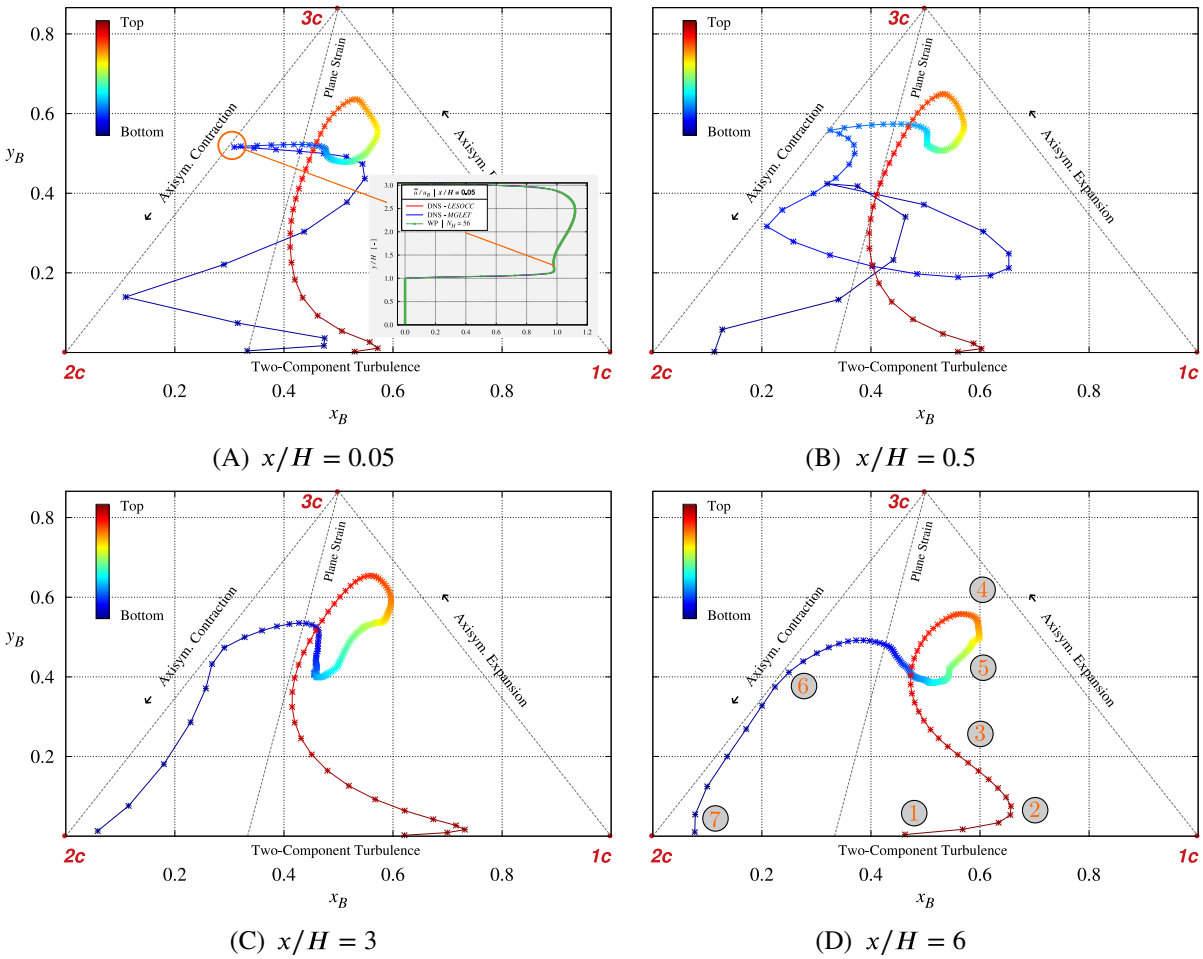

FIGURE 10 AIMs at four distinctive x/H positions for the parameter set Re = 2800, $N_H = 56$, Ma = 1/30, and $\lambda_{\text{def}} = 10^{-2}$ [Colour figure can be viewed at wileyonlinelibrary.com]

approached, the longitudinal and vertical normal stresses reduce, and the trajectory shifts toward the left edge associated with axisymmetric contraction [6]. The vertical normal stress component is negligible for $0.4 > y/H > 0.1$. The other two components are approximately equal and decrease at a similar rate as the bottom wall is approached. In the vicinity of the lower wall [7], a large gradient $\mathrm{d}\overline{u}/\mathrm{d}y$ feeds an augmented level of longitudinal normal stress.

The AIM trajectory (C) of the recirculation zone profile located at $x/H = 3$ displays two deviations from the map at $x/H = 6$. These include a more pronounced and sharper 1c trend at the top wall (red) region, in response to the stronger flow confinement, and a greater distance from the axisymmetric contraction limit within the bottom, recirculating flow, region (blue) after touching this edge where the gradient $\mathrm{d}\overline{u}/\mathrm{d}y$ vanishes in line with the $\overline{u}$ minimum, compare Figure 8A. Moving further upstream to $x/H = 0.5$ (B), the part of the trajectory that is, located inside or near the recirculation zone (blue to cyan) is characterized by significant and sudden changes of the Reynolds stress anisotropy, which agrees with either local extrema or inflection points. The AIM closest to the crest (A) displays features which are supported by the corresponding $\overline{u}$ velocity profile in Figure 8. Due to strong acceleration above the crest, the bottom wall branch is shifted toward the 1c state. The upper wall behavior follows the behavior seen in (B) and the footprint of the two vanishing primal velocity gradient positions close to the bottom wall is observed again.

4.2 | Acoustic scaling (Re = 2800)

To assess the sensitivity of the WP cumulant operator to the temporal resolution, three Mach numbers are investigated for the finest grid with $N_H = 56$, compare Table 4. Investigations employ $\lambda_{\mathrm{def}} = 10^{-2}$ and refer to the baseline value of $\mathrm{Ma} = 1/30$, as well as one larger ($\mathrm{Ma} = 1/10$) and one smaller ($\mathrm{Ma} = 1/90$) Mach number, respectively.

Averaged data

Figure 11 displays representative exemplary longitudinal velocity and Reynolds shear stress results at two positions of the flow field. While the left column shows a profile close to the separation point at the crest ($x/H = 0.5$), the right column refers to a location slightly downstream of the reattachment point ($x/H = 6$). The DNS-*MGLET* result (black line) serves as a reference. Predictive differences induced by the variation of the Mach number are small, and LB results agree reasonably well with the DNS results. A minor but noticeable deviation arises for the Reynolds shear stress, more distinct for the finest time step at $y/H = 0.85$.

A more comprehensive analysis assesses the relative L_2 error norm against reference DNS-*MGLET* results. Table 5 summarizes the (unweighted) integral error norms of the ten selected profiles for the longitudinal and vertical velocity component. Its almost constant value confirms the minor influence of the underlying temporal resolution. It is noted that spatial resolution changes do not alter this finding, and similar results were obtained from $N_H = 28$ or $N_H = 14$ but are not displayed to save the space. Moreover, and again not displayed to safe space, the AIMs shown in Figure 10 do not depict any significant differences in response to a Mach number variation.

Turbulent spectra

Supplementary to the averaged data, Figure 12 shows the $PSD(f)$ based on a DFT of the instantaneous velocity signal. To this end, the $PSD(f)$ of the longitudinal (u) component is exemplary depicted at two locations, in the core flow (P-2) and the reattaching flow (P-3), compare Figure 5. No substantial differences are observed between the three Mach numbers. Both the length and the slope of the inertial range are identical for all displayed spectra. Minor deviations in the high-frequency cut-off range are attributed to the data processing scheme and have no physical meaning.

4.3 | Diffusive scaling (Re = 2800)

The next part reports the sensitivity of the results to the spatial resolution, achieved by a variation of the resolution parameter N_H for the medium Mach number $\mathrm{Ma} = 1/30$ and the default regularization ($\lambda_{\mathrm{def}} = 10^{-2}$). Three consecutive resolutions are investigated, $N_H = \{14; 28; 56\}$, and compared with DNS-*MGLET* results.

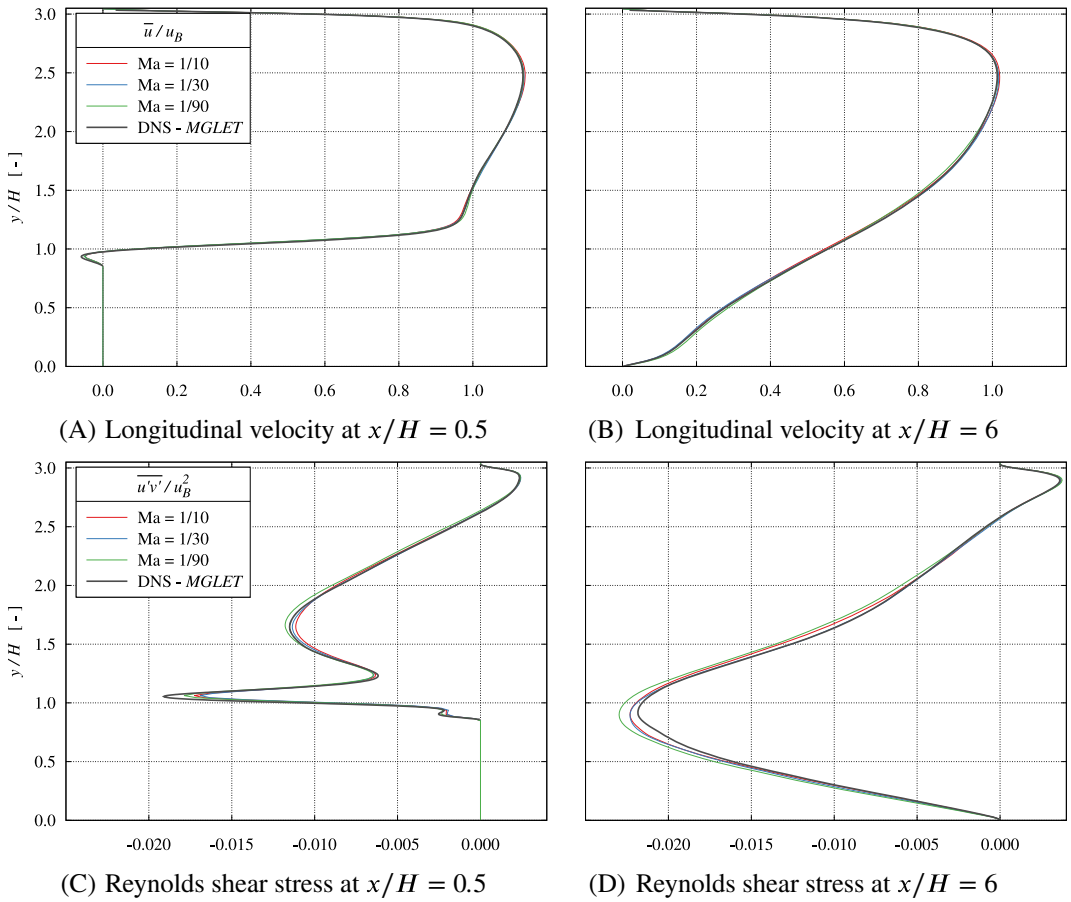

(A) Longitudinal velocity at $x/H = 0.5$ (B) Longitudinal velocity at $x/H = 6$

(C) Reynolds shear stress at $x/H = 0.5$ (D) Reynolds shear stress at $x/H = 6$

FIGURE 11 WP versus DNS- *MGLET* reference: averaged longitudinal velocity component $\overline{u}/u_B$ (left) and Reynolds shear stress $\overline{u'v'}/u_B^2$ (right) profiles under acoustic scaling with Ma = {1/10; 1/30; 1/90} exemplarily depicted at two positions (downstream locations close to the crest (left) and the reattachment point (right)) for Re = 2800, $N_H = 56$, and $\lambda_{\text{def}} = 10^{-2}$ [Colour figure can be viewed at wileyonlinelibrary.com]

TABLE 5 Relative integral $L_2(\vartheta)$ error norm (WP vs. DNS-*MGLET*) under acoustic scaling of selected flow quantities for the parameter set Re = 2800, $N_H = 56$, and $\lambda_{\text{def}} = 10^{-2}$

ϑ	Ma = 1/90	Ma = 1/30	Ma = 1/10
$\overline{u}/u_B$	7.71×10^{-3}	6.83×10^{-3}	7.61×10^{-3}
$\overline{v}/u_B$	5.15×10^{-2}	4.96×10^{-2}	4.20×10^{-2}

Averaged data

Figure 13 outlines the averaged flow results at four x/H locations. Compared with the DNS reference solution (black), the coarse grid results (red) significantly overpredict the longitudinal velocity component above the crest at $x/H = 0.05$ and $y/H \approx 1.2$ (A). This defect is due to under-resolving the thin boundary layer in the acceleration regime upstream the crest and mitigates with increasing wall distance for $y/H > 1.75$. The associated larger shear stress gradient magnitude (E) delays flow separation and no substantial recirculation regime is formed at $x/H = 0.5$ (B). At $x/H = 3$ (C) all mean velocity data agree. At the same time, Reynolds shear stress magnitudes predicted on the coarse grid reveal again larger gradients and peak values around the dividing streamline (G). This, in turn, enhances the recovery of the reattaching shear flow for the coarse grid at $x/H = 6$ (D). The predictive agreement of the fine grid $\overline{u}$-results with the reference solution is marginally better than the medium grid results in the recovery regime. These improvements also yield small changes in the upper boundary layer for continuity reasons.

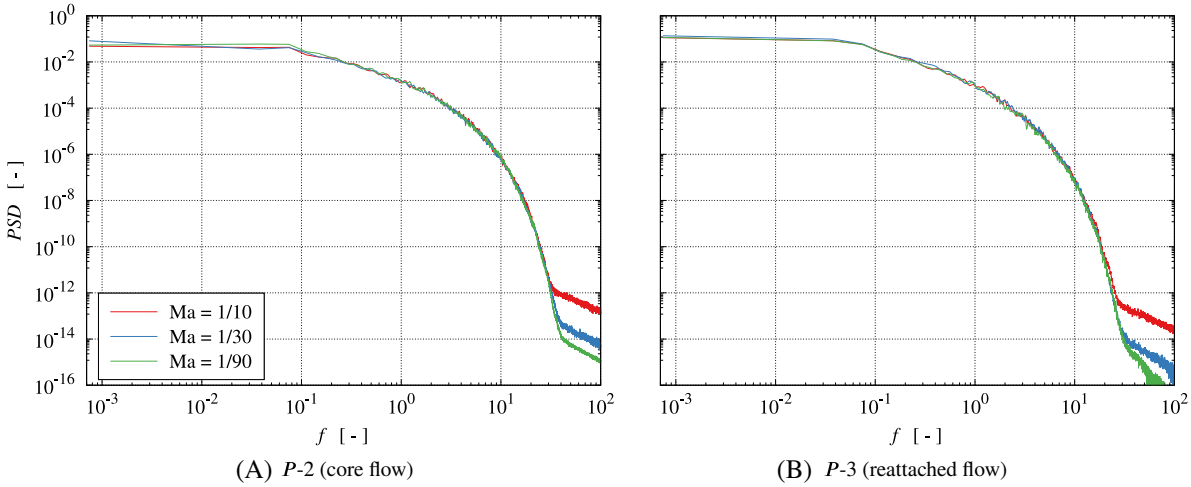

FIGURE 12 Longitudinal (u) turbulent energy spectra $PSD(f)$ under acoustic scaling with Ma $= \{1/10; 1/30; 1/90\}$ exemplarily depicted at two points for the parameter set Re $= 2800$, $N_H = 56$, and $\lambda_{\text{def}} = 10^{-2}$ [Colour figure can be viewed at wileyonlinelibrary.com]

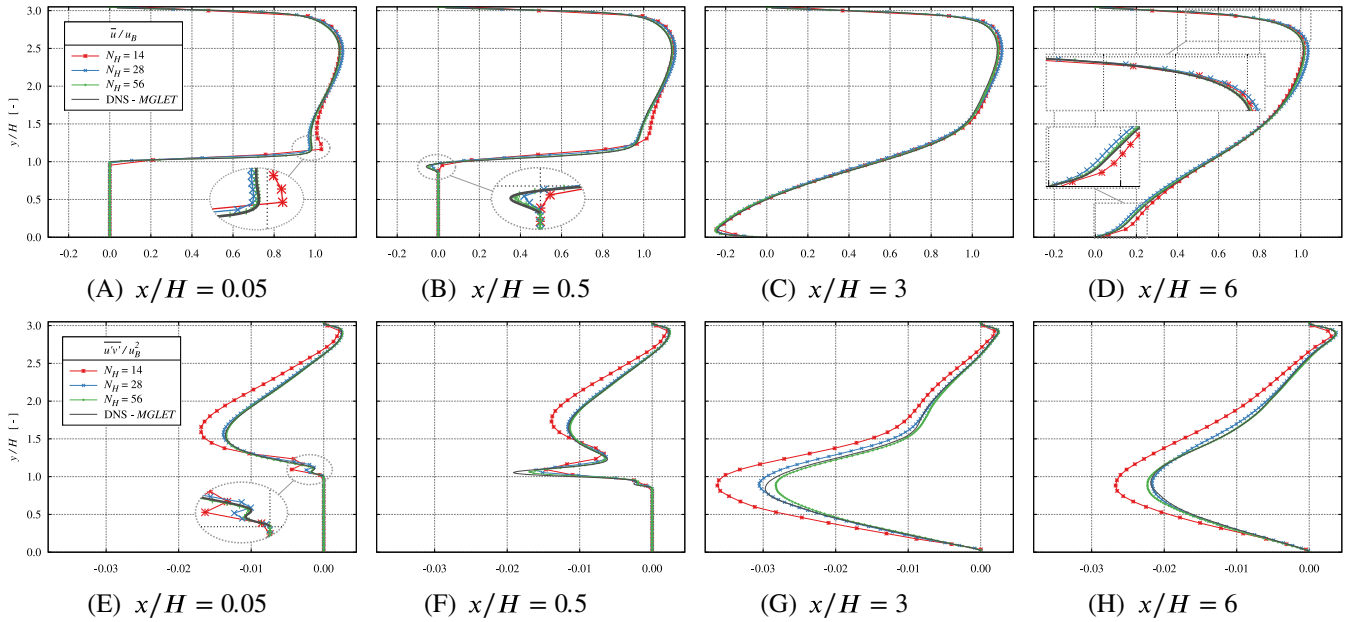

FIGURE 13 WP versus DNS-*MGLET* reference: averaged longitudinal velocity component $\overline{u}/u_B$ (top) and Reynolds shear stress $\overline{u'v'}/u_B^2$ (bottom) at four distinctive x/H positions under diffusive scaling with $N_H = \{14; 28; 56\}$ for the parameter set Re $= 2800$, Ma $= 1/30$, and $\lambda_{\text{def}} = 10^{-2}$ [Colour figure can be viewed at wileyonlinelibrary.com]

With attention given to the resolution influences on the integral L_2 error norm displayed in Figure 14, the more subtle vertical velocity component $\overline{v}$ depicts an almost linear dependency of the error norm across the total resolution spectrum. The dashed blue lines indicate the relative error norms for the ten selected profiles, and the solid red line represents their (unweighted) mean value. As could be expected by the Reynolds stresses displayed in Figure 13, they reveal a stronger sensitivity to the resolution, which is of the order two in the coarse grid regime and lower in the fine grid regime. This trend is representative and also relates to the influence of the limiter λ, as will be outlined in Section 4.4.

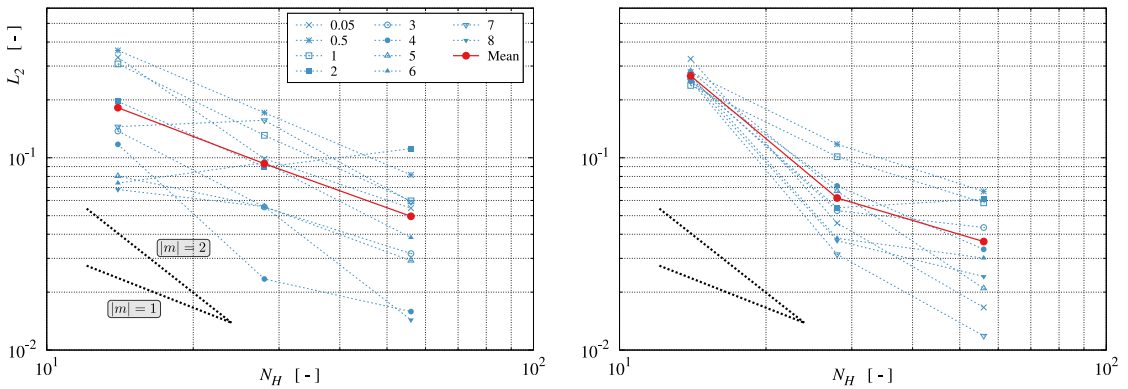

(A) Vertical velocity $\overline{v}/u_B$ (B) Reynolds shear stress $\overline{u'v'}/u_B^2$

FIGURE 14 Relative L_2 error norm (WP vs. DNS-*MGLET*) of selected flow quantities under diffusive scaling with $N_H = \{14; 28; 56\}$ for the parameter set of Re = 2800, Ma = 1/30, and $\lambda_{\text{def}} = 10^{-2}$ [Colour figure can be viewed at wileyonlinelibrary.com]

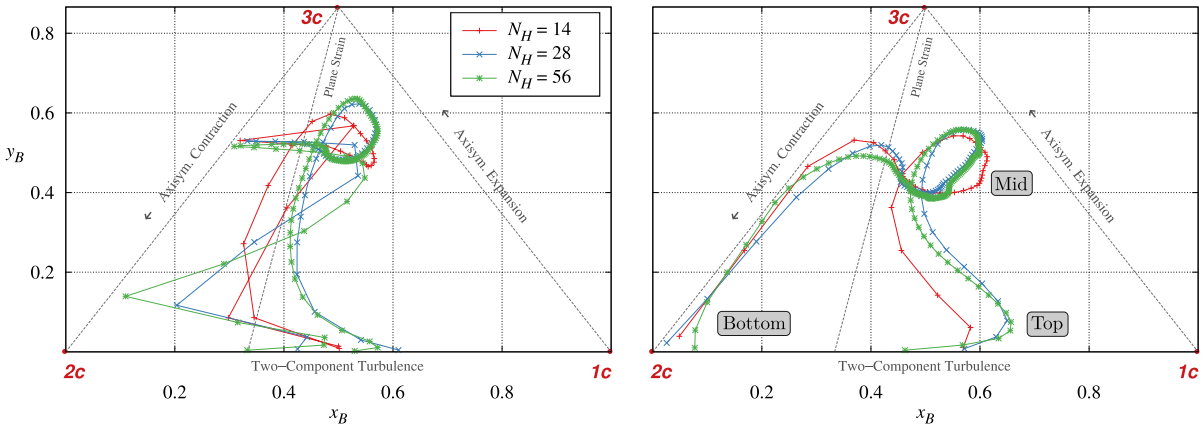

(A) $x/H = 0.05$ (B) $x/H = 6$

FIGURE 15 Influence of diffusive scaling $N_H = \{14; 28; 56\}$ on the Reynolds stress anisotropies depicted at two positions,downstream locations close to the crest (left) and the reattachment point (right), for the parameter set Re = 2800, Ma = 1/30, and $\lambda_{\text{def}} = 10^{-2}$ [Colour figure can be viewed at wileyonlinelibrary.com]

Turbulent structures

The observation made for the averaged data are confirmed by the AIM trajectories depicted in Figure 15 for a near crest location at $x/H = 0.05$ (A) and a recovery location at $x/H = 6$ (B). Resolution-related differences are more pronounced for the near crest location, where the reduction of the resolution confines the AIM pathway toward the vicinity of the plane strain line, and at least one of the eigenvalues equals zero. The axisymmetric states above the bottom wall are not well resolved. Moreover, the augmentation of the primary normal stress component close to the top wall and the related shift toward the one-component regime is suppressed, particularly at $x/H = 6$. Much smaller deviations between the medium and the fine grid are seen for all the above-discussed aspects. In general, the ability to resolve flow anisotropies is enhanced with the resolution. This observance might hint at an earlier onset of dissipative structures in frequency space and a corresponding reduction of the inertial range when coarsening the grid.

Figure 16 shows the predicted turbulent spectra obtained for all three velocity components at a core flow location *P*-2, compare Figure 5. The graphs reveal a shift of the upper end of the inertia regime by almost one order of magnitude when increasing the resolution from $N_H = 14$ to $N_H = 56$. Comparing the medium and the fine grid, a more gradual onset of dissipative influences is observed in combination with a small increase of the upper inertial subrange frequency for

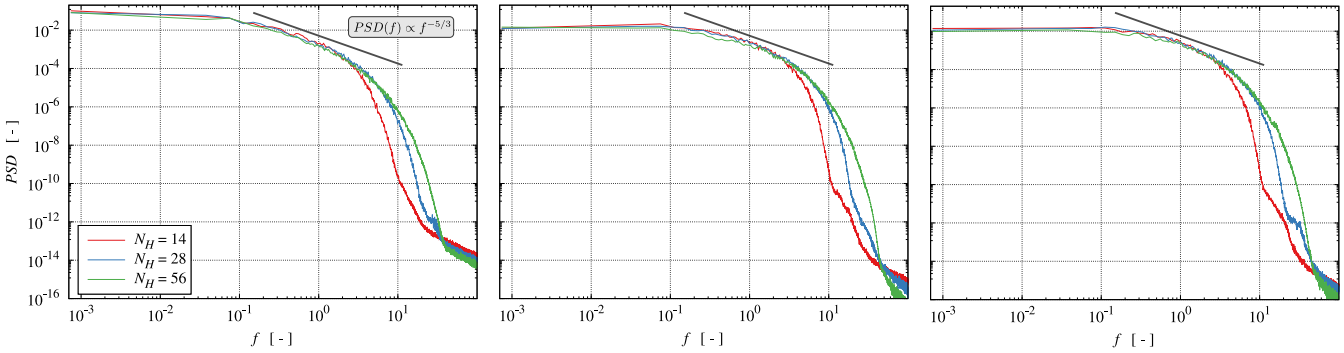

(A) u (longitudinal) (B) v (vertical) (C) w (lateral)

FIGURE 16 Turbulent energy spectra $PSD(f)$ under diffusive scaling with $N_H = \{14; 28; 56\}$ exemplarily depicted at P-2 (core flow) for the parameter set Re = 2800, Ma = 1/30, and $\lambda_{\text{def}} = 10^{-2}$ [Colour figure can be viewed at wileyonlinelibrary.com]

the fine grid. The resolution-induced differences are similar for other locations, albeit slightly more pronounced for the recirculation regime (P-1).

We also show illustrative snapshots of the velocity magnitude and the averaged (resolved) turbulent kinetic energy in the centered x-y plane for all three resolutions in Figure 17. Apparently, the coarse mesh ($N_H = 14$; top row) features relatively large structures and misses many details. As outlined by the black boxes in Figure 17A, the coarse grid simulation fails to resolve the shear layer while approaching the crest of the hill at the downstream end of the domain. For the coarse grid, the large structures are associated with a stable, almost horizontal, perhaps even upward-directed, separated shear layer downstream of the crest as well as an increased mean turbulence intensity above the dividing streamline, consistent with Figure 13. The observed deficits are induced by the inability to resolve the thin shear flow in the accelerated regime accurately. Increasing the resolution reduces the thickness of the predicted shear layer at the crest and changes the direction of the streamlines, as additionally outlined in Figure 18. When approaching the crest, the coarse grid streamlines do not follow the curved hill shape like the fine grid streamlines, and an upward motion is seen for $N_H = 56$ around $x/H = 1$, which reduces the turbulence producing mean flow gradients and cannot be observed for the coarse grid $N_H = 14$. Moreover, coarse grid streamlines indicate a stronger thickening of the top boundary layer until $x/H \approx 7$, which is compensated during the acceleration section. The flow is more inclined toward the top on the coarse grid. Albeit the fine grid snapshot (E) reveals more details of the turbulent structures than the medium grid results (C), the mean turbulence intensities agree rather well. Mind that the evaluation point used for the spectra in Figure 16 is located in the core flow (P-2) regime, where no substantial resolution-based differences occur for the large structure.

4.4 | Regularization parameter analysis (Re = 2800)

This section addresses the impact of the value assigned to the regularization parameter λ under diffusive scaling. Reported results are confined to Re = 2800 and the baseline Mach number of Ma = 1/30.

Averaged data

Figure 19 depicts the nondimensional wall distance y_{T}^+ along the top wall of the domain. The plot involves information for three λ-values and three spatial resolutions, $N_H = \{14; 28; 56\}$ displayed in red, blue, and green. The first fluid node does not exceed the buffer layer for all simulations with $y_{\text{T}}^+ < 7.5$ and $y_{\text{B}}^+ < 12$. Next to the default value of $\lambda_{\text{def}} = 10^{-2}$ (dashed), two supplementary values which differ by four orders of magnitude from the default value are used, $\lambda = 10^{-6}$ (solid) and $\lambda = 10^{2}$ (dotted). Bearing in mind the information on the general level of unregularized ω_i-values mentioned at the end of Section 2.2, the investigated λ-values refer to the AO cumulant model ($\lambda = 10^{-6}$), as well as modifications in the order of 100% (λ_{def}) and 1% ($\lambda = 10^{2}$) of the unregularized ω_i-value, respectively.

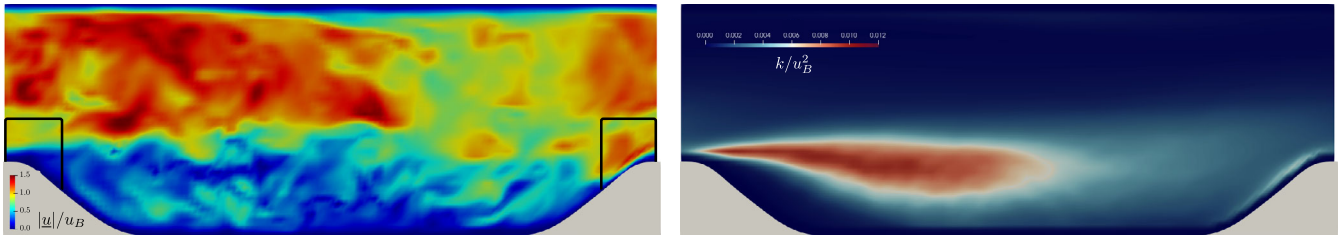

(A) $N_H = 14$ (B) $N_H = 14$

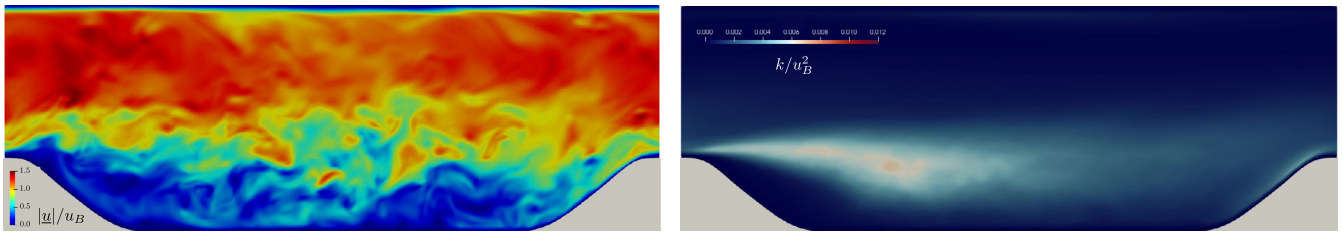

(C) $N_H = 28$ (D) $N_H = 28$

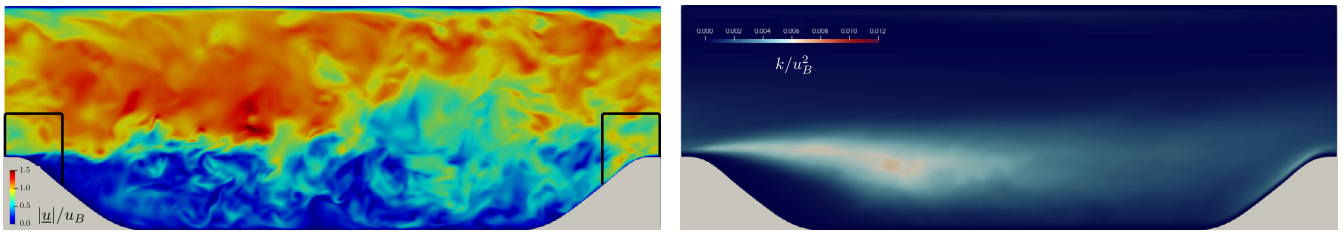

(E) $N_H = 56$ (F) $N_H = 56$

FIGURE 17 Normalized instantaneous velocity magnitude $|\underline{u}|/u_B$ (left) and normalized turbulent kinetic energy k/u_B^2 (right) in the centered x-y plane under diffusive scaling with $N_H = \{14; 28; 56\}$ for the parameter set Re = 2800, Ma = 1/30, and $\lambda_{\text{def}} = 10^{-2}$ [Colour figure can be viewed at wileyonlinelibrary.com]

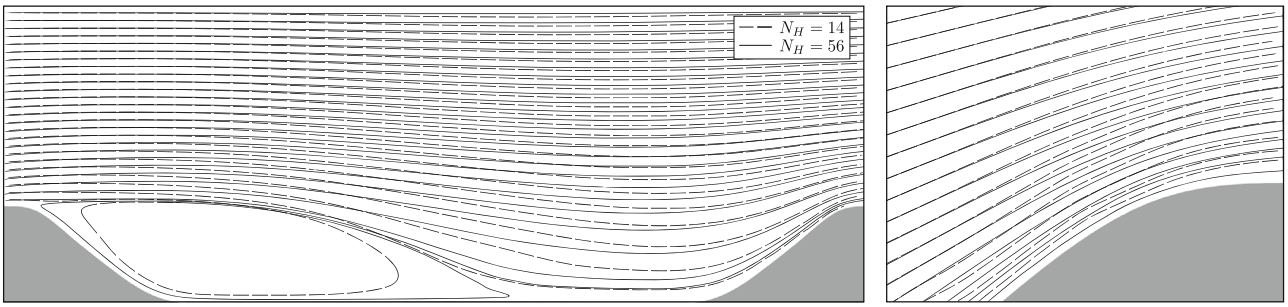

FIGURE 18 Comparison of averaged flow field streamlines obtained with the coarse (red, $N_H = 14$) and the fine grid (green, $N_H = 56$) in the centered x-y plane for the parameter set Re = 2800, Ma = 1/30, and $\lambda_{\text{def}} = 10^{-2}$

As indicated by Figure 19, the regularization influence increases distinctly in under-resolved conditions. Decreasing the limiter value introduces numerical diffusion and reduces the dynamics as well as the wall shear stress. Along the top wall, the y_{T}^+-variation amounts up to approximately 60% for the coarse grid and 30% for the medium grid in response to the limiter's variation. On the contrary, the variations returned by the fine grid computation remain fairly moderate and fall below 10% over the entire domain.

Figure 20 shows the relative L_2 error norm of longitudinal (A) and vertical (B) mean velocity components as a function of the resolution. For brevity, the plots are limited to the integral values of all profiles. Results are again compiled for $\lambda = \{10^{-6}; 10^{-2}; 10^{2}\}$. Overall, the default value $\lambda_{\text{def}} = 10^{-2}$ (orange) yields the smallest errors for the observed quantities over the investigated range of spatial resolutions. Using $\lambda = 10^{-6}$ (dark red), provides

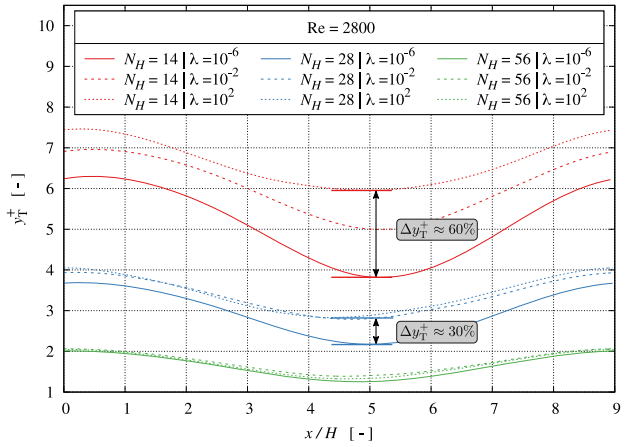

FIGURE 19 Influence of limiter the value $\lambda = \{10^{-6}; 10^{-2}; 10^{2}\}$ on the nondimensional wall distance y_T^+ at the top wall for Re = 2800 and Ma = 1/30 under diffusive scaling with $N_H = \{14; 28; 56\}$ [Colour figure can be viewed at wileyonlinelibrary.com]

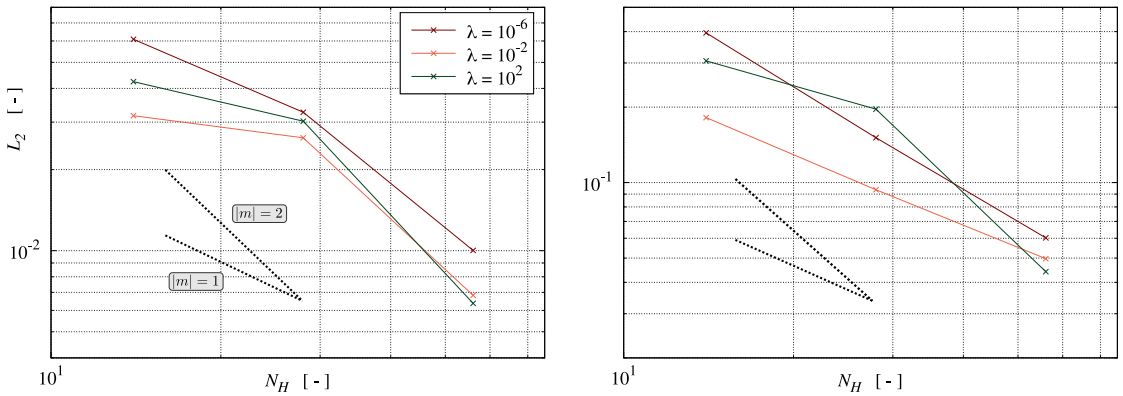

FIGURE 20 Influence of the limiter value $\lambda = \{10^{-6}; 10^{-2}; 10^{2}\}$ on the integral L_2 error norm (WP vs. DNS-*MGLET*) for Re = 2800 and Ma = 1/30 under diffusive scaling with $N_H = \{14; 28; 56\}$ [Colour figure can be viewed at wileyonlinelibrary.com]

a constant slope of $|m| \approx 1.4$ for both quantities. Increasing the limiter value reveals a different behavior. For $\lambda = 10^2$ (green), all error norms feature a pronounced slope change. In the fine grid regime, the convergence primarily improves toward $|m| \approx 2$, while a lower inclination ($|m| \leq 1$) is seen for the coarse grid regime. The observed resolution reduction influences the convergence behavior for the coarser grids, which suggests that the regularization of ω_i in the investigated regime is insufficient. We therefore supplement results obtained from a narrower range of regularization parameter values featuring $\lambda = \{10^{-2}; 10^{-1}; 10^{0}\}$ in Figure 21. The figure reveals that $\lambda = 10^{-1}$ seems a reasonable choice. This finding is also confirmed by the below-discussed assessment of spectra for different λ-values.

Turbulent structures

The influence of the limiter on the characteristics of the resolved Reynolds stress tensor is outlined by Figure 22. The figure depicts the AIM for the three investigated spatial resolutions using the broader limiter spectrum assessed in Figure 20. The reported results refer to a profile extracted at $x/H = 6$, located close to the reattachment point along the bottom wall. Similar results were observed for the other locations. Again, the most pronounced response to a choice of the limiter

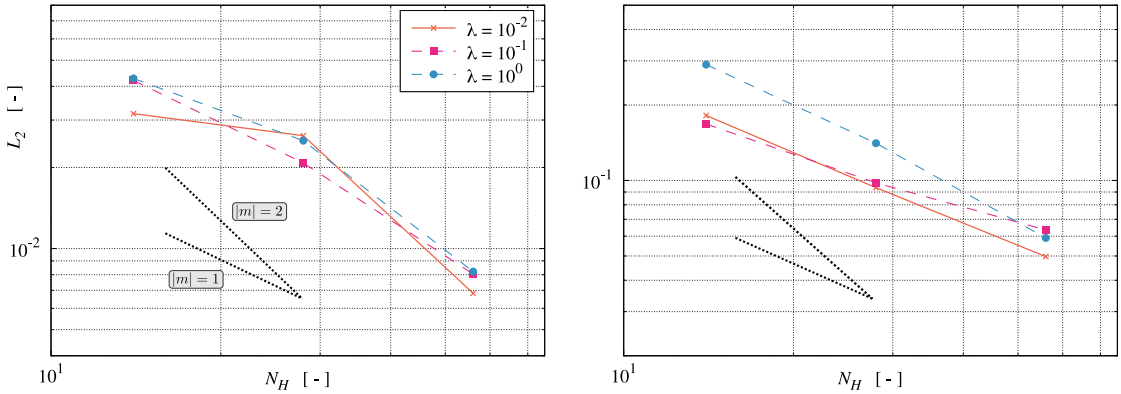

(A) Longitudinal velocity $\overline{u}/u_B$ (B) Vertical velocity $\overline{v}/u_B$

FIGURE 21 Influence of the limiter value $\lambda = \{10^{-2}; 10^{-1}; 10^{0}\}$ on the integral L_2 error norm (WP vs. DNS-*MGLET*) for Re = 2800 and Ma = 1/30 under diffusive scaling with $N_H = \{14; 28; 56\}$ [Colour figure can be viewed at wileyonlinelibrary.com]

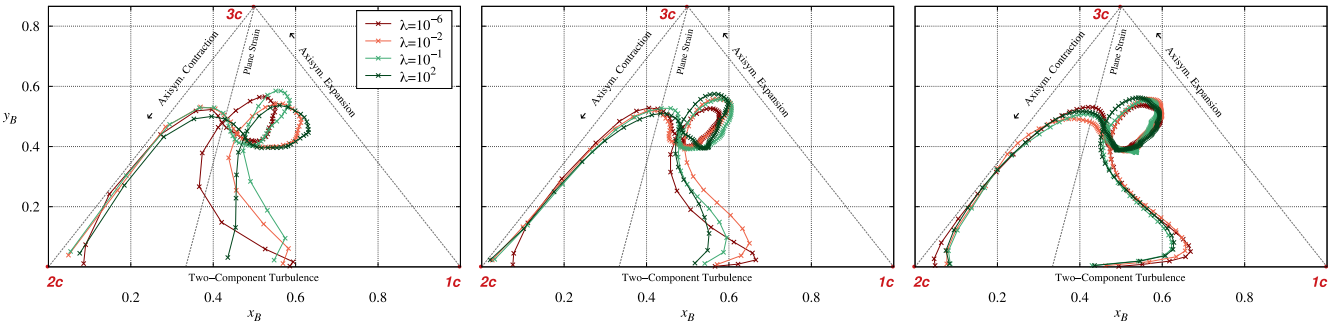

(A) $N_H = 14$ (B) $N_H = 28$ (C) $N_H = 56$

FIGURE 22 Influence of the limiter value $\lambda = \{10^{-6}; 10^{-2}; 10^{2}\}$ on the Reynolds stress anisotropies at $x/H = 6$ for Re = 2800 and Ma = 1/30 under diffusive scaling with $N_H = \{14; 28; 56\}$ [Colour figure can be viewed at wileyonlinelibrary.com]

value occurs for the coarse resolution ($N_H = 14$), whereas the trajectories for the different limiter values converge for the fine grid ($N_H = 56$). The figure reveals that λ distinctly alters the turbulence characteristics of the top wall boundary layer. Here, significant deviations occur along the $\overline{2c - 1c}$ abscissa and propagate into the core flow when the resolution is reduced. For the coarser meshes, results obtained for $\lambda = 10^{-1}$ (light green) provide, perhaps, the best overall agreement with the fine mesh data.

Figure 23 depicts representative energy spectra $PSD(f)$ of the vertical (v) velocity component in the core flow regime (P-2). Each subfigure refers to a fixed resolution N_H and displays data obtained for $\lambda = \{10^{-6}; 10^{-2}; 10^{-1}; 10^{2}\}$. The abscissa is limited to $10^{-1} \leq f \leq 10^{2}$ to support the discussion of details. While an increase of the resolution generally yields a more gradual sloping toward the dissipative scales, many details are identical for all three resolutions. The low frequency ($f \leq 1$) production regime is deemed independent of both the resolution and the limiter value, and all curves approximately originate from $PSD(f = 10^{-1}) \approx 10^{-2}$. When the normalized frequencies approach unity, the graphs enter the inertia regime, where the slope is close to the expected value of $-5/3$, irrespective of the resolution and the limiter value. As alluded to earlier, a grid refinement results in an extension of the inertial range. However, the extent of the inertia regime is also linked to the choice of the limiter value, which distinctly occurs for the coarse grid (A). In particular, low λ-values attenuate the dynamics and significantly reduce the width of the inertial subrange. On the other hand, increasing λ above the default value might help extend the inertial subrange. Considering the fine grid results (C), the variation of the spectrum in response to the λ-value diminishes, and only the AO approach ($\lambda = 10^{-6}$, (dark red)) deviates from the other three curves.

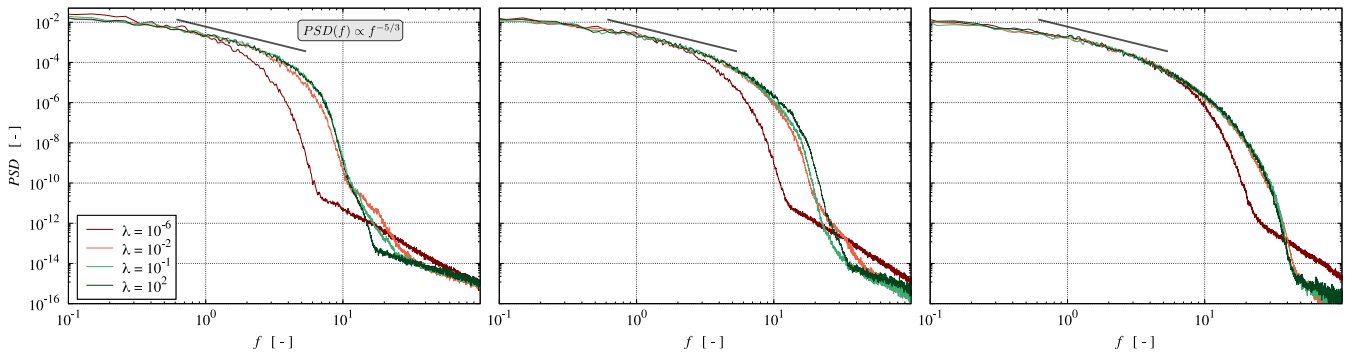

(A) $N_H = 14$ (B) $N_H = 28$ (C) $N_H = 56$

FIGURE 23 Influence of the limiter value $\lambda = \{10^{-6}; 10^{-2}; 10^{-1}; 10^{2}\}$ on the turbulent energy spectra $PSD(f)$ of the vertical (v) component at P-2 (core flow regime) for Re = 2800 and Ma = 1/30 under diffusive scaling with $N_H = \{14; 28; 56\}$ [Colour figure can be viewed at wileyonlinelibrary.com]

4.5 | Reynolds number study

This section addresses a Reynolds number variation and analysis of the prospects of adjusting the value of the regularization parameter λ.

Re = 700

For the lowest considered Reynolds number of Re = 700 the resolution of the near-wall flow is displayed in Figure 24. The maximum $y^+_{\mathrm{B,max}}$ values of the three grids span 5 ($N_H = 14$), 3 ($N_H = 28$), and 2 ($N_H = 56$) wall units. The figure suggests that the fine grid (green) fully resolves the Kolmogorov scales except for a small interval within the accelerated flow region, $8.25 \leq x/H \leq 8.75$. The $y^+_{\mathrm{T|B}}$ evolution confirms the results of the baseline study for Re = 2800, compare Figure 7, and approximately scales with the Reynolds number ratio. Minor deviations thereof are attributed to λ-influences, which take effect in under-resolved conditions. Grid convergence toward the referenced reattachment point[34] at $x/H = 5.34$ (gray vertical) is noted from Figure 24.

The averaged profiles of the longitudinal velocity and Reynolds shear stress are depicted in Figure 25. They display an excellent agreement between the medium (blue) and fine (green) grid results and also reproduce the DNS reference data obtained from *LESOCC*[24,25] (black). Only the coarse grid (red) produces substantial deviations in all four plots. Most apparent defects occur in the vicinity of the crest due to a misrepresentation of the accelerated shear upstream of the crest. As the flow recovers from separation, results of all three resolutions almost coincide at $x/H = 6$ (B).

Based on this evaluation, $N_H = 28$ (blue) is deemed to provide an adequate spatial resolution for Re = 700 as the finer grid does not alter the solution. This conclusion is supported by the energy spectra extracted at the core flow position (P-2) depicted in Figure 26. While the spectra returned by the medium (blue) and the fine (green) grid are almost identical, the coarse grid spectrum (red) shows a smaller equilibrium range and a slightly smaller extent of the inertial subrange. This is similar to the characteristics observed for Re = 2800 in Figure 16. Figure 27 displays the response of the energy spectra of the v-velocity at P-2 to a variation of λ for the three grids. For a fixed spatial resolution (N_H), the spectra are deemed to be practically converged for $\lambda = 10^{-1}$, $\lambda = 10^{-3}$, and $\lambda = 10^{-4}$ on the coarse, medium and fine grid, respectively. The limit λ-value gradually decreases as the grid is refined, nonetheless $\lambda = 10^{-1}$ appears as an adequate and almost resolution-independent choice for this fairly low Reynolds number.

Re = 10,600

Re = 10,600 studies are of interest due to the availability of both experimental[27] and numerical[25,26] (LES) data sourced from the ERCOFTAC data base.[24] The predicted nondimensional wall distances along the bottom, and top walls are not

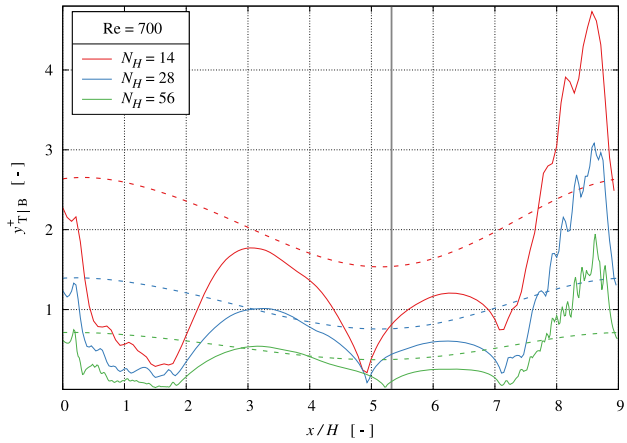

FIGURE 24 Nondimensional wall distance $y^+_{T|B}$ under diffusive scaling with $N_H = \{14; 28; 56\}$ at the bottom (solid) and top (dashed) wall for the parameter set Re = 700, Ma = 1/30, and $\lambda_{def} = 10^{-2}$ [Colour figure can be viewed at wileyonlinelibrary.com]

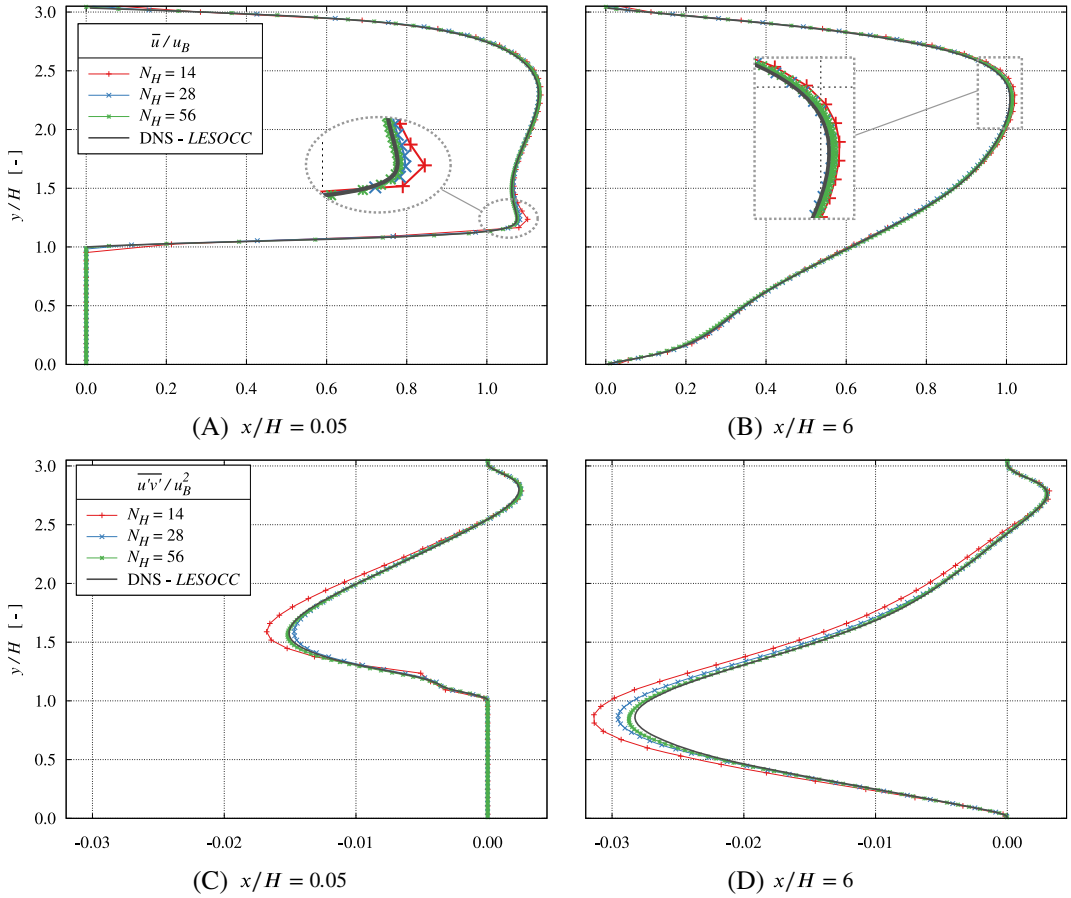

FIGURE 25 WP versus DNS-*LESOCC* reference: averaged longitudinal velocity component $\overline{u}/u_B$ (top) and Reynolds shear stress $\overline{u'v'}/u_B^2$ (bottom) at two distinctive x/H positions under diffusive scaling with $N_H = \{14; 28; 56\}$ for the parameter set Re = 700, Ma = 1/30, and $\lambda_{def} = 10^{-2}$ [Colour figure can be viewed at wileyonlinelibrary.com]

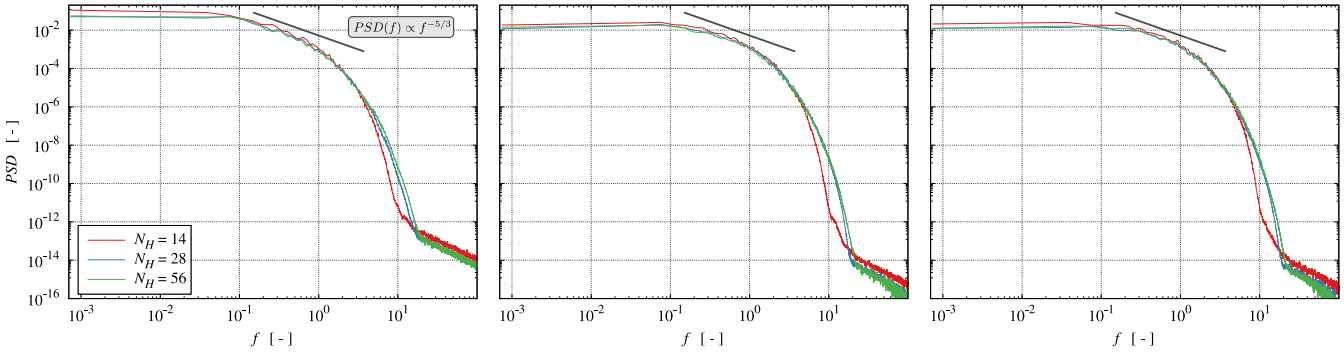

(A) u (longitudinal) (B) v (vertical) (C) w (lateral)

FIGURE 26 Turbulent energy spectra $PSD(f)$ under diffusive scaling with $N_H = \{14; 28; 56\}$ exemplarily depicted at P-2 (core flow) for the parameter set Re = 700, Ma = 1/30, and $\lambda_{\text{def}} = 10^{-2}$ [Colour figure can be viewed at wileyonlinelibrary.com]

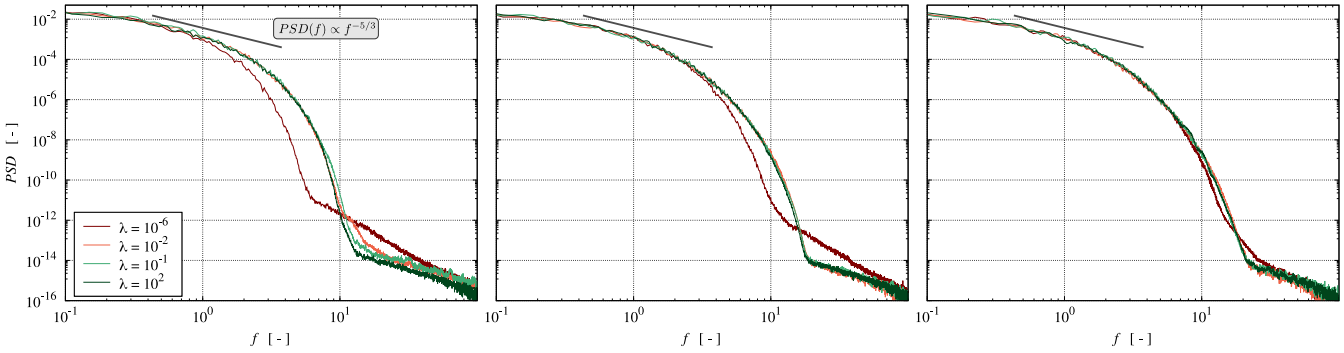

(A) $N_H = 14$ (B) $N_H = 28$ (C) $N_H = 56$

FIGURE 27 Influence of the limiter value $\lambda = \{10^{-6}; 10^{-2}; 10^{-1}; 10^{2}\}$ on the turbulent energy spectra $PSD(f)$ of the vertical (v) component at P-2 (core flow) for Re = 700 and Ma = 1/30 under diffusive scaling with $N_H = \{14; 28; 56\}$ [Colour figure can be viewed at wileyonlinelibrary.com]

displayed to safe space. For $\lambda_{\text{def}} = 10^{-2}$, they resemble the results for Re = 2800 displayed in Figure 7, but y^+-levels are of course higher. The global maxima of $y^+_{\text{B,max}}$ for the three grids occur slightly upstream of the crest along the lower wall and refer to 18 ($N_H = 14$), 14 ($N_H = 28$) and 10 ($N_H = 56$) wall units. Peak values along the top wall are subjected to smaller variations and read $y^+_{\text{T,av}} \approx \{15, 8, 5\}$ on average. Using an exemplary log-law correlation,[58] $u^+(y^+) = 8.3\,(y^+)^{1/7}$, reveals an underprediction of y^+ of approximately 15% for the coarse grid when using a linear relation $u^+ \sim y^+$, while the medium and fine grid predictions seem realistic. The grid resolution is deemed to be in the range of LES for $N_H = 56$ and VLES for $N_H = \{14; 28\}$.

Figure 28 depicts selected averaged flow quantities, $\overline{u}$, $\overline{v}$, and $\overline{u'v'}$, at two upstream ($x/H = \{0.05, 1\}$) and two downstream positions ($x/H = \{7, 8\}$) of the crest. The fine grid appears adequate and provides a fair resolution of the separating flow, the initial separation, the recovery, and the accelerating flow regime. Mean flow predictions are slightly closer to the experimental data than the reference LES data, for which displayed Reynolds stresses only include resolved contributions. The most evident differences between the LBM results and the experimental data occur on the top of the hill. They are attributed to misrepresenting the accelerated upstream flow, which would benefit from finer grids. The predictive accuracy for the Reynolds stress is also fair, particularly in the downstream region. A peculiar feature is the sign difference of $\overline{u'v'}$ predicted around $y/H = 1.2$ for the separating flow at $x/H = 0.05$ (I). This is attributed to curvature effects and an erroneous upward-directed mean flow near the bottom wall shortly behind the inlet, compare Figure 29.

When attention is directed to the medium grid (blue), detrimental effects of the resolution occur between the hills. The strong acceleration of the flow at $x/H = 8$ and the related pronounced, thin shear layer is not as well captured as for $N_H = 56$. The global flow is noticeably displaced toward the top wall, and the recovery at $x/H = 7$ is likewise weaker.

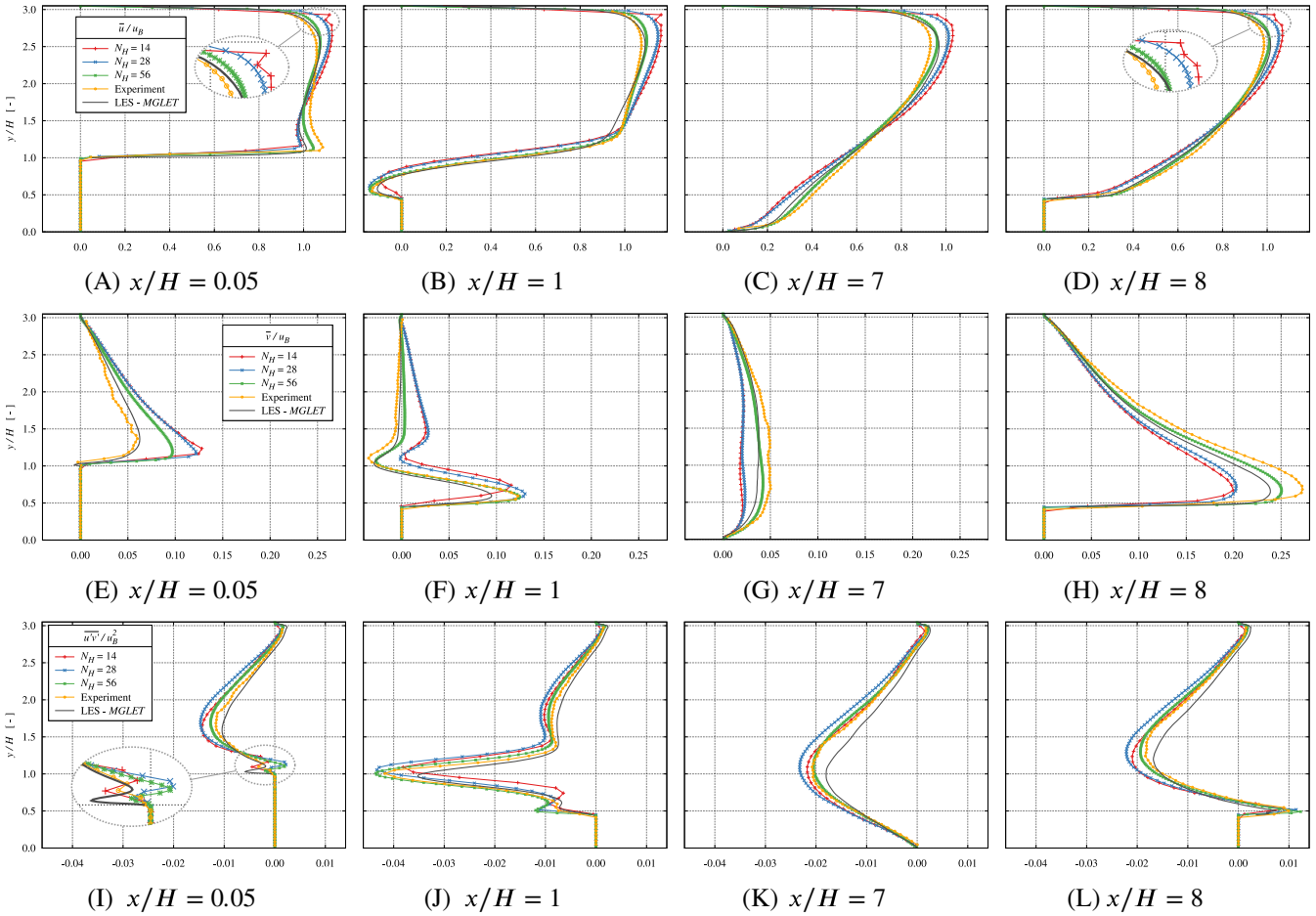

FIGURE 28 WP versus LES-*MGLET* and experimental references: averaged longitudinal $\overline{u}/u_B$ (top) and vertical $\overline{v}/u_B$ (middle) velocity component and Reynolds shear stress $\overline{u'v'}/u_B^2$ (bottom) at four distinctive x/H positions under diffusive scaling with $N_H = \{14; 28; 56\}$ for the parameter set Re = 10,600, Ma = 1/30, and $\lambda_{\text{def}} = 10^{-2}$ [Colour figure can be viewed at wileyonlinelibrary.com]

As a result, the bottom boundary layer thickens, the intensity of the wall-normal velocity weakens, and $\overline{u}$-gradients are reduced. These trends continue for the coarse grid (red) results. Due to the inadequate resolution, the displacement of the global flow field toward the top wall becomes more pronounced, and gradients of the bottom longitudinal velocity are further reduced. Neglecting a turbulence model and wall modeling strategies, the prediction of the $\overline{u}$-velocity along the top wall is insufficient. It exceeds the resolution limits, as indicated by the kinks in Figure 28. Mind that discontinuous upper wall $\overline{u}$-profiles are also seen for smaller λ-values on the coarse grid. Such inaccuracies were also observed in previous studies of simple channel flows[18,19] for y^+-values situated in the logarithmic regime.

Introducing an SGS model adjusts ω_1 and helps to avoid discontinuous velocity profiles. Though eddy viscosity models of turbulence are somewhat debatable in the context of LBM,[59] they are often employed in practical simulations. Figure 30 shows the influence of a simple Smagorinsky subgrid-scale eddy viscosity model[60] which alters ω_1 by a modification of (13), $\omega_1 = 1/(\nu_g/c_s^2 + \Delta t/2)$. Here, $\nu_g = \nu + (C_S\Delta)^2 S$ is an effective viscosity, Δ corresponds to the lattice spacing Δx_i, $S = \sqrt{2S_{ij}S_{ij}}$ is a strain-rate measure and $C_S = 0.1$ denotes the Smagorinsky constant. Present SGS simulations do not substantially improve the acceleration prediction but support the predictions along the top wall. Here, the resolution is too coarse without the SGS for $N_H = 14$ along the entire wall, and the use of an SGS yields approximately 20% smaller y^+ values, but much fewer changes along the bottom wall. Increasing the resolution attenuates the SGS influences, which mainly refer to the upper boundary layer, as outlined by Figure 30.

A note of caution is necessary as regards the influence of the SGS on the regularized WP cumulant. According to Equations (14)–(16), the relaxation rates $\omega_{3,4,5}$ depend on ω_1. Hence, two options exist to compute $\omega_{3,4,5}$ in combination with an eddy-viscosity model, one using the SGS-modified ω_1 and one using the unmodified ω_1. Related differences were examined and deemed negligible for the default value λ_{def}. Moreover, present SGS results match the findings of

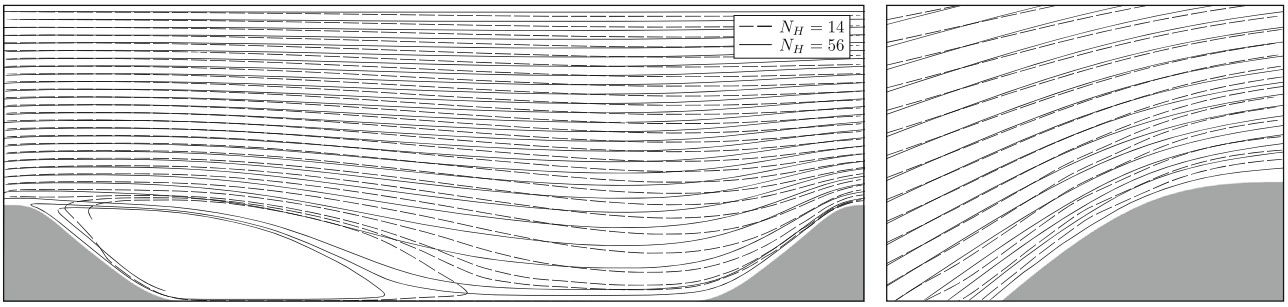

FIGURE 29 Comparison of averaged flow field streamlines obtained with the coarse (red, $N_H = 14$) and the fine grid (green, $N_H = 56$) in the centered x-y plane for the parameter set Re = 10,600, Ma = 1/30, and $\lambda_{\text{def}} = 10^{-2}$

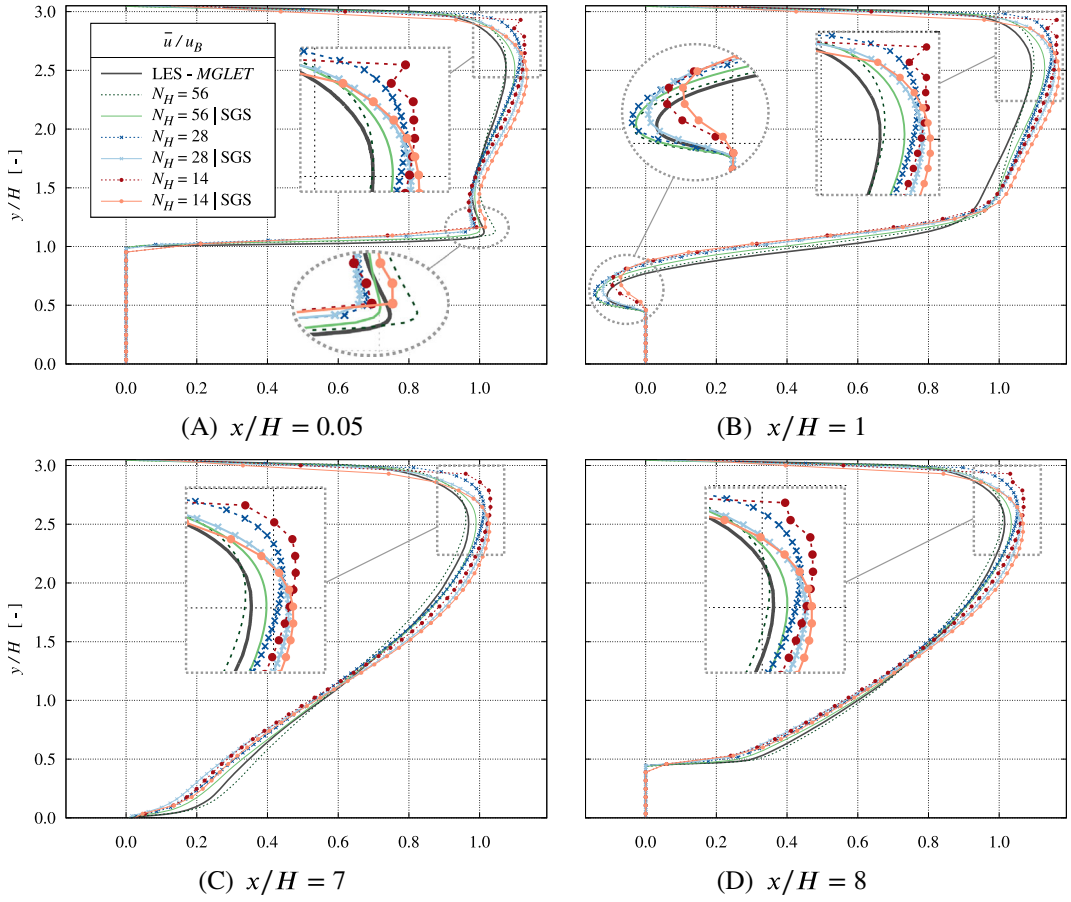

FIGURE 30 WP versus LES-*MGLET* reference: Averaged longitudinal $\overline{u}/u_B$ velocity component at four distinctive x/H positions under diffusive scaling with additional consideration of a SGS model for the parameter set Re = 10,600, Ma = 1/30, and $\lambda_{\text{def}} = 10^{-2}$ [Colour figure can be viewed at wileyonlinelibrary.com]

Chang et al.,[61] who employed an immersed boundary Navier–Stokes procedure with a dynamic Smagorinsky model on an anisotropic Cartesian grid with a resolution close to our medium grid. The authors conclude that predictions without wall modeling return better results and report similar predictive trends as the present study.

In line with the results obtained for the lower Reynolds numbers, the spectra displayed in Figure 31 indicate a substantial widening of the inertial subrange with an increase of the resolution. All spectra show a kink within the dissipation range, which indicates the activity of the regularization and is shifted toward higher frequencies as the resolution increases. For sufficiently large values of λ, the regularization is confined to the dissipative scales at the upper bounds of

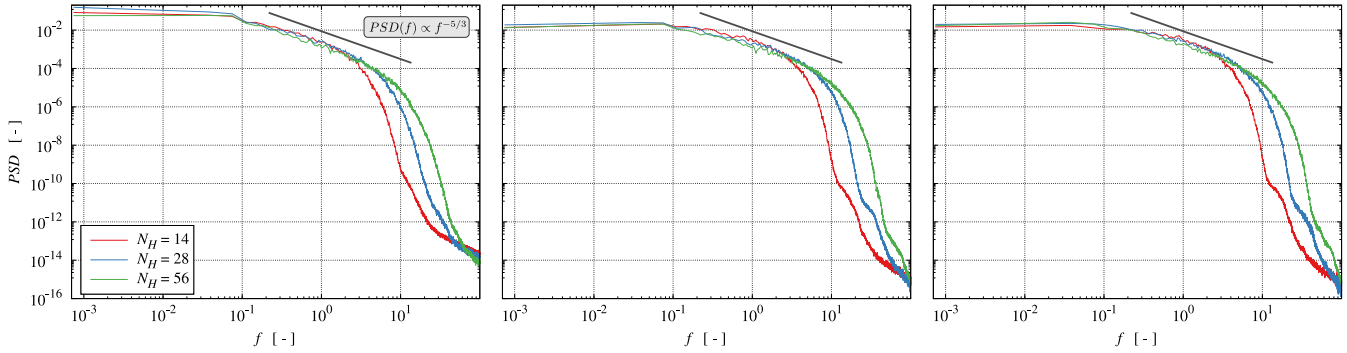

(A) u (longitudinal) (B) v (vertical) (C) w (lateral)

FIGURE 31 Turbulent energy spectra $PSD(f)$ under diffusive scaling with $N_H = \{14; 28; 56\}$ exemplarily depicted at P-2 (core flow regime) for the parameter set Re = 10,600, Ma = 1/30, and $\lambda_{\text{def}} = 10^{-2}$ [Colour figure can be viewed at wileyonlinelibrary.com]

the spectra. When decreasing the value of λ, the regularization influences overlap with the inertia subrange, compare the previous Figure 23. This effect will subsequently be discussed in more detail for the medium ($N_H = 28$) grid, making the related differences more apparent.

Figure 32 outlines the sensitivity of $\overline{u}$ profiles to changes of λ-value at $x/H = \{0.05, 1, 7, 8\}$ on the medium grid. The dashed lines represent the default limiter solution $\lambda_{\text{def}} = 10^{-2}$, where the flow field starts to be globally displaced, and the recovery is delayed. The regularization suppressed flow dynamics are less when increasing the λ-value. The dynamics release significantly improves agreement with both the numerical reference and the fine grid LBM results. On the contrary, a decrease of λ restrains the resolved dynamics and thus promotes the global displacement toward the top wall. The stability limit for this grid is $\lambda^{10,600}_{\text{max},28} = 10^{0}$.

In order to pursue the previous quantitatively, Figure 33 contains plots of the respective L_2 error norm for the entire predicted flow field. Figure 33A reveals a gradually improved agreement of the predicted longitudinal ($\overline{u}/u_B$) velocities for $\lambda > 10^{-2}$, whereby the mean integral error (red) is reduced by a factor of 4 between $\lambda = 10^{-2}$ and $\lambda = 10^{0}$. The sensitivity decreases for $\lambda > 1.5 \cdot 10^{-1}$ and $L_2 \approx 2 \cdot 10^{-2}$ appears as the converged value before reaching the stability limit. The graph features two additional horizontal lines representing the integral L_2 norm of the coarse (orange) and the fine (green) grid for the default λ-value. A similar trend is observed for the vertical ($\overline{v}/u_B$) velocity component depicted in (B). Hence, the predictive accuracy is substantially governed by the interplay between the λ-value and the resolution, provided that the resolution is not too coarse. Present results indicate a required lattice distance based (local) Reynolds number of $\text{Re}/N_H \leq 750$ or near-wall resolutions around $y^+ \approx 15$.

The resolution-regularization interplay is somewhat critical, as outlined by Figure 34A, which displays the energy spectra of the lateral velocity (w) component in an accelerated flow location (P-4) for a variation of λ on the coarse grid ($N_H = 14$). The nonphysical increase of energy in the high-frequency regime for $\lambda = 10^{0}$, which refers to the optimal value on the medium mesh, clearly indicates the limits of an adjustment. Similar to the findings for Re = 2800, the optimal λ-value increases with the resolution and reads $\lambda^{10,600}_{\text{opt},56} = 10^{-1}$ and $\lambda^{10,600}_{\text{opt},14} = 5 \times 10^{-1}$ for the fine and the coarse grid.

Figure 35 depicts two longitudinal (u) energy spectra in response to the variation of the value of the regularization parameter $\lambda = \{10^{-6}; 10^{0}\}$ and the resolution $N_H = \{28; 56\}$ at a core (P-2; left) and accelerated (P-4; right) flow location. While the slopes of the inertial and dissipation range depend only marginally on λ and N_H, both parameters influence the width of the inertial range. For a fixed resolution, the λ-dependent widening is more pronounced for the coarser grid as indicated by the blue arrows ($\lambda \uparrow$) connecting the green ($N_H = 28$) and red ($N_H = 56$) colored verticals. In conjunction with fixed λ-values, the impact of grid refinement ($N_H \uparrow$) is larger (red arrows) for $\lambda = 10^{-6}$ which verifies the strict dependence on N_H identified in the scope of the baseline analysis for the lowest employed limiter value, compare L_2 error norm plots of Figure 20 (dark red). For $\lambda = 10^{0}$ the extent of the inertial subrange changes only marginally when increasing the resolution from $N_H = 28$ (dark green) to $N_H = 56$ (dark red). Nevertheless, the spatial resolution strongly affects the dissipation regime and the width of the equilibrium range. This dependence is also characterized by the enrichment with higher-frequency contributions and shifting the f-kink position within the dissipation range.

Figure 36 compares the velocity magnitude ($|\underline{u}|/u_B$) and the (resolved) Reynolds-averaged turbulent kinetic energy (k/u_B^2) in the centered x-y plane for the optimal and the lowest value of λ on the medium grid with $N_H = 28$. Subtle but

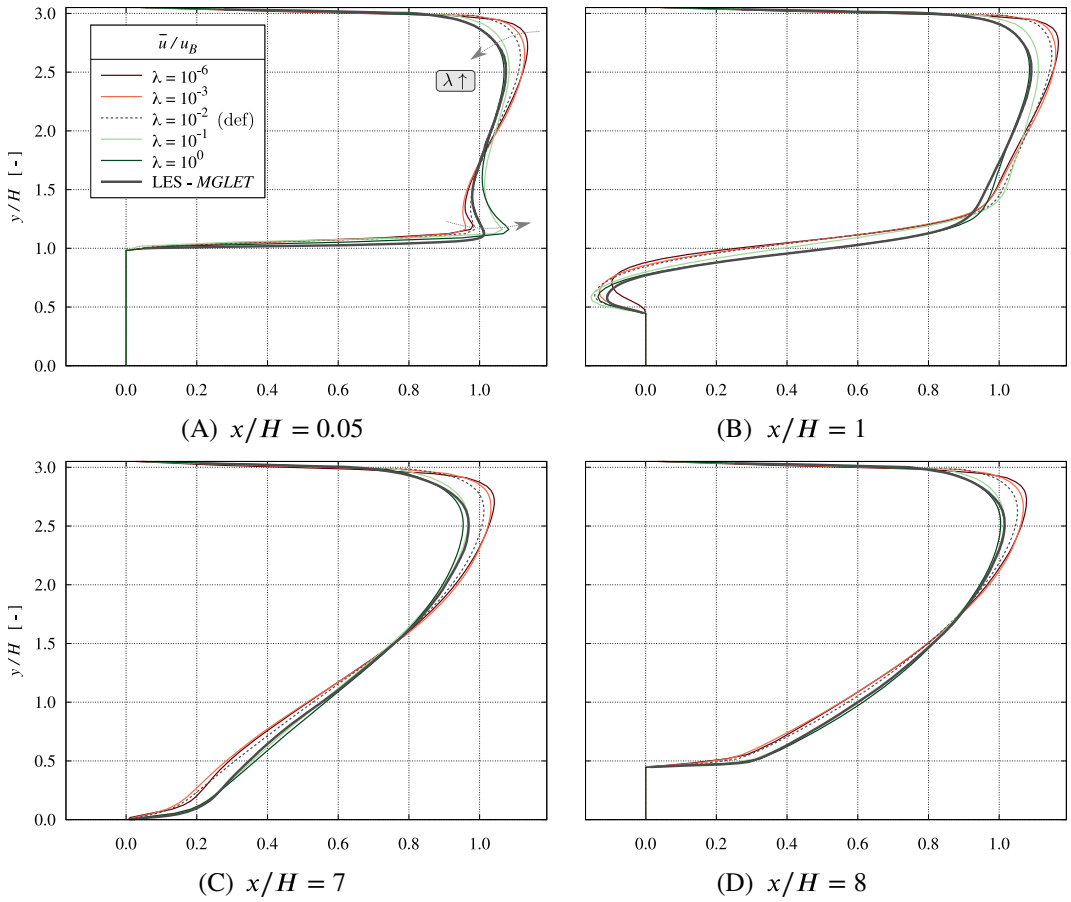

FIGURE 32 WP versus LES-*MGLET* reference: Averaged longitudinal $\overline{u}/u_B$ velocity component predicted with five values of the regularization parameter λ depicted at four x/H locations for Re = 10,600, $N_H = 28$ (medium grid) and Ma = 1/30 [Colour figure can be viewed at wileyonlinelibrary.com]

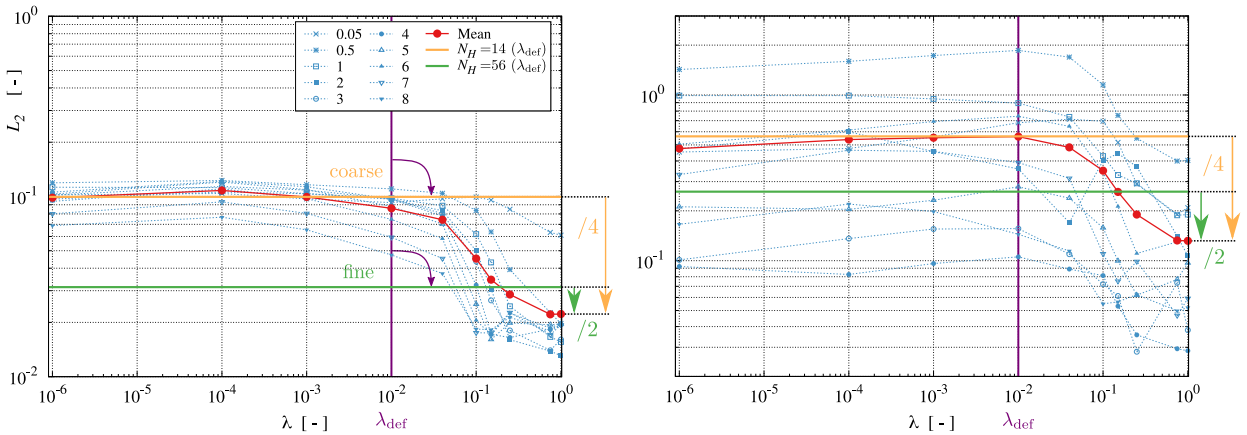

FIGURE 33 Influence of the regularization parameter on the L_2 error norm (WP cumulant LBM vs. LES-*MGLET*) for $\lambda = \{10^{-6}, ..., 10^{0}\}$, Re = 10,600, $N_H = 28$ (medium grid) and Ma = 1/30. The horizontal lines indicate the integral L_2 norm using the default limiter $\lambda_{def} = 10^{-2}$ (purple vertical) for the coarse (orange) resp. fine (green) grid [Colour figure can be viewed at wileyonlinelibrary.com]

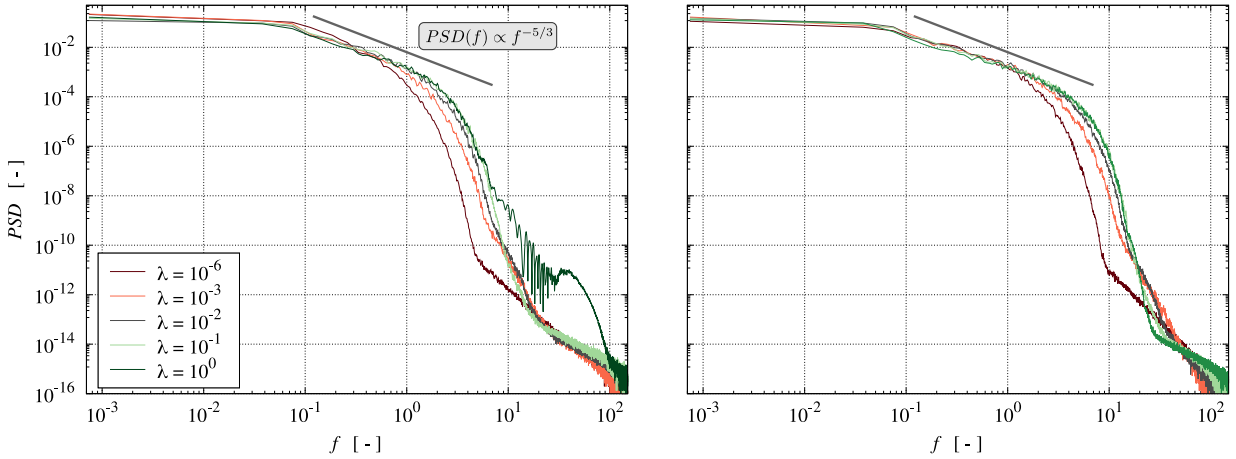

(A) $N_H = 14$ (B) $N_H = 28$

FIGURE 34 Influence of the limiter value λ on the turbulent energy spectra of the lateral (w) component at P-4 (accelerated flow) for Re = 10,600 and Ma = 1/30 on the coarse and medium grid [Colour figure can be viewed at wileyonlinelibrary.com]

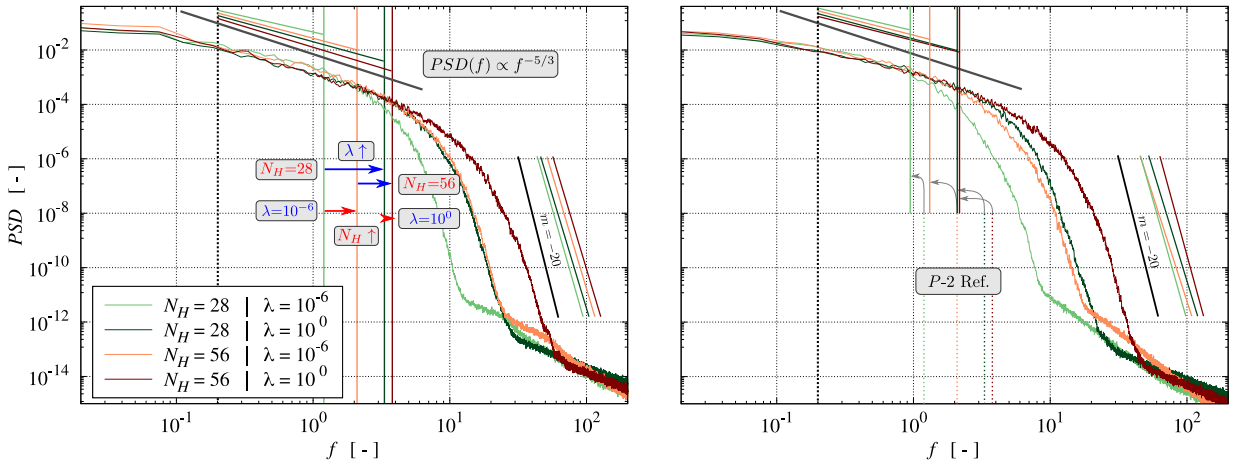

(A) P-2 (core flow) (B) P-4 (accelerated flow)

FIGURE 35 Influence of the limiter value $\lambda = \{10^{-6}; 10^{0}\}$ and spatial resolution $N_H = \{28; 56\}$ on the turbulent energy spectra $PSD(f)$ of the longitudinal (u) component at two locations for Re = 10,600 and Ma = 1/30 [Colour figure can be viewed at wileyonlinelibrary.com]

influential differences are evident for the optimal λ-value associated with the smallest possible regularization, compare white markings in (A) and (B). The structures displayed by λ_{opt} are essentially smaller than for $\lambda = 10^{-6}$, and the mixing of low and high momentum fluid close to the reattachment point at $x/H = 4.7$ is enhanced. Also, the separating shear layer is less upward-directed in the inlet section and remains much thinner in the acceleration regime. The strong shearing causes a more pronounced turbulence intensity in the inlet section with an enhanced early mixing in the upstream zone of the separation. However, far less turbulence intensity arises in the vicinity of the (mean) dividing streamline.

Exchanging the default value $\lambda = 10^{-2}$ by the optimal one $\lambda = 10^{0}$ significantly improves the predictive performance for $N_H = 28$, as outlined in Figure 37. Results of the model-free simulation for $\lambda = 10^{0}$ match reference LES and experimental data surprisingly fair. A substantial change is noticed for the increased λ-value at the $x/H = 0.05$ location. The flow is directed downwards and not upwards, in line with LES reference data, and the Reynolds shear stress is no longer changing sign near the bottom wall. A key advantage of the WP cumulant LBM seems the explicit control through λ without generating further artificial interference, provided that the spatial resolution is reasonably adequate, with $y^{+} \approx 10 - 15$ matching the lower half of the buffer layer region.

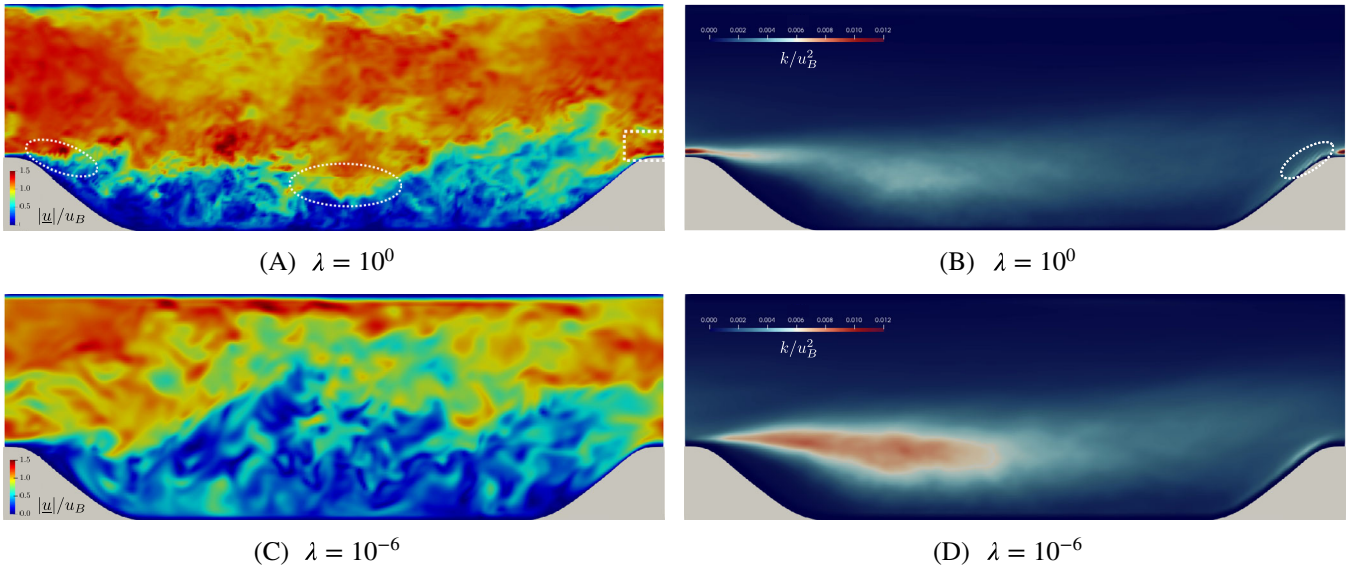

FIGURE 36 Influence of the limiter value $\lambda = \{10^{-6}; 10^0\}$ on the instantaneous velocity magnitude $|\underline{u}|/u_B$ (left) and turbulent kinetic energy k/u_B^2 (right) in the centered x-y plane for Re = 10,600 on the medium grid ($N_H = 28$) and Ma = 1/30 [Colour figure can be viewed at wileyonlinelibrary.com]

Re = 37,000

Figure 38A shows the $y^+_{\mathrm{T|B}}$ pathways for the three grids when the Reynolds number is increased to Re = 37,000. Obviously, only the fine grid is sufficient, and results for the medium and the coarse grid indicate the same resolution induced failures that were already intensively discussed for Re = 10,600 ($N_H = 14$), compare Figure 38B. Brief verifications of the predicted shear stresses using a more realistic wall function, for example $u^+(y^+) = 8.4\,(y^+)^{1/7}$, indicate a substantial underprediction of the shear stress by approximately 100% and 40% for the coarse and the medium mesh. Hence, both meshes are deemed inadequate. Due to the coarser resolution for this Reynolds number and the associated lower stability limit, the deviation of the optimal value $\lambda^{37{,}000}_{\mathrm{opt},56} = 5 \times 10^{-1}$ from the default value is small. Analog to the changes observed for Re = 10,600, an increase of λ from the default value to the optimum value results in substantial improvements. Again, predictions of the recovery, acceleration, and near crest regions improve qualitatively and quantitatively. Figure 39 compares exemplary longitudinal velocity profiles returned by $\lambda_{\mathrm{def}} = 10^{-2}$ as well as the optimal $\lambda^{37{,}000}_{\mathrm{opt},56}$ with reference LES and experimental data. Overall, the present WP cumulant LBM slightly outperforms the reference LES in combination with the optimal λ-value, though the respective grid is about five times larger. Figure 40 motivates the choice of the optimal λ-value from the evolution of the L_2 integral error with λ, which is approximately reduced by a factor of two for the longitudinal velocity and 1.5 for the vertical velocity. The green dashed lines indicate the error level obtained for Re = 10,600 when using the optimal medium grid λ-value, which are close to the fine grid accuracy for Re = 37,000 applying the optimal limiter $\lambda^{37{,}000}_{\mathrm{opt},56}$. Mind that the analysis of the spectral convergence might reveal slightly different optimal values.

4.6 | Synopsis

A comparative analysis of the four Reynolds numbers under diffusive scaling is conducted to condense the results. To this end, Figure 41 depicts the integral L_2 error norms of the longitudinal velocity as a function of the Reynolds (A) and Mach number (B).

For the acoustic scaling summarized in (B), results refer to the default value $\lambda_{\mathrm{def}} = 10^{-2}$ and medium grid results are omitted to improve the clarity. It is evident that the acoustic scaling is not intertwined with either Re or N_H influences. The variation of the error level with Ma is very moderate, with the largest slopes in the range of $m \approx 0.2$.

As regards the diffusive scaling aspects summarized in (A), solid lines depict results obtained with the default λ-value, and dashed lines refer to results obtained with an optimal choice of λ for the two higher Reynolds numbers. A large

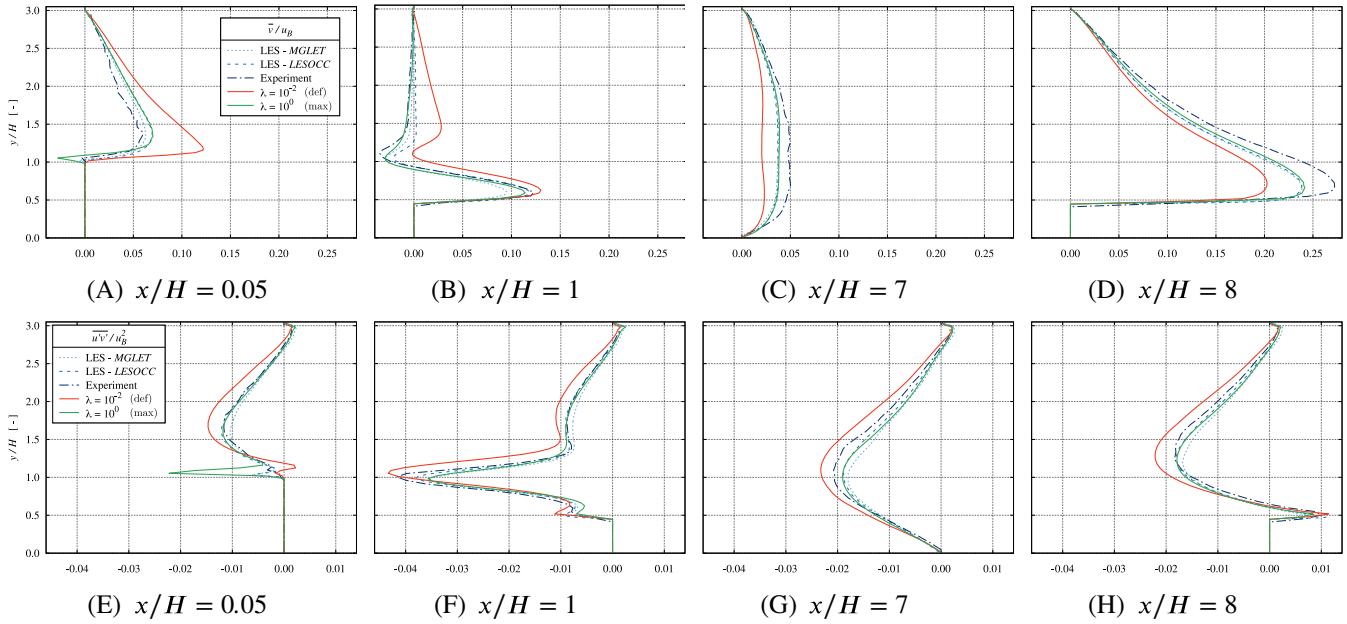

FIGURE 37 WP versus LES-*MGLET* / *LESOCC* and experimental references: Averaged vertical $\bar{v}/u_B$ (top) velocity component and Reynolds shear stress $\overline{u'v'}/u_B^2$ (bottom) predicted with two values (default and maximum) of the regularization parameter λ depicted at four x/H locations for Re = 10,600 on the medium grid ($N_H = 28$) with Ma = 1/30 [Colour figure can be viewed at wileyonlinelibrary.com]

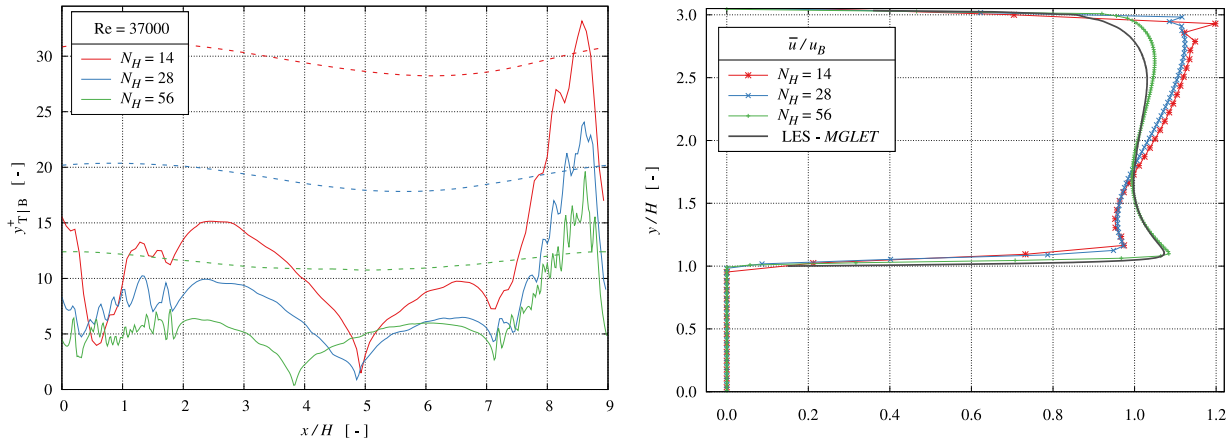

(A) Computed nondimensional wall distance $y^+_{T|B}$ at the bottom [solid] and top [dashed] wall

(B) Averaged longitudinal velocity component $\bar{u}/u_B$ extracted at $x/H = 0.05$

FIGURE 38 Selected diffusive scaling results for Re = 37,000 with Ma = 1/30 and $\lambda_{def} = 10^{-2}$ [Colour figure can be viewed at wileyonlinelibrary.com]

sensitivity to the Reynolds number and thereby the resolution is observed between Re = 2800 and Re = 10,600. Both decreasing (Re = 700) and increasing (Re = 37,000) the Reynolds number reduces the L_2 slope. For the low Reynolds number regime, the resolution seems to reach grid convergence, and the details of the approach, particularly the influence of the regularization, become less vital. For this reason, results for an optimal choice of λ are only given for the larger Reynolds numbers. For the high Reynolds number, the opportunities of adjusting the regularization diminish in line with smaller stability preserving upper limits of λ, and improvements are only detected for the more stable fine grid. Figure 42 complements the diffusive scaling results of Figure 41A by observing the change of predictive agreement over the (local) cell Reynolds number $\mathrm{Re_c} = u_B\,\Delta x/\nu$ for the mean axial velocity and the mean turbulent shear stress. Here, improvements of a change of the regularization parameter become more obvious.

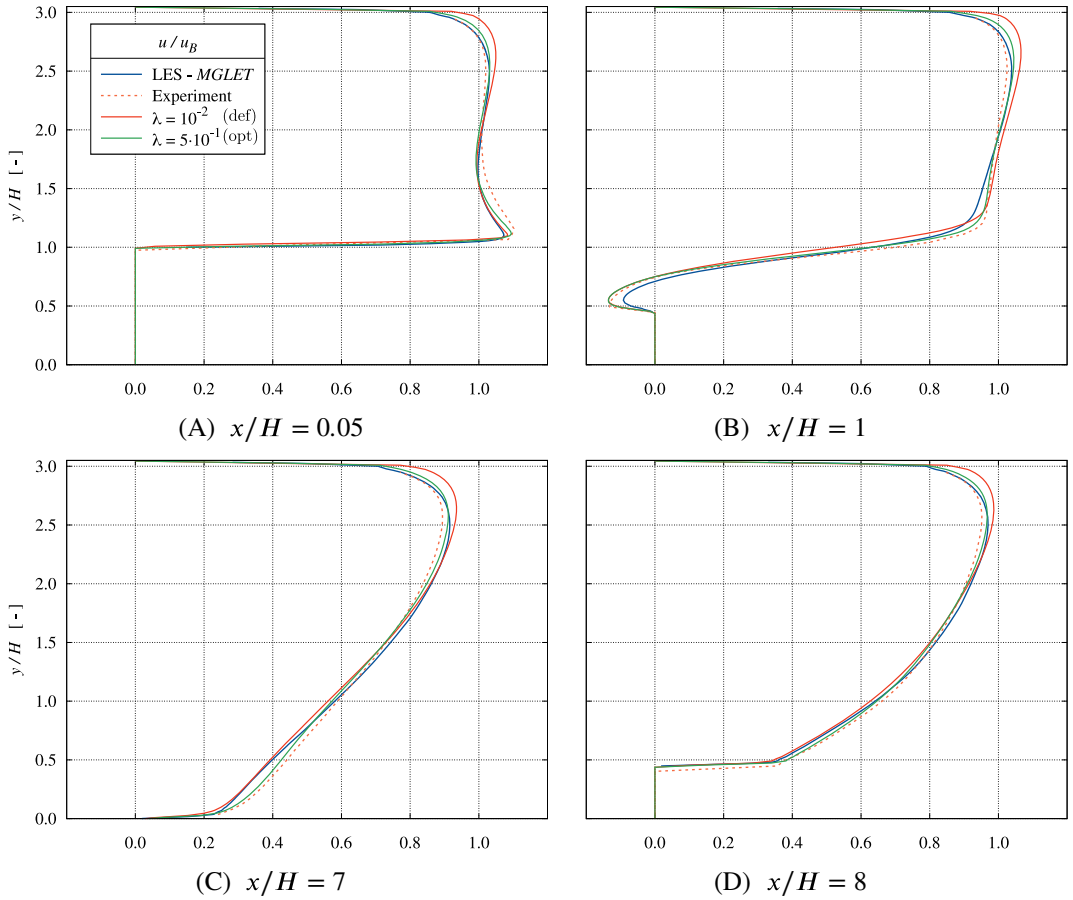

FIGURE 39 WP versus LES-*MGLET* and experimental references: Averaged longitudinal $\overline{u}/u_B$ velocity component predicted with two values (default and optimum) of the regularization parameter λ depicted at four x/H locations for Re = 37,000 on the fine grid ($N_H = 56$) with Ma = 1/30 [Colour figure can be viewed at wileyonlinelibrary.com]

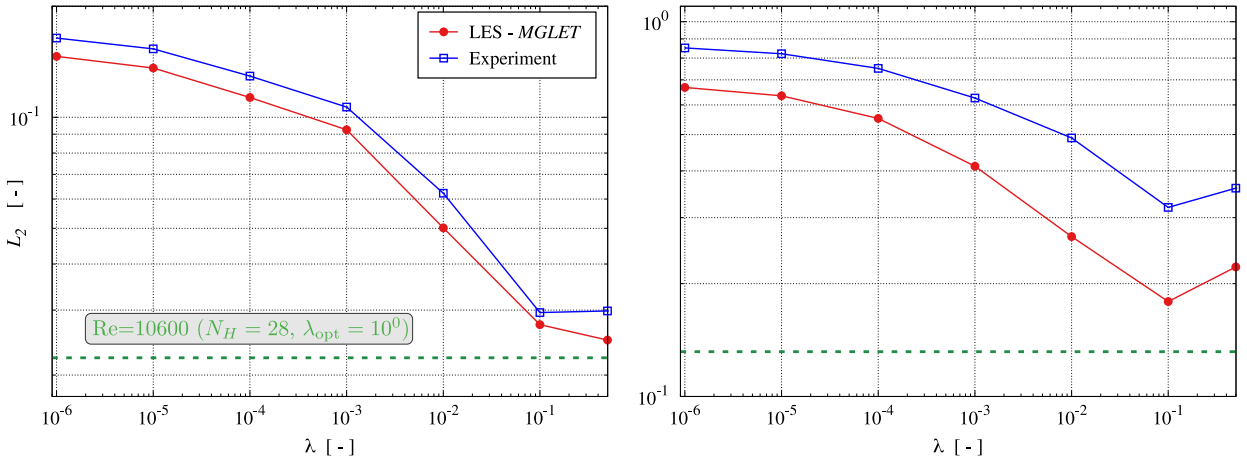

FIGURE 40 Influence of the limiter value $\lambda = \{10^{-6}; \ldots; 5 \cdot 10^{-1}\}$ on the integral L_2 error norm (WP vs. LES-*MGLET* /Experiment) for Re = 37,000, $N_H = 56$ (fine grid) and Ma = 1/30. The dashed green lines indicate the integral L_2 norm using the optimal limiter determined for the medium grid and Re = 10,600, compare Figure 33 [Colour figure can be viewed at wileyonlinelibrary.com]

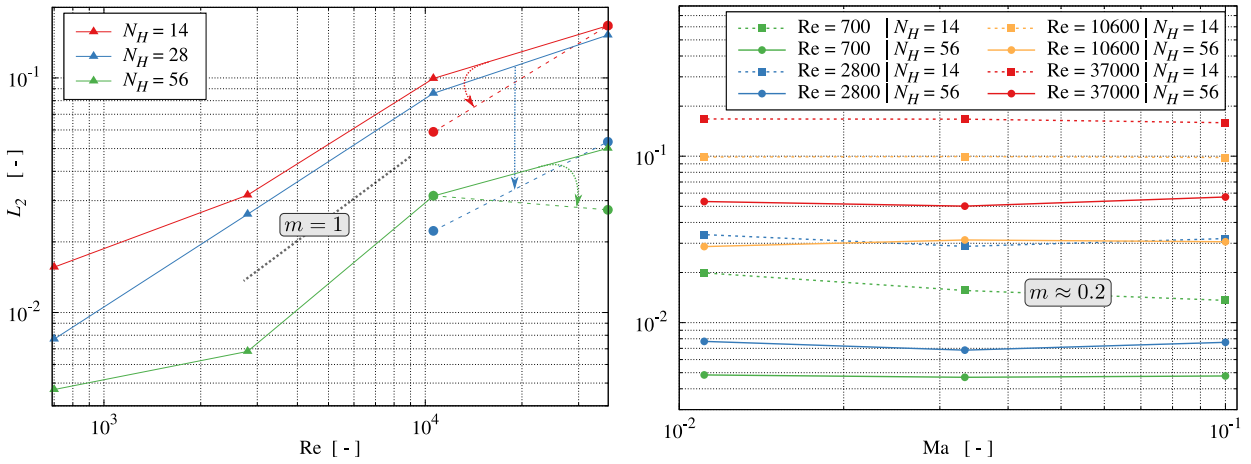

(A) Diffusive scaling for the default [solid] and optimal [dashed for Re = {10,600; 37,000}, cf. Table 7] limiter value.

(B) Acoustic scaling on the coarse [dashed] and fine [solid] grid for $\lambda_{\text{def}} = 10^{-2}$.

FIGURE 41 Integral L_2 error norm (WP vs. *LESOCC / MGLET* references) of the longitudinal velocity component $\overline{u}/u_B$ for varying Reynolds numbers Re = {700; 2800; 10,600; 37,000} under diffusive and acoustic scaling [Colour figure can be viewed at wileyonlinelibrary.com]

TABLE 6 Stability limits $\lambda^{\text{Re}}_{\text{max},N_H}$ for Ma = 1/30

Re	$N_H = 14$	$N_H = 28$	$N_H = 56$
700	10^6	10^6	10^6
2800	10^3	10^6	10^6
10,600	10^0	10^0	10^1
37,000	10^{-1}	5×10^{-1}	5×10^{-1}

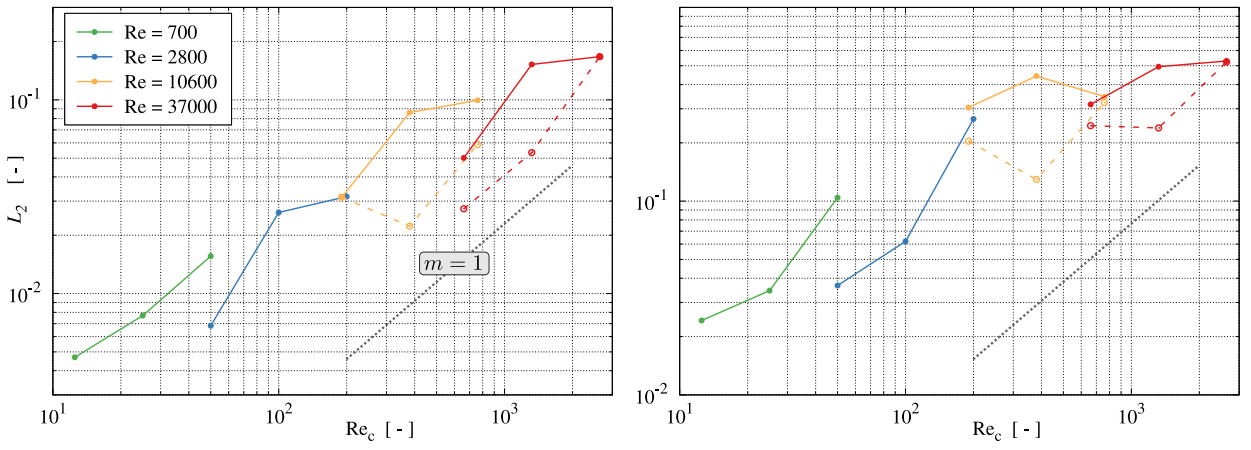

(A) Longitudinal velocity $\overline{u}/u_B$

(B) Reynolds shear stress $\overline{u'v'}/u_B^2$

FIGURE 42 Influence of the cell Reynolds number $\text{Re}_c = \text{Re}/N_H = \{12.5; \ldots; 2640\}$ on the integral L_2 error norm for the default (solid) and optimal (dashed) limiter values for two selected flow quantities. Due to the discontinuous overlap of $\text{Re}_c(\text{Re}, N_H)$ for the investigated test case matrix, compare Table 7, lines are additionally colored by the underlying Reynolds numbers [Colour figure can be viewed at wileyonlinelibrary.com]

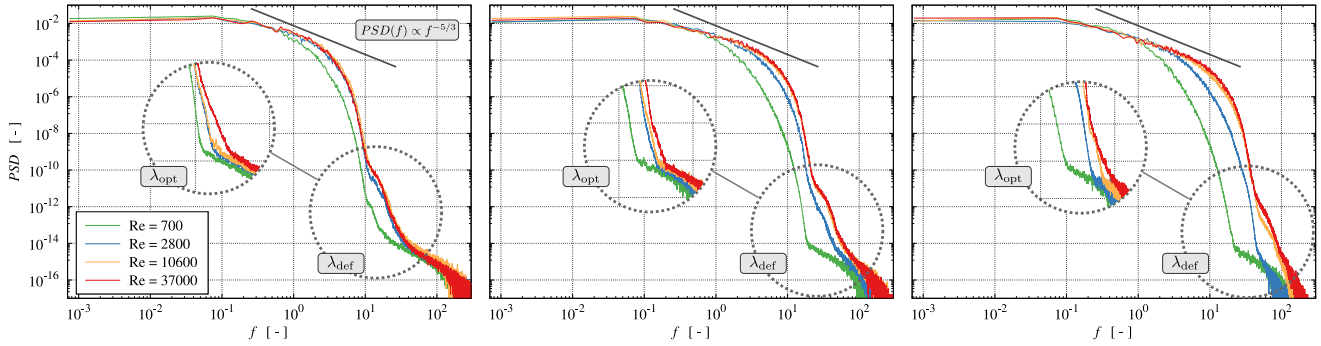

(A) $N_H = 14$ (B) $N_H = 28$ (C) $N_H = 56$

FIGURE 43 Turbulent energy spectra $PSD(f)$ in vertical (v) direction for Re = {700; 2800; 10,600; 37,000} on each grid at P-2 (core flow regime) for Ma = 1/30 using the default limiter value $\lambda_{\text{def}} = 10^{-2}$. The circled areas display the change of the dissipation range when applying the optimal limiter value λ_{opt} in each case [Colour figure can be viewed at wileyonlinelibrary.com]

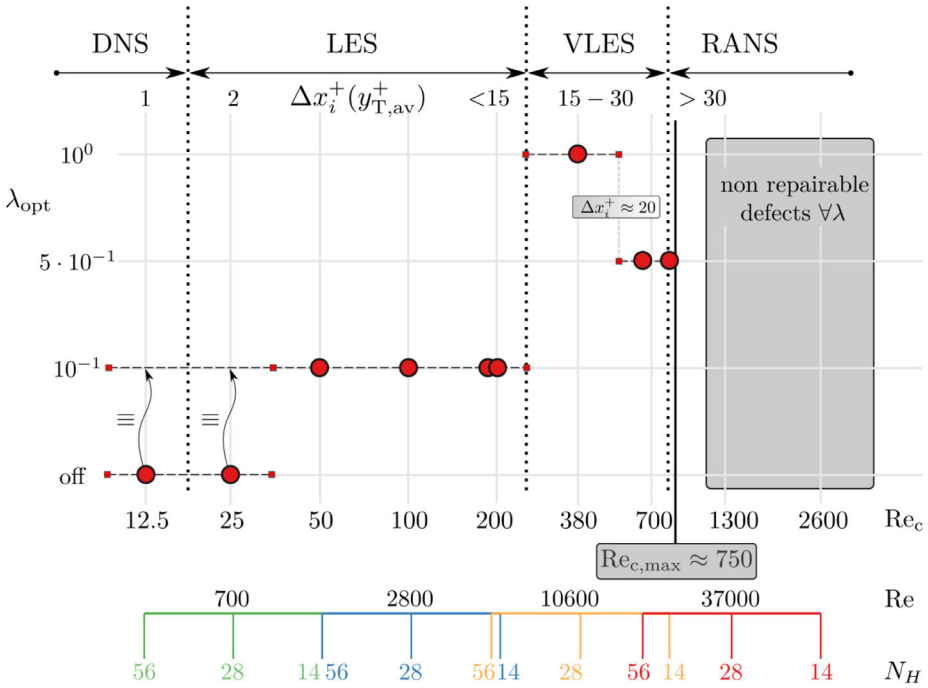

FIGURE 44 Optimal limiter dependency λ_{opt} for varying grid types ranging from DNS to RANS [Colour figure can be viewed at wileyonlinelibrary.com]

Table 6 offers a summary of the stability limits with respect to the maximum possible value of $\lambda^{\text{Re}}_{\text{max},N_H}$ for the respective Reynolds number and resolution N_H at Ma = 1/30. For Re = 700 all resolutions feature inherent stability over the entire range of investigated $\lambda \in [10^{-6}, 10^{6}]$. Maximum possible values reduce when the Reynolds number increases and the resolution decreases. It is noted that maximum values are not necessarily optimal, compare Section 5.

The turbulent energy spectra of the v-component are illustrated in Figure 43. Each graph displays the results of the four different Reynolds numbers for a fixed grid. Here, the entire frequency range plots correspond to $\lambda_{\text{def}} = 10^{-2}$. In contrast, companion cutouts describe the changes in the dissipation range when increasing the limiter value to the case-specific optimum. For Re = 700, the spectra are deemed grid (N_H), and limiter (λ) converged since a variation of λ does not significantly alter the spectra. In all cases, applying λ_{opt} eliminates the kink associated with the onset of the regularization, which is distinctly seen for Re ≥ 2800 using λ_{def}. An indication of the resolution requirements for Re = 37,000 is outlined by the almost congruent spectra for Re = 10,600 (orange) and Re = 37,000 (red) for all grids. Just for the fine grid (C), small extensions of the inertial subrange are observed when increasing Re.

TABLE 7 Optimal limiter choice λ_{opt} and classification of the grid types based on the particular y^+ maxima for the investigated parameter space (Re, N_H)

Re	N_H	Re_c	λ_{max}	λ_{opt}	$y^+_{T,av}(\lambda_{def})$	$y^+_{T,av}(\lambda_{opt})$	Grid type
700	56	12.5	10^6	No influence	0.5	≡	DNS
	28	25	10^6	No influence	1.0	≡	LES
	14	50	10^6	10^{-1}	2.0	≡	LES
2800	56	50	10^6	10^{-1}	1.6	≡	LES
	28	100	10^6	10^{-1}	3.2	≡	LES
	14	200	10^3	10^{-1}	6.3	≡	LES
10,600	56	190	10^1	10^{-1}	4.8	5.0	LES
	28	380	10^0	10^0	8.9	9.7	VLES
	14	760	10^0	5×10^{-1}	14.5 [16.7]	15.9 [18.3]	VLES/RANS limit
37,000	56	660	5×10^{-1}	5×10^{-1}	11.1	12.4	VLES
	28	1320	5×10^{-1}	✗	19.0 [26.6]	✗	RANS (†)
	14	2640	10^{-1}	✗	30.5 [61.0]	✗	RANS (†)

5 | SUMMARY AND CONCLUSION

Based on the periodic hill test case results, the WP cumulant LBM is considered a robust and efficient opportunity to simulate separated turbulent flows without using a classical turbulence model. In line with a former study on simple channel flows,[19] the WP cumulant outperforms previous nonparameterized and AllOne cumulant collision operators, and the use of the regularization ensures a sufficient level of numerical stability. This applies for wall-resolved DNS and LES grids up to resolution of $\Delta x_i^+ \approx 30$ ($y^+ \approx 15$). Moreover, the results of the acoustic scaling studies did reflect a negligible sensitivity to the Mach number in the range of $1/10 \leq \mathrm{Ma} \leq 1/90$ for all tested resolutions and Reynolds numbers.

The seamless blend from DNS to (V)LES is a distinct advantage of the regularized WP cumulant collision operator, and the resolution requirements are relatively moderate, as already pointed out by Geier et al.[43] On the downside, the above-mentioned resolution requirements still pose severe feasibility restrictions in an engineering context. However, recent distributed-memory CPU computations[62] for up to 2.0×10^{11} grid nodes or state-of-the-art GPU-based AI systems, for example, NVIDIA DGX A100, with up to 640GB shared-memory and $\mathcal{O}(10^5)$ CUDA cores enabling computations with up to $\mathcal{O}(10^9)$ grid nodes in a single server setup, demonstrate a considerable reduction of hardware related limitations. Furthermore, recent LBM related studies[63,64] executed on a distributed-memory HPC cluster also involve up to 3.3×10^9 nodes processed by maximal 256 GPUs in parallel.

The stability preserving regularization might be interpreted as a dynamic turbulence model mostly confined to the upper dissipative frequencies by addressing the higher relaxation rates. The related regularization parameter λ is usually assigned to a constant value with $\lambda_{def} = 10^{-2}$ and modifications were barely discussed in detail. This default value seems conservative. A lower λ-value rapidly drives the simulation toward the AllOne approach and hampers the resolution of the flow dynamics. In contrast, results might benefit from increasing the λ-value as the resolution transits from $\Delta x_i^+ \approx 10$ to coarser resolutions $\Delta x_i^+ \approx 30$ (VLES resolutions) to avoid the damping of intensive turbulence generation in the buffer layer. The risks to impede the stability and robustness of the simulation are moderate for lower Reynolds numbers but increase for higher Reynolds numbers where the stability limits approach $\lambda_{max} = 10^{-1}$ in the present studies. Given the attainable predictive accuracy, this value seems more appropriate than the default value $\lambda_{def} = 10^{-2}$. In severely under-resolved cases, for example, $\Delta x_i^+ \geq 30$, the additional use of a traditional SGS model may help in parts but was no panacea for the investigated flow.

Supplementary to the resolution of near-wall flows, an upper threshold of the regularization parameter λ might be judged by the cell Reynolds number. For the investigated flows, $\mathrm{Re_c} = u_B\, \Delta x/\nu = \mathrm{Re}/N_H \lesssim 750$ seems a viable criterion to run simulations with an increased $\lambda = 10^{-1}$, compare Table 7. As outlined in this table, maximal values of λ increase from the finest ($\mathrm{Re} = 700$, $N_H = 56$) to the coarsest ($\mathrm{Re} = 37{,}000$, $N_H = 14$) resolution. Unlike λ_{max}, optimal λ-values identified

in the present study focus on a narrow range $\lambda_{\text{opt}} \in [10^{-1}; 10^{0}]$ and the lower value seems a good candidate. The sixth and seventh column of Table 7 display the nondimensional wall distances $y^{+}_{\text{T,av}}(\lambda_{\delta})$ along the top wall. Respective deviations due to the different choice of λ remain rather small. However, as the resolution deteriorates, the imposed wall boundary condition and the related assumption on the wall shear become a major source of error beyond $y^{+} \geq 15$, as indicated by the square bracketed values obtained from an alternative profile, for example $u^{+}(y^{+}) = 8.4\,(y^{+})^{1/7}$. In such cases, the investigated grids (†) featuring 40 [50] $\leq \Delta x_i^{+} \leq$ 60 [120] are classified as too coarse since any limiter choice does not remedy prevailing upper wall defects.

Figure 44 offers a supplementary visualization of the tabulated data. Analyzing the modifications of the relaxation rates $\omega_{3,4,5}$ due to the influence of the regularization parameter λ, it appears that an alternative regularization approach that automatically restrains a low level of dynamics might refer to relative changes of the parameterized relaxation rates $\omega_{3,4,5}$ and is the subject of future research. Moreover, the WP properties for simulating the PHTC at higher Reynolds numbers in conjunction with a wall function[17,65] are of interest.

ACKNOWLEDGEMENT

Open Access funding enabled and organized by Projekt DEAL.

ORCID

Martin Gehrke https://orcid.org/0000-0002-5073-397X
Thomas Rung https://orcid.org/0000-0002-3454-1804

REFERENCES

1. Niedermeier CA, Janßen CF, Indinger T. Massively-parallel multi-GPU simulations for fast and accurate automotive aerodynamics. Proceedings of the 7th European Conference on Computational Fluid Dynamics; June 11–15, 2018; Glasgow.
2. Pasquali A, Schönherr M, Geier M, Krafczyk M. Simulation of external aerodynamics of the DrivAer model with the LBM on GPGPUs. In: Joubert GR, Leather H, Parsons M, Peters F, Sawyer M, eds. *Parallel Computing: On the Road to Exascale*. Vol 27. IOS Press; 2016:391-400.
3. Lenz S, Schönherr M, Geier M, et al. Towards real-time simulation of turbulent air flow over a resolved urban canopy using the cumulant lattice Boltzmann method on a GPGPU. *J Wind Eng Ind*. 2019;189:151-162.
4. Bhatnagar PL, Gross EP, Krook M. A model for collision processes in gases. I. Small amplitude processes in charged and neutral one-component systems. *Phys Rev*. 1954;94:511-525.
5. Coreixas C, Wissocq G, Chopard B, Latt J. Impact of collision models on the physical properties and the stability of lattice Boltzmann methods. *Philos Trans A Math Phys Eng Sci*. 2020;378:20190397.
6. Ginzburg I, Verhaeghe F, d'Humières D. Two-relaxation-time lattice Boltzmann scheme: about parametrization, velocity, pressure and mixed boundary conditions. *Commun Comput Phys*. 2008;3(2):427-478.
7. Ginzburg I, Verhaeghe F, d'Humières D. Study of simple hydrodynamic solutions with the two-relaxation-times lattice Boltzmann scheme. *Commun Comput Phys*. 2008;3(3):519-581.
8. d'Humières D, Ginzburg I, Krafczyk M, Lallemand P, Luo LS. Multiple-relaxation-time lattice Boltzmann models in three dimensions. *Philos Trans R Soc A*. 2002;360:437-451.
9. Tölke J, Freudiger S, Krafczyk M. An adaptive scheme using hierarchical grids for lattice Boltzmann multi-phase flow simulations. *Comput Fluids*. 2006;35(8):820-830.
10. Geier M, Greiner A, Korvink JG. Cascaded digital lattice Boltzmann automata for high Reynolds number flow. *Phys Rev E*. 2006;73(6):066705.
11. Latt J, Chopard B. Lattice Boltzmann method with regularized pre-collision distribution functions. *Math Comput Simul*. 2006;72(2):165-168.
12. Karlin IV, Bösch F, Chikatamarla SS. Gibbs' principle for the lattice-kinetic theory of fluid dynamics. *Phys Rev E*. 2014;90(3):031302.
13. Bösch F, Chikatamarla SS, Karlin IV. Entropic multirelaxation lattice Boltzmann models for turbulent flows. *Phys Rev E*. 2015;92(4):043309.
14. Dorschner D, Bösch F, Chikatamarla SS, Karlin IV. Entropic multi-relaxation time lattice Boltzmann model for complex flows. *J Fluid Mech*. 2016;801:623-651.
15. Geier M, Schönherr M, Pasquali A, Krafczyk M. The cumulant lattice Boltzmann equation in three dimensions: theory and validation. *Comput Math Appl*. 2015;70(4):507-547.
16. Geier M, Pasquali A, Schönherr M. Parametrization of the cumulant lattice Boltzmann method for fourth order accurate diffusion part I: derivation and validation. *J Comput Phys*. 2017;348:862-888.
17. Pasquali A, Geier M, Krafczyk M. Near-wall treatment for the simulation of turbulent flow by the cumulant lattice Boltzmann method. *Comput Math Appl*. 2020;79:195-212.
18. Gehrke M, Janßen CF, Rung T. Scrutinizing lattice Boltzmann methods for direct numerical simulations of turbulent channel flows. *Comput Fluids*. 2017;156:247-263.

19. Gehrke M, Banari A, Rung T. Performance of under-resolved, model-free LBM simulations in turbulent shear flows. In: Hoarau Y, Peng SH, Schwamborn D, Revell A, Mockett C, eds. *Progress in Hybrid RANS-LES Modelling*. Springer International Publishing; 2020:3-18.
20. Nathen P, Gaudlitz D, Krause MJ, Adams NA. On the stability and accuracy of the BGK, MRT and RLB Boltzmann schemes for the simulation of turbulent flows. *Commun Comput Phys*. 2018;23:846-876.
21. Geier M, Lenz S, Schönherr M, Krafczyk M. Under-resolved and large eddy simulations of a decaying Taylor-Green vortex with the cumulant lattice Boltzmann method. *Theor Comput Fluid Dyn*. 2020.
22. Mellen CP, Fröhlich J, Rodi W. Large eddy simulation of the flow over periodic hills. Proceedings of the 16th IMACS World Congress; August 21–25, 2000; International Association for Mathematics and Computers in Simulation, Lausannes.
23. Silva G, Semiao V. Truncation errors and the rotational invariance of three-dimensional lattice models in the lattice Boltzmann method. *J Comput Phys*. 2014;269:259-279.
24. Rapp C, Breuer M, Manhart M, Peller N. 2D periodic hill flow (UFR 3-30 Test Case), ERCOFTAC; 2009. Accessed January 10, 2021 https://www.kbwiki.ercoftac.org/w/index.php?title=UFR_3-30_Test_Case
25. Breuer M, Rodi W. Large eddy simulation for complex turbulent flows of practical interest. In: Hirschel EH, ed. *Flow Simulation with High-Performance Computers II: DFG Priority Research Programme Results 1993–1995*. Vieweg+Teubner Verlag; 1996:258-274.
26. Manhart M, Tremblay F, Friedrich R. MGLET: a parallel code for efficient DNS and LES of complex geometries. In: Jenssen CB, Andersson HI, Ecer A, et al., eds. *Parallel Computational Fluid Dynamics 2000*. North-Holland; 2001:449-456.
27. Rapp C, Manhart M. Flow over periodic hills: an experimental study. *Exp Fluids*. 2011;51(1):247-269.
28. Almeida GP, Durão DFG, Heitor MV. Wake flows behind two-dimensional model hills. *Exp Therm Fluid Sci*. 1993;7(1):87-101.
29. Bonnin JC, Buchal T, Rodi W. Revised test case descriptions and calculation results. Proceedings of the ERCOFTAC Workshop on Data Bases and Testing of Calculation Methods for Turbulent Flows in Association with 4th ERCOFTAC/IAHR Workshop on Refined Flow Modeling; April 3–7, 1995; Karlsruhe.
30. Rapp C, Manhart M. Experimental investigations on the turbulent flow over a periodic hill geometry. Proceedings of the 5th International Symposium on Turbulence and Shear Flow Phenomena; 2007:649-654; München, Begell House Inc.
31. Fröhlich J, Mellen CP, Rodi W, Temmerman L, Leschziner MA. Highly resolved large-eddy simulation of separated flow in a channel with streamwise periodic constrictions. *J Fluid Mech*. 2005;526:19-66.
32. Kähler CJ, Scharnowski S, Cierpka C. Highly resolved experimental results of the separated flow in a channel with streamwise periodic constrictions. *J Fluid Mech.* 2016;769:257-284.
33. Breuer M, Jaffrézic B, Peller N, et al. A comparative study of the turbulent flow over a periodic arrangement of smoothly contoured hills. In: Lamballais E, Friedrich R, Geurts BJ, Métais O, eds. *Direct and Large-Eddy Simulation VI*. Springer Netherlands; 2006:635-642.
34. Breuer M, Peller N, Rapp C, Manhart M. Flow over periodic hills–Numerical and experimental study in a wide range of Reynolds numbers. *Comput Fluids*. 2009;38(2):433-457.
35. Xia Z, Shi Y, Hong R, Xiao Z, Chen S. Constrained large-eddy simulation of separated flow in a channel with streamwise-periodic constrictions. *J Turbul*. 2013;14(1):1-21.
36. Gloerfelt X, Cinnella P. Large eddy simulation requirements for the flow over periodic hills. *Flow Turbul Combust*. 2019;103:55-91.
37. Gao W, Cheng W, Samtaney R. Large-eddy simulations of turbulent flow in a channel with streamwise periodic constrictions. *J Fluid Mech*. 2020;900:A43.
38. Xiao H, Wu JL, Laizet S, Duan L. Flows over periodic hills of parameterized geometries: a dataset for data-driven turbulence modeling from direct simulations. *Comput Fluids*. 2020;200:104431.
39. Seeger S, Hoffmann KH. The cumulant method for computational kinetic theory. *Contin Mech Thermodyn*. 2000;12:403-421.
40. Far EK, Geier M, Kutscher K, Krafczyk M. Simulation of micro aggregate breakage in turbulent flows by the cumulant lattice Boltzmann method. *Comput Fluids*. 2016;140:222-231.
41. Asmuth H, Olivares-Espinosa H, Nilsson K, Ivanell S. The actuator line model in lattice Boltzmann frameworks: numerical sensitivity and computational performance. *J Phys Conf Ser*. 2019;1256:012022
42. Banari A, Gehrke M, Janßen CF, Rung T. Numerical simulation of nonlinear interactions in a naturally transitional flat plate boundary layer. *Comput Fluids*. 2020;203:104502.
43. Geier M, Pasquali A, Schönherr M. Parametrization of the cumulant lattice Boltzmann method for fourth order accurate diffusion part II: application to flow around a sphere at drag crisis. *J Comput Phys*. 2017;348:889-898.
44. Asmuth H, Olivares-Espinosa H, Ivanell S. Actuator line simulations of wind turbine wakes using the lattice Boltzmann method. *Wind Energy Sci*. 2020;5(2):623-645.
45. Janßen CF, Mierke D, Überrück M, Gralher S, Rung T. Validation of the GPU-accelerated CFD solver ELBE for free surface flow problems in civil and environmental engineering. *Computation*. 2015;3(3):354-385.
46. Qian Y, d'Humières D, Lallemand P. Lattice BGK models for Navier Stokes equation. *Europhys Lett*. 1992;17(6):479-784.
47. Yu D, Mei R, Luo LS, Shyy W. Viscous flow computations with the method of lattice Boltzmann equation. *Prog Aerosp Sci*. 2003;39:329-367.
48. Chapman S, Cowling TG. *The Mathematical Theory of Non-Uniform Gases. An Account of the Kinetic Theory of Viscosity, Thermal Conduction and Diffusion in Gases*. Cambridge University Press; 1970.
49. Tölke J. Implementation of a lattice Boltzmann kernel using the compute unified device architecture developed by nVIDIA. *Comput Vis Sci*. 2008;13:29-39.
50. Pasquali A. *Enabling the Cumulant Lattice Boltzmann Method for Complex CFD Engineering Problems*. PhD. thesis. Technische Universität Carolo-Wilhelmina zu Braunschweig; 2016.

51. Mierke D, Janßen CF, Rung T. An efficient algorithm for the calculation of sub-grid distances for higher-order LBM boundary conditions in a GPU simulation environment. *Comput Math Appl*. 2020;79(1):66-87.
52. Yu D, Mei R, Shyy W. A Unified boundary treatment in lattice Boltzmann method. Proceedings of the 41st Aerospace Sciences Meeting and Exhibit AIAA 3003-0953; January 6–9, 2003; Reno, NV.
53. Bouzidi M, Firdaouss M, Lallemand P. Momentum transfer of a Boltzmann-lattice fluid with boundaries. *Phys Fluids*. 2001;13(11):3452-3459.
54. Dubief Y, Delcayre F. On coherent-vortex identification in turbulence. *J Turbul*. 2000;11:N11.
55. Lumley JL, Newman GR. The return to isotropy of homogeneous turbulence. *J Fluid Mech*. 1977;82(1):161-178.
56. Choi KS, Lumley JL. The return to isotropy of homogeneous turbulence. *J Fluid Mech*. 2001;436:59-84.
57. Banerjee S, Krahl R, Durst F, Zenger C. Presentation of anisotropy properties of turbulence, invariants versus eigenvalue approaches. *J Turbul*. 2007;8:N32.
58. Werner H, Wengle H. Large-eddy simulation of turbulent flow over and around a cube in a plate channel. In: Durst F, Friedrich R, Launder BE, Schmidt FW, Schumann U, Whitelaw JH, eds. *Turbulent Shear Flows*. Vol 8. Springer; 1993:155-168.
59. Girimaji SS. Boltzmann kinetic equation for filtered fluid turbulence. *Phys Rev Lett*. 2007;99(3):034501.
60. Smagorinsky J. General circulation experiments with the primitive equations. *Mon Weather Rev*. 1963;91(3):99-164.
61. Chang PH, Liao CC, Hsu HW, Liu SH, Lin CA. Simulations of laminar and turbulent flows over periodic hills with immersed boundary method. *Comput Fluids*. 2014;92:233-243.
62. Schornbaum F, Rüde U. Massively parallel algorithms for the Lattice Boltzmann method on nonuniform grids. *SIAM J Sci Comput*. 2016;38:96-126.
63. Hasegawa Y, Aoki T, Kobayashi H, Shirasaki K. Large-scale LES analysis for aerodynamics of a group of racing bicycles by lattice Boltzmann method. *Trans Jpn Soc Mech Eng*. 2019;85(870):18-00441.
64. Watanabe S, Aoki T. Large-scale flow simulations using lattice Boltzmann method with AMR following free-surface on multiple GPUs. *Comput Phys Commun*. 2021;264:107871.
65. Wilhelm S, Jacob J, Sagaut P. An explicit power-law-based wall model for lattice Boltzmann method-Reynolds-averaged numerical simulations of the flow around airfoils. *Phys Fluids*. 2018;30(6):065111.

How to cite this article: Gehrke M, Rung T. Periodic hill flow simulations with a parameterized cumulant lattice Boltzmann method. *Int J Numer Meth Fluids*. 2022;94(8):1111-1154. doi: 10.1002/fld.5085

APPENDIX A. GEOMETRY DEFINITION

The underlying test case geometry initially published by Almeida et al.[28] is defined piecewise via six polynomials $s_i(x)$ given in a nondimensional representation rounded to three decimal places as

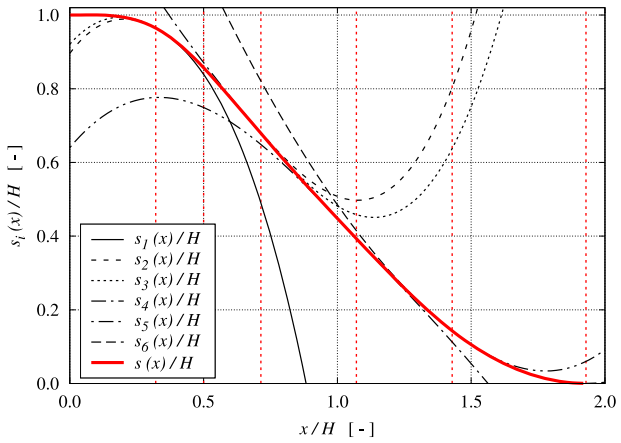

FIGURE A1 Hill geometry piecewisely defined via six polynomials $s_i(x)$ normalized by the hill height H [Colour figure can be viewed at wileyonlinelibrary.com]

$$s_i(x)/H = \begin{cases} \min\left(1, 1.000 + 0.190\,x^2 - 1.666\,x^3\right) & x \in [0, 0.321]\ H \\ 0.896 + 0.975\,x - 2.845\,x^2 + 1.482\,x^3 & x \in]0.321, 0.500]\ H \\ 0.921 + 0.821\,x - 2.536\,x^2 + 1.275\,x^3 & x \in]0.500, 0.714]\ H \\ 1.445 - 1.380\,x + 0.545\,x^2 - 0.162\,x^3 & x \in]0.714, 1.071]\ H \\ 0.640 + 0.874\,x - 1.559\,x^2 + 0.492\,x^3 & x \in]1.071, 1.429]\ H \\ \max\left(0,\ 2.014 - 2.011\,x + 0.461\,x^2 + 0.021\,x^3\right) & x \in]1.429, 1.929]\ H \end{cases} \tag{A1}$$

where the hill height H is equal to unity within this notation. The resulting contour of the hill is shown in Figure A1 (red graph).

APPENDIX B. CUMULANT COLLISION OPERATOR - IMPLEMENTATION

The following part of the appendix includes the implementation of the Cumulant collision operator within the `elbe`[45] LBM framework. The documentation is mainly close to the publications of Geier et al.[15,16] Firstly, details regarding the well-conditioning context of the approach are considered in Section B.1, followed by the one-to-one collision step implementation for the underlying fixed set of relaxation rates in Section B.2.

B.1 Conditioning

The conditioning modifications refer to two major improvements suggested by Geier et al.[15] The first modification addresses reducing rounding errors. These can significantly impact the quality of results for single and double precision simulations in low-velocity regimes. Therefore, to reduce rounding errors, which originate from the compressible nature of the cumulant approach, the so-called *well-conditioned* (W) PDFs are obtained by subtracting the weights w_{ijk} from the compressible (c) defined PDFs

$$f_{ijk} = f^{\mathrm{c}}_{ijk} - w_{ijk}. \tag{B1}$$

The respective weights of the $D3Q27$ velocity space are given by

$$w_{ijk} = \begin{cases} \frac{8}{27} & ijk = \{000\} \\ \frac{2}{27} & ijk = \{100, 010, 001, \bar{1}00, 0\bar{1}0, 00\bar{1}\} \\ \frac{1}{54} & ijk = \{110, 1\bar{1}0, \bar{1}10\ \bar{1}\bar{1}0, 101, 10\bar{1}, \bar{1}01, \bar{1}0\bar{1}, 011, 01\bar{1}, 0\bar{1}1, 0\bar{1}\bar{1}\} \\ \frac{1}{216} & ijk = \{111, 11\bar{1}, 1\bar{1}1, \bar{1}11, 1\bar{1}\bar{1}, \bar{1}1\bar{1}, \bar{1}\bar{1}1, \bar{1}\bar{1}\bar{1}\} \end{cases}. \tag{B2}$$

Based on the discrete velocity space, compare Figure 3 and matrix (4), the center is weighted by 8/27 (orange), the main axes by 2/27 (green), the medians (blue) of the cube by 1/54 and its vertices (red) by 1/216.

The second modification comprises an explicit prescription for computing macroscopic quantities. This essentially involves a favorable pairwise summation and subtraction of inverse *PDF* directions as well as a separation of the different cube contributions (vertices, medians, main axes, and center). To this end, the density fluctuation is given by

$$\begin{aligned} \delta\rho = \Bigg[& \underbrace{(((f_{111} + f_{\bar{1}\bar{1}\bar{1}}) + (f_{1\bar{1}\bar{1}} + f_{\bar{1}1\bar{1}})) + ((f_{11\bar{1}} + f_{\bar{1}\bar{1}1}) + (f_{1\bar{1}1} + f_{\bar{1}1\bar{1}})))}_{\text{Vertices}} \\ & + \underbrace{(((f_{011} + f_{0\bar{1}\bar{1}}) + (f_{01\bar{1}} + f_{0\bar{1}1})) + ((f_{101} + f_{\bar{1}0\bar{1}}) + (f_{10\bar{1}} + f_{\bar{1}01})) + ((f_{110} + f_{\bar{1}\bar{1}0}) + (f_{1\bar{1}0} + f_{\bar{1}10})))}_{\text{Medians}} \\ & + \underbrace{((f_{100} + f_{\bar{1}00}) + (f_{010} + f_{0\bar{1}0}) + (f_{001} + f_{00\bar{1}}))}_{\text{Main Axes}} \Bigg] + \underbrace{f_{000}}_{\text{Center}}, \end{aligned} \tag{B3}$$

and the velocity components follow from

$$u = [(((f_{111} - f_{\bar{1}\bar{1}\bar{1}}) + (f_{1\bar{1}1} - f_{\bar{1}1\bar{1}})) + ((f_{11\bar{1}} - f_{\bar{1}\bar{1}1}) + (f_{1\bar{1}\bar{1}} - f_{\bar{1}11})))$$
$$+ (((f_{101} - f_{\bar{1}0\bar{1}}) + (f_{10\bar{1}} - f_{\bar{1}01})) + ((f_{110} - f_{\bar{1}\bar{1}0}) + (f_{1\bar{1}0} - f_{\bar{1}10}))) + (f_{100} - f_{\bar{1}00})]/\rho, \tag{B4}$$

$$v = [(((f_{111} - f_{\bar{1}\bar{1}\bar{1}}) + (f_{\bar{1}11} - f_{1\bar{1}\bar{1}})) + ((f_{11\bar{1}} - f_{\bar{1}\bar{1}1}) + (f_{\bar{1}1\bar{1}} - f_{1\bar{1}1})))$$
$$+ (((f_{011} - f_{0\bar{1}\bar{1}}) + (f_{01\bar{1}} - f_{0\bar{1}1})) + ((f_{110} - f_{\bar{1}\bar{1}0}) + (f_{\bar{1}10} - f_{1\bar{1}0}))) + (f_{010} - f_{0\bar{1}0})]/\rho, \tag{B5}$$

$$w = [(((f_{111} - f_{\bar{1}\bar{1}\bar{1}}) + (f_{\bar{1}11} - f_{1\bar{1}\bar{1}})) + ((f_{1\bar{1}1} - f_{\bar{1}1\bar{1}}) + (f_{\bar{1}\bar{1}1} - f_{11\bar{1}})))$$
$$+ (((f_{011} - f_{0\bar{1}\bar{1}}) + (f_{0\bar{1}1} - f_{01\bar{1}})) + ((f_{101} - f_{\bar{1}0\bar{1}}) + (f_{\bar{1}01} - f_{10\bar{1}}))) + (f_{001} - f_{00\bar{1}})]/\rho. \tag{B6}$$

Optional body forces F_i are incorporated by shifting the frame of reference via $u_i = u_i + \Delta t\ F_i/(2\rho)$. This shift operation is implemented prior to the subsequent transformations from PDF → central moments → cumulants, in which the velocity components appear. Moreover, the shift affects the backward transformation from cumulants into the space of (relaxed) central moments wherein the first order central moments change sign.

B.2 Collision in cumulant space

Equations (B7) to (B32) depict the entire explicit implementation of the collision step for the underlying relaxation rate set with $\omega_2 = 1$, $\{\omega_6, ..., \omega_{10}\} = 1$ and $\omega_{1|3|4|5}$ defined by Equations (13) and (14) through (16) respectively in the limiter version via (20) to (26), compare Section 2.2.

The presentation aims at showing the shortest version of the collision step by omitting the use of linear combinations within the expressions as compared to the fundamental work of Geier et al.[16] and by neglecting intrinsic zero contributions attributed to the chosen relaxation rates. For the required transformations (PDF space → central moments → cumulants and respective back transformations) the reader is referred to the original paper,[16] compare Section 3 therein.

The zeroth and first-order cumulants are directly linked to the macroscopic flow quantities that are conserved properties during collision implying their relaxation is left out, whereby $C^*_{000} = C_{000}$ and so forth holds. The only equilibria that are nonzero are three second order ($C^{eq}_{200}, C^{eq}_{020}, C^{eq}_{002}$) and all fourth order cumulants. The modified equilibria are traced to repairing the anisotropy arising from the underlying discretization. Both the parameters A and B, compare Equations (17) and (18), and three derivatives,

$$D_x\ u = \omega_1/(2\ \rho)\ (-2\ C_{200} + C_{020} + C_{002}) - 1/(2\ \rho)\ (C_{200} + C_{020} + C_{002} - k_{000}), \tag{B7}$$

$$D_y\ v = \omega_1/(2\ \rho)\ (C_{200} + 2\ C_{020} + C_{002}) - 1/(2\ \rho)\ (C_{200} + C_{020} + C_{002} - k_{000}), \tag{B8}$$

$$D_z\ w = \omega_1/(2\ \rho)\ (C_{200} + C_{020} + 2\ C_{002}) - 1/(2\ \rho)\ (C_{200} + C_{020} + C_{002} - k_{000}), \tag{B9}$$

occur in these expressions. k_{000} represents the zeroth order central moment. Hence, the collisional part explicitly reads:

$$C^*_{110} = (1 - \omega_1)\ C_{110}, \tag{B10}$$

$$C^*_{101} = (1 - \omega_1)\ C_{101}, \tag{B11}$$

$$C^*_{011} = (1 - \omega_1)\ C_{011}, \tag{B12}$$

$$C^*_{200} = [(1 - \omega_1)\ (C_{200} - C_{020}) - 3\ \rho\ (1 - \omega_1/2)\ (u^2\ D_x\ u - v^2\ D_y\ v)$$
$$+ (1 - \omega_1)\ (C_{200} - C_{002}) - 3\ \rho\ (1 - \omega_1/2)\ (u^2\ D_x\ u - w^2\ D_z\ w)$$
$$+ k_{000} - 3\ \rho\ (1 - 1/2)\ (u^2\ D_x\ u + v^2\ D_y\ v + w^2\ D_z\ w)]/3, \tag{B13}$$

$$C^*_{020} = [-2\ (1 - \omega_1)\ (C_{200} - C_{020}) + 6\ \rho\ (1 - \omega_1/2)\ (u^2\ D_x\ u - v^2\ D_y\ v)$$
$$+ (1 - \omega_1)\ (C_{200} - C_{002}) - 3\ \rho\ (1 - \omega_1/2)\ (u^2\ D_x\ u - w^2\ D_z\ w)$$
$$+ k_{000} - 3\ \rho\ (1 - 1/2)\ (u^2\ D_x\ u + v^2\ D_y\ v + w^2\ D_z\ w)]/3, \tag{B14}$$

$$C^*_{002} = [(1-\omega_1)\,(C_{200}-C_{020}) - 3\,\rho\,(1-\omega_1/2)\,(u^2\,D_x\,u - v^2\,D_y\,v) - 2\,(1-\omega_1)\,(C_{200}-C_{002}) + 6\,\rho\,(1-\omega_1/2)\,(u^2\,D_x\,u - w^2\,D_z\,w) + k_{000} - 3\,\rho\,(1-1/2)\,(u^2\,D_x\,u + v^2\,D_y\,v + w^2\,D_z\,w)]/3, \tag{B15}$$

$$C^*_{102} = [(1-\omega^{\lambda}_{3,1})\,(C_{120}+C_{102}) - (1-\omega^{\lambda}_{4,2})\,(C_{120}-C_{102})]/2, \tag{B16}$$

$$C^*_{120} = [(1-\omega^{\lambda}_{3,1})\,(C_{120}+C_{102}) + (1-\omega^{\lambda}_{4,1})\,(C_{120}-C_{102})]/2, \tag{B17}$$

$$C^*_{012} = [(1-\omega^{\lambda}_{3,2})\,(C_{210}+C_{012}) - (1-\omega^{\lambda}_{4,2})\,(C_{210}-C_{012})]/2, \tag{B18}$$

$$C^*_{210} = [(1-\omega^{\lambda}_{3,2})\,(C_{210}+C_{012}) + (1-\omega^{\lambda}_{4,2})\,(C_{210}-C_{012})]/2, \tag{B19}$$

$$C^*_{021} = [(1-\omega^{\lambda}_{3,3})\,(C_{201}+C_{021}) - (1-\omega^{\lambda}_{4,3})\,(C_{201}-C_{021})]/2, \tag{B20}$$

$$C^*_{201} = [(1-\omega^{\lambda}_{3,3})\,(C_{201}+C_{021}) + (1-\omega^{\lambda}_{4,3})\,(C_{201}-C_{021})]/2, \tag{B21}$$

$$C^*_{111} = (1-\omega^{\lambda}_{5})\,C_{111}, \tag{B22}$$

$$C^*_{220} = [2/3\,(1/\omega_1 - 1/2)\,A\,\rho\,(D_x\,u - 2\,D_y\,v + D_z\,w) + 2/3\,(1/\omega_1 - 1/2)\,A\,\rho\,(D_x\,u + D_y\,v - 2\,D_z\,w) - 4/3\,(1/\omega_1 - 1/2)\,A\,\rho\,(D_x\,u + D_y\,v + D_z\,w)]/3, \tag{B23}$$

$$C^*_{022} = [-2/3\,(1/\omega_1 - 1/2)\,A\,\rho\,(D_x\,u + D_y\,v - 2\,D_z\,w) - 4/3\,(1/\omega_1 - 1/2)\,A\,\rho\,(D_x\,u + D_y\,v + D_z\,w)]/3, \tag{B24}$$

$$C^*_{202} = [-2/3\,(1/\omega_1 - 1/2)\,A\,\rho\,(D_x\,u - 2\,D_y\,v + D_z\,w) - 4/3\,(1/\omega_1 - 1/2)\,A\,\rho\,(D_x\,u + D_y\,v + D_z\,w)]/3, \tag{B25}$$

$$C^*_{211} = (1-\omega_1/2)\,B\,C_{011}, \tag{B26}$$

$$C^*_{121} = (1-\omega_1/2)\,B\,C_{101}, \tag{B27}$$

$$C^*_{112} = (1-\omega_1/2)\,B\,C_{110}, \tag{B28}$$

$$C^*_{221} = 0, \tag{B29}$$

$$C^*_{212} = 0, \tag{B30}$$

$$C^*_{122} = 0, \tag{B31}$$

$$C^*_{222} = 0. \tag{B32}$$